

DTIC FILE COPY

AD-A220 776

4

TECHNICAL REPORT BRL-TR-3090

# BRL

## MECHANISMS INDUCING JET ROTATION IN SHEAR-FORMED SHAPED-CHARGE LINERS

STEVEN B. SEGLETES

DTIC  
ELECTE  
APR 24 1990  
S D  
Co D

MARCH 1990

APPROVED FOR PUBLIC RELEASE; DISTRIBUTION UNLIMITED.

U.S. ARMY LABORATORY COMMAND

BALLISTIC RESEARCH LABORATORY  
ABERDEEN PROVING GROUND, MARYLAND

## **DESTRUCTION NOTICE**

**Destroy this report when it is no longer needed. DO NOT return it to the originator.**

**Additional copies of this report may be obtained from the National Technical Information Service, U.S. Department of Commerce, 5285 Port Royal Road, Springfield, VA 22161.**

**The findings of this report are not to be construed as an official Department of the Army position, unless so designated by other authorized documents.**

**The use of trade names or manufacturers' names in this report does not constitute indorsement of any commercial product.**

# UNCLASSIFIED

REPORT DOCUMENTATION PAGE			Form Approved OMB No. 0704-0188		
Public reporting burden for this collection of information is estimated to average 1 hour per response, including the time for reviewing instructions, searching existing data sources, gathering and maintaining the data needed, and completing and reviewing the collection of information. Send comments regarding this burden estimate or any other aspect of this collection of information, including suggestions for reducing this burden, to Washington Headquarters Services, Directorate for Information Operations and Reports, 1215 Jefferson Davis Highway, Suite 1204, Arlington, VA 22202-4302, and to the Office of Management and Budget, Paperwork Reduction Project (0704-0188), Washington, DC 20503.					
1. AGENCY USE ONLY (Leave blank)		2. REPORT DATE March 1990	3. REPORT TYPE AND DATES COVERED Final, Sep 84 - Dec 88		
4. TITLE AND SUBTITLE Mechanisms Inducing Jet Rotation in Shear-Formed Shaped-Charge Liners			5. FUNDING NUMBERS		
6. AUTHOR(S) Steven B. Segletes					
7. PERFORMING ORGANIZATION NAME(S) AND ADDRESS(ES)			8. PERFORMING ORGANIZATION REPORT NUMBER		
9. SPONSORING / MONITORING AGENCY NAME(S) AND ADDRESS(ES) US Army Ballistic Research Laboratory ATTN: SLCBR-DD-T Aberdeen Proving Ground, MD 21005-5066			10. SPONSORING / MONITORING AGENCY REPORT NUMBER  BRL-TR-3090		
11. SUPPLEMENTARY NOTES Doctoral Thesis at Drexel University, Oct 88					
12a. DISTRIBUTION / AVAILABILITY STATEMENT Approved for public release; distribution unlimited.			12b. DISTRIBUTION CODE		
13. ABSTRACT (Maximum 200 words) This report is concerned with the mechanisms by which rotation may be introduced into the jet of a stationary shaped charge which employs a shear-formed liner. After a brief review of the past efforts in the area, an analysis is presented on the nature of jet rotation as it relates to the concept of shaped-charge jet spin compensation.  Two mechanisms are introduced which have traditionally been considered likely candidates for inducing rotation in jets from shear-formed liners. These mechanisms are residual stress and mechanical anisotropy. Analytical, experimental and computational analyses are presented in an attempt to quantify the jet rotation rate that each respective mechanism is likely to effect, thus revealing the relative importance which should be attached to each mechanism. Results indicate that mechanical anisotropy in the shear-formed liner is the significant mechanism involved in producing a rotational jet from a stationary shaped charge. <i>Keywords:</i>					
14. SUBJECT TERMS Shaped charge Spin compensation Anisotropy <i>Jet rotation Hydrocode, Shaped Charge Liners, Shear form Shaped Charge Projectiles (HLL)</i>			15. NUMBER OF PAGES 148		
17. SECURITY CLASSIFICATION OF REPORT UNCLASSIFIED			16. PRICE CODE		
18. SECURITY CLASSIFICATION OF THIS PAGE UNCLASSIFIED		19. SECURITY CLASSIFICATION OF ABSTRACT UNCLASSIFIED		20. LIMITATION OF ABSTRACT SAR	

## GENERAL INSTRUCTIONS FOR COMPLETING SF 298

The Report Documentation Page (RDP) is used in announcing and cataloging reports. It is important that this information be consistent with the rest of the report, particularly the cover and title page. Instructions for filling in each block of the form follow. It is important to *stay within the lines* to meet optical scanning requirements.

**Block 1. Agency Use Only (Leave blank).**

**Block 2. Report Date.** Full publication date including day, month, and year, if available (e.g. 1 Jan 88). Must cite at least the year.

**Block 3. Type of Report and Dates Covered**  
State whether report is interim, final, etc. If applicable, enter inclusive report dates (e.g. 10 Jun 87 - 30 Jun 88).

**Block 4. Title and Subtitle** A title is taken from the part of the report that provides the most meaningful and complete information. When a report is prepared in more than one volume, repeat the primary title, add volume number, and include subtitle for the specific volume. On classified documents enter the title classification in parentheses.

**Block 5. Funding Numbers.** To include contract and grant numbers; may include program element number(s), project number(s), task number(s), and work unit number(s). Use the following labels:

C - Contract	PR - Project
G - Grant	TA - Task
PE - Program Element	WU - Work Unit Accession No.

**Block 6. Author(s)** Name(s) of person(s) responsible for writing the report, performing the research, or credited with the content of the report. If editor or compiler, this should follow the name(s).

**Block 7. Performing Organization Name(s) and Address(es)** Self-explanatory.

**Block 8. Performing Organization Report Number** Enter the unique alphanumeric report number(s) assigned by the organization performing the report.

**Block 9. Sponsoring/Monitoring Agency Name(s) and Address(es)** Self-explanatory.

**Block 10. Sponsoring/Monitoring Agency Report Number. (If known)**

**Block 11. Supplementary Notes.** Enter information not included elsewhere such as: Prepared in cooperation with...; Trans. of...; To be published in.... When a report is revised, include a statement whether the new report supersedes or supplements the older report.

**Block 12a. Distribution/Availability Statement.** Denotes public availability or limitations. Cite any availability to the public. Enter additional limitations or special markings in all capitals (e.g. NOFORN, REL, ITAR)

DOD - See DoDD 5230.24, "Distribution Statements on Technical Documents."

DOE - See authorities.

NASA - See Handbook NHB 2200 2.

NTIS - Leave blank.

**Block 12b. Distribution Code.**

DOD - Leave blank.

DOE - Enter DOE distribution categories from the Standard Distribution for Unclassified Scientific and Technical Reports.

NASA - Leave blank.

NTIS - Leave blank.

**Block 13. Abstract.** Include a brief (*Maximum 200 words*) factual summary of the most significant information contained in the report.

**Block 14. Subject Terms.** Keywords or phrases identifying major subjects in the report.

**Block 15. Number of Pages.** Enter the total number of pages.

**Block 16. Price Code.** Enter appropriate price code (*NTIS only*).

**Blocks 17. - 19. Security Classifications.** Self-explanatory. Enter U.S. Security Classification in accordance with U.S. Security Regulations (i.e., UNCLASSIFIED). If form contains classified information, stamp classification on the top and bottom of the page.

**Block 20. Limitation of Abstract.** This block must be completed to assign a limitation to the abstract. Enter either UL (unlimited) or SAR (same as report). An entry in this block is necessary if the abstract is to be limited. If blank, the abstract is assumed to be unlimited.

## ACKNOWLEDGMENTS

The author is indebted to Dr. Pei Chi Chou of Drexel University for attempting to convey to the author, through example, those things necessary in becoming a good engineering researcher. The author is likewise grateful to Dr. W.P. Walters of the Ballistic Research Laboratory and Drs. C.W. Lau, T.M. Tan, and H. Rogers of Drexel University. Many colleagues of the author were helpful in providing relevant technical discourse, moral support, and friendship. They included Dr. W. Walters, Mr. R. Ciccarelli, Dr. W. Flis, Dr. J. Zukas, Mr. D. Silvia, Dr. N. Huffington, Mr. R. Jameson, Dr. L. Wu, Dr. A. Dietrich, and Dr. C.W. Kitchens. There are countless others who assisted in this regard.

Additional assistance was provided to the author in many forms. Mr. M. Labriola of Dyna East Corp. provided the author with rotary forged tensile specimens necessary for one phase of the research. Mr. R. Franz and Ms. D. Montiel instructed the author in the use of BRL's tensile testing machine. A number of the illustrative renderings were performed by Ms. M. Scarborough and the graphic arts team, both of BRL.



Accession For	
NTIS CRA&I	<input checked="" type="checkbox"/>
DTIC TAB	<input type="checkbox"/>
Unannounced	<input type="checkbox"/>
Justification	
By	
Distribution/	
Availability Codes	
Dist	Avail and/or Special
A-1	

INTENTIONALLY LEFT BLANK.

## TABLE OF CONTENTS

	<u>Page</u>
ACKNOWLEDGEMENTS . . . . .	iii
LIST OF FIGURES . . . . .	vii
LIST OF TABLES . . . . .	xi
<b>1 INTRODUCTION . . . . .</b>	<b>1</b>
1.1 The Conical Shaped Charge . . . . .	1
1.2 Shear Forming for Spin Compensation . . . . .	3
1.3 Spin Compensation . . . . .	5
1.3.1 Shear Forming . . . . .	9
1.3.2 Fluting . . . . .	9
1.3.3 Electroforming . . . . .	12
<b>2 THE EFFECT OF CHARGE ROTATION UPON SHAPED-CHARGE JET FORMATION . . . . .</b>	<b>12</b>
2.1 Analysis . . . . .	13
2.2 Comparison with Experiment . . . . .	15
<b>3 RESIDUAL STRESS . . . . .</b>	<b>16</b>
3.1 Residual Stress Mode 1: Circumferential Acceleration after Jetting . . . . .	23
3.2 Residual Stress Mode 2: Circumferential Acceleration after Liner Shock . . . . .	26
3.3 Residual Stress: Summary . . . . .	30
<b>4 ANISOTROPY . . . . .</b>	<b>30</b>
4.1 Determination of Anisotropic Mechanical Properties . . . . .	32
4.1.1 Metallurgical Determination of Properties . . . . .	33
4.1.2 Experimental Determination of Properties . . . . .	35
4.1.3 Tensile Test Results . . . . .	37
4.1.4 Tensile Test Analysis . . . . .	42

	<u>Page</u>
4.1.5 Tensile Test Conclusions .....	50
4.2 Analytical Studies .....	51
4.2.1 Elastic vs. Plastic Anisotropy .....	53
4.2.2 Collapsing Anisotropic Liner Element .....	58
4.2.3 Shear Coupling .....	58
4.3 Computational Studies .....	65
4.3.1 Plane Stress Collapse of Anisotropic Cylinders .....	66
4.3.2 Axisymmetric Code Validation .....	75
4.3.3 Axisymmetric Collapse of an Anisotropic Liner .....	75
5 CONCLUSIONS AND RECOMMENDATIONS .....	84
6 LIST OF REFERENCES .....	88
APPENDIX A: DEVIATORIC CONSTITUTIVE RELATION FOR ANISOTROPIC MATERIALS .....	A1
APPENDIX B: ANISOTROPY DIRECTION TRACKING FOR AXISYMMETRIC SIMULATIONS .....	B1
LIST OF SYMBOLS .....	93
DISTRIBUTION LIST .....	101

## LIST OF FIGURES

		<u>Page</u>
1.	Time sequence of shaped charge collapse, with flash times indicated in microseconds after detonation at apex . . . . .	4
2.	Scaled penetration of two charges versus spin rate <sup>4</sup> . . . . .	6
3.	The shear-forming process for shaped-charge liners . . . . .	10
4.	Cross sectional view of a typical fluted liner . . . . .	11
5.	Moment of inertia relationship between a liner element and its resulting jet segment . . . . .	14
6.	Computed jet angular velocity versus jet axial velocity for a BRL 3.2 liner at 125 $\mu$ s after liner collapse . . . . .	17
7.	Maximum hoop stress in jet as a function of jet axial velocity . . . . .	18
8.	Three views of jet resulting from an 89 mm liner spun at 30 rps . . . . .	19
9.	Residual stress system under consideration, formed by welding together two flush cones after applying opposite and equal traction distributions along weld interface . . . . .	20
10.	Free body diagram of a residually stressed liner slice . . . . .	21
11.	Mode 2 stress relief, which occurs after liner shock and prior to jet formation . . . . .	24
12.	Idealized $\tau_{z\theta}$ distribution assumed for residual stress analysis . . . . .	27
13.	(110) pole figure of recrystallized low-carbon steel <sup>37</sup> . . . . .	34
14.	Types of rotary forges: (a) Type 1a if only one die is driven and one follows, Type 1b if both dies are driven; (b) Type 2, and (c) Type 3 . . . . .	36
15.	Details of rotary forged dog bone specimens used for tensile testing . . . . .	38
16.	Yield strength versus percent workpiece reduction, for three orientations of tensile specimen . . . . .	39
17.	Characteristic strength/elongation versus orientation graph for rolled copper sheet <sup>42</sup> . . . . .	41
18.	Measured values of specimen width and thickness, along with curve fit, for typical rotary forged tensile tab . . . . .	43
19.	$\pi$ -plane of a perfectly plastic anisotropic material under conditions of no shear stress. Point P denotes stress state from uniaxial stress in 1 direction. $\bar{\epsilon}^P$ denotes plastic strain vector after yield . . . . .	46

	<u>Page</u>
20. $\pi$ -plane of a material, strained to $e_j$ , prior to yield. Anisotropic stress state $s_j^A$ differs from the isotropic stress state $s_j^I$ . . . . .	52
21. $\pi$ -plane of a material, strained to $e_j$ , following yield. Anisotropic stress state $s_j^A$ rapidly approaches the isotropic stress state $s_j^I$ . . . . .	54
22. Primed 1-2-3 laboratory coordinate system used for shear velocity analysis . .	55
23. Schematic illustration of shear velocity concept, with resultant counter-rotation of jet and slug . . . . .	56
24. Cylinder geometry used to study collapse of anisotropic cylinders, under conditions of plane stress and strain . . . . .	67
25. Distorted cylinder geometry plot of plane stress cylinder at 11.2 $\mu$ s. Inner surface of cylinder has rotated 24 degrees . . . . .	68
26. Net angular velocity of liner slice ( $\omega_{net}$ ) may be acquired as a function of cumulative mass fraction (m/M) . . . . .	70
27. Net angular velocity of liner slice versus percentage of cumulative mass (m/M), for anisotropic plane stress cylinder, $\Gamma = 10$ degrees . . . . .	71
28. Net spin of inner 25 percent of liner slice, as a function of anisotropy orientation angle $\Gamma$ , for plane stress simulations at 11.2 $\mu$ s . . . . .	73
29. Limiting value and value at 11.2 $\mu$ s of net angular velocity as a function of percentage cumulative mass (m/M), for anisotropic plane stress cylinder, $\Gamma = 10$ degrees . . . . .	74
30. Initial grid geometry of the axisymmetric simulation involving the collapse of an anisotropic BRL 3.2 liner . . . . .	76
31. Deformed grid geometry of anisotropic jet, with a plot of jet angular velocity versus jet location, both at 45 $\mu$ s . . . . .	78
32. Angular velocity contour plot of anisotropic jet at 45 $\mu$ s. Unity aspect ratio has not been preserved . . . . .	79
33. Angular velocity contour plot of anisotropic jet at 25 $\mu$ s. Unity aspect ratio has not been preserved . . . . .	80
34. Angular momentum contour plot of anisotropic jet at 25 $\mu$ s. Unity aspect ratio has not been preserved . . . . .	81
35. Angular momentum contour plot of anisotropic jet at 45 $\mu$ s. Unity aspect ratio has not been preserved . . . . .	82

	<u>Page</u>
36. Time history graph of angular momentum for several points on the anisotropic BRL 3.2 liner . . . . .	83
37. Initial outline of simulation geometry, depicting material points whose angular momentums have been traced in time . . . . .	85
38. Jet spin versus axial jet velocity for unspun charge and charge spun at 35 rps opposite direction of spin compensation . . . . .	86
A-1. Schematic depiction of general anisotropic body, where principal material directions are not generally aligned with laboratory axes . . . . .	A7
A-2. Transversely isotropic material properties are derivable from orthotropic properties, when plane of material symmetry is assumed . . . . .	A8
A-3. Error in computation of hydrostatic pressure is introduced if tangent modulus is employed . . . . .	A13
B-1. Interpolation for $\theta$ within a computational element is flat in Cartesian r-z- $\theta$ space . . . . .	B4
B-2. Schematic depiction of how interpolation function for $\theta$ causes the angle between r-z plane and computational element ( $\phi^f$ ) to vary throughout element, as viewed down the z axis in cylindrical r-z- $\theta$ space . . . . .	B5
B-3. Computational element viewed in Cartesian r-z- $\theta$ space, showing all quantities needed to compute $d\theta/dl$ , and hence the angle between the r-z plane and deformed element in cylindrical r-z- $\theta$ space ( $\phi$ ) . . . . .	B7

INTENTIONALLY LEFT BLANK.

## LIST OF TABLES

	<u>Page</u>
1. Shaped Charge Liner Spin Compensation Data from the Literature . . . . .	8
2. Width to Thickness Strain Ratio ( $r$ ) and Standard Deviation ( $\sigma$ ) for Various Specimen Orientations after a 90 Percent Reduction via Rotary Forging . .	44
3. Plastic Potential Deviation Matrix $\tilde{A}_{ij}$ . . . . .	62
4. Shear to normal coupling ratios for material with yield characteristics $Y_i = \langle 3.41 \ 3.86 \ 3.86 \ 2.34 \ 2.65 \ 2.65 \rangle$ kbar . . . . .	64

INTENTIONALLY LEFT BLANK.

## 1. INTRODUCTION

This study examines the mechanism by which shaped-charge liners, when manufactured by the shear-forming process, produce jets which have the tendency to spin. In particular, both residual shear stress relief and anisotropic shear coupling are examined to determine what influence, if any, is had upon the shaped-charge collapse and subsequent jet formation processes.

Where possible, analytical models are derived which reveal quantitative information on the phenomenon of shear-formed liner collapse. For problems which are not analytically tractable, finite element computations are employed, using a specially modified version of the Lagrangian DEFEL code (discussed in Section 4.3). The modifications to DEFEL were developed as part of the current research and include a unique implementation of the Hill yield function/Prandtl-Reuss flow rule formulation for anisotropic materials. This and other code development efforts are detailed in Appendices A and B. A list of symbols used throughout this document is provided near the end of this document.

Some experimental tests have been performed during the course of this research. Though experimentation is not the focus of the research, the experimental data generated by the author as well as that drawn from other references are used to support the research in several ways: to show past efforts in the area of the current research, to show qualitative support for a proposed idea, and to provide input data to analytical models and computational simulations.

### 1.1 The Conical Shaped Charge.

Several authors<sup>1,2,3</sup> have written good introductions on the history and process of shaped-charge collapse, which may be consulted for more detail. As such, only a brief summary is provided below for the reader's convenience.

Walters<sup>1</sup> points out that the earliest reference to a hollowed charge dates to von Foerster in 1883. This hollowed charge principle became known in the U.S. as the Munroe effect, after Charles Munroe, who rediscovered the effect in 1888 for the U.S. Navy. The Munroe effect is the principle on which the modern shaped charge is based, in which the hollowed cavity is lined with a thin layer of inert material (called the liner). Upon

detonation, the focusing effect of the explosive collapses the liner into a fast traveling jet, which constitutes an effective penetrator.

In the modern axisymmetric shaped charge, the hollowed out portion of the charge generally assumes a regular geometric shape whose axis of symmetry coincides with that of the charge (two common examples for cavity shape are conical and hemispherical). This hollowed out cavity is then lined with a thin layer of inert material. Metals are typically employed, with copper being the most common choice for the liner material.

When the explosive is detonated along the liner's axis of symmetry, at the end of the charge opposite the liner, the detonation wave, as it passes over the liner, accelerates the liner forward and towards its axis of symmetry at a speed of several kilometers per second. Because the force of the detonation is very large, the strength of the liner material influences the liner collapse relatively little. Thus, the collapsing liner material behaves like a fluid. The velocity flow field established by the collapsing liner depends on many factors, including the original shape of the liner, but will be described below for the collapse of a typical point initiated conically lined shaped charge.

Liner elements adjacent to the liner apex are the first to strike the axis of symmetry, since they are the first accelerated by the detonation shock wave. In accordance with momentum and energy principles, a small fraction of the liner element from the inside surface of the liner, upon striking the axis, peels off and jets forward along the axis of symmetry. The velocity of the jet can be quite large, approaching ten kilometers per second. When viewed from the forward moving stagnation point of the collapsing liner, this jetting phenomenon is not unlike the situation of squirting a hose at an angle with respect to the pavement: a small portion of the water jets back along the pavement in the direction of the incoming stream. As subsequent liner elements, progressing from liner apex to base, successively strike the axis of symmetry, a similar splitting of the liner occurs for each element. The result is a continuous stream of jetting material along the axis of symmetry for the duration of the liner collapse. This jet constitutes an effective penetrating element, capable of penetrating through rock, steel, or other materials in its path. The slow moving portion of the collapsed liner which does not jet forward in this coordinate system is called the slug. Though the slug constitutes the bulk of the original liner mass (approximately 80 percent), its relatively slow speed (less than a kilometer per second) prevents it from being an effective penetrator against rock and steel. A time sequenced

set of photographs are shown in Figure 1, which depict the progression of conical liner collapse, as well as jet and slug formation.

One final issue which will be addressed regarding the formation of shaped-charge jets concerns the velocity distribution along the jet. For the case of the conical cavity shaped charge presently under discussion, there is less explosive accelerating liner elements near the base of the conical liner compared with those at the apex. As such, the collapse and subsequent jetting velocities of these elements is smaller than those from those liner elements previously jetted from the liner apex. The practical consequence of this velocity gradient is that the shaped-charge jet stretches in time, under its own inertia. The stretching process continues until such time that the jet can undergo no further axial stretch and breaks up into a sequence of discrete jet particles.

## 1.2 Shear Forming for Spin Compensation.

During the 1950's, most military shaped-charge projectiles were fired from rifled barrels, which caused the projectiles to spin. A spinning projectile is necessary to provide aerodynamic stability. However the spinning, which enhances the ability to get a projectile to its intended target, adversely affects the functioning of shaped-charge projectiles. When detonated, the spinning shaped-charge projectile naturally produces a spinning jet. It was discovered that the penetration capability of a spinning jet degraded with increasing amounts of rotation. Means were sought to compensate for the spin of the projectile in such a way as to produce a non-rotational jet from a spinning charge.

Several means were devised which would produce a spinning jet from a non-rotational charge, though the mechanisms behind this behavior were not well understood. Three such techniques involved modification of the shaped charge liner and included fluting, shear forming, and electroforming. These techniques are described in greater detail in subsequent sections of this chapter. When the sense of this built-in spin was employed opposite the natural spin of barrel rifling, the penetration characteristics of the resultant jet could be brought back to a level approaching that of a non-rotational jet. This technique of negating the effect of projectile spin is called spin compensation.

One of the techniques mentioned above for providing spin compensation to conically lined shaped charges involves manufacturing the liner with the shear-forming process. The

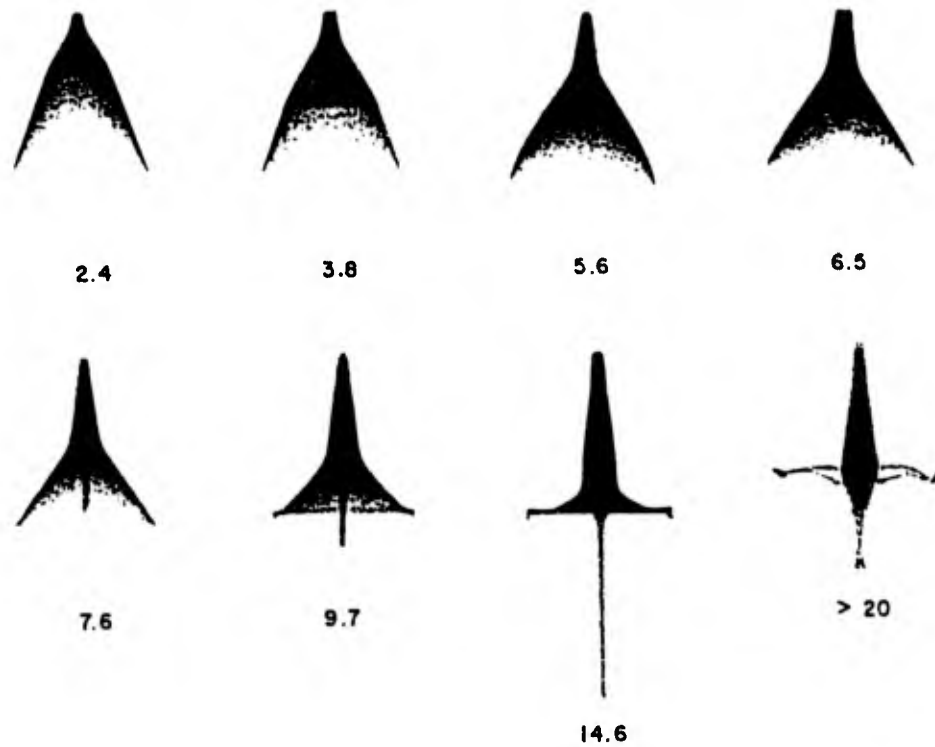


Figure 1. Time sequence of shaped charge collapse, with flash times indicated in microseconds after detonation at apex.

original theories contended that this shear-forming process introduced spin compensation through one or more of several means. One popular notion asserted that residual stress locked in the liner at manufacturing time was relieved during liner collapse to produce compensating characteristics in the jet. Another notion held that metallurgical anisotropies were introduced into the liner at the time of manufacture and that these anisotropies manifested themselves during collapse in the form of spin compensation.

The best analyses done at the time on the nature of shear-formed spin compensation were semi-empirical, in that knowledge on the behavior of single crystals was used to infer the macroscopic spin compensation properties of shear-formed liners. Because global quantities like angular momentum were not rigorously conserved in the early analyses, speculation on the compensation mechanisms of shear-formed liners remained generally uncertain.

It is the purpose of the present study to investigate the nature of the shear-formed liner collapse process from a macro-mechanical perspective; that is to say, a continuum mechanics viewpoint will be adopted to study the various mechanisms purported to effect spin compensation. Metallurgical and/or micro-mechanical phenomena are studied only insofar as they provide insight and/or data to be used in the continuum (macro-mechanical) model. The ultimate goal of this research is to ascertain which of the two mechanisms, residual stress or mechanical anisotropy, dominates the spin compensation process in shear-formed liners.

### 1.3 Spin Compensation.

The notion of shaped-charge spin compensation arose in the 1950's when it was observed that the penetrating ability of a given shaped charge decreased when the charge was subjected to a spin prior to detonation. A spinning round is employed to provide aerodynamic stability. Several methods were discovered which could compensate for this penetration degradation, and are discussed in the following sections of this document. Figure 2 depicts the scaled penetration of two 57 mm liners versus the scaled spin rates of the charge.<sup>4</sup> The liner manufactured with the drawing process, does not exhibit compensation properties, and has a maximum penetration when no rotation is present. Penetration values dropped off as the charge was spun in either direction.

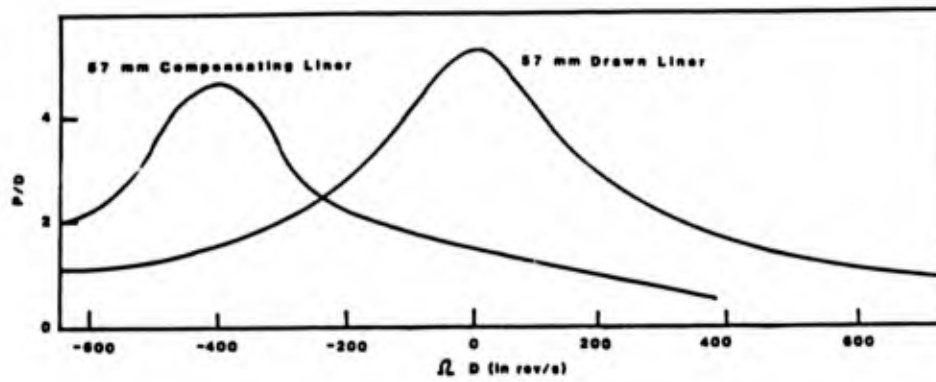


Figure 2. Scaled penetration of two charges versus spin rate.<sup>4</sup>

On the other hand, the liner manufactured to exhibit spin compensation has the peak of its penetration versus spin rate curve at a non-zero value of charge spin. As shown in Figure 2, the shape of the compensated curve takes the same general shape as the uncompensated curve, except that it is shifted and may possess a slightly lower peak value of penetration. The value of spin compensation is defined as the charge spin rate at which penetration is maximized. Different liner designs are able to compensate for different magnitudes of spin. For ordnance situations, the optimal design to choose for a given application would have as a compensation value the negative of the designed projectile spin rate.

Unfortunately though, there are practical limits on the spin magnitudes for which compensation is viable. The upper limit on the compensation magnitude is not only dependent on the compensation technique (e.g., shear forming, fluting, etc.) but also on the liner size. Zernow<sup>5</sup> points out that the scaling law for geometrically similar charges dictates that the quantity ( $\Omega D$ ) be constant, where  $\Omega$  is the charge spin rate and  $D$  is the charge diameter. However, the validity of such a relation hinges on the spin compensation mechanism scaling geometrically too. For some methods of spin compensation, like liner fluting, it seems quite plausible that the compensation mechanism scales geometrically. On the other hand, shear-formed and electroformed liners, which also exhibit spin compensation behavior, seem less likely to scale geometrically, since the compensation mechanisms are more closely related to the metallurgical grain structure within the liner, where geometric scaling does not necessarily hold.

Various data are presented in Table 1, which represent a reasonably comprehensive compilation of compensating liner data.<sup>4,6-18</sup> Upon examination of the scaling parameter  $\Omega D$ , one observes a fair amount of scatter in the data, particularly amongst the fluted liners. This scatter is not unexpected since the data also indicates that the liners in question are not precise geometric scales, as witnessed by the variable diameter to wall thickness ratios. Nonetheless, the data of Table 1 give an indication of expected spin compensation magnitudes. For shear formed liners, which are the topic of the current research, an average value of scaled compensation frequency ( $\Omega D$ ) is found to be 2,850 mm rps. This value will be important during subsequent analyses, since it may be used to compute the expected compensation frequency of a typical shear formed liner of arbitrary diameter.

TABLE 1. Shaped Charge Liner Spin Compensation Data from the Literature.

Liner Type	Liner Diameter D (mm)	Liner Thickness t (mm)	Diameter to Thickness Ratio D/t	Spin Compensation $\Omega$ (rps)	$\Omega$ D (mm rps)	Ref.
Fluted:						
	41			180	7380	4
	41			250	10250	4
	41	1.22	33.9	185	7585	10
	41			150	6150	9
	59*	1.75	33.7	140	8260	11
	72	2.66	27.1	95	6840	16
	89	2.66	33.5	50	4450	12
	89			30-45	2670-4005	6
	89			50	4450	4
	96	3.56	27.0	65	6240	14
	96	3.56	27.0	65	6240	16
Shear Formed:						
	74			25-35	1850-2590	18
	89			30-45	2670-4005	7
	89			30-45	2670-4005	15
	89	2.66	33.5	30	2670	13
	89			26	2314	4
Electroformed:						
	89	2.41	36.9	30	2670	17
	89			45	4005	8
	89			45	4005	15

\*liner diameter not explicitly mentioned, but inferred from following data:

-projectile diameter = 75 mm,

-projectile dia. exceeds charge dia. by 16 mm in both 57 mm and 105 mm charges, and

-59 mm liner dia. makes the liner a geometric scale of 57 mm and 105 mm charges.

### 1.3.1 Shear Forming.

As mentioned above, the shear forming of shaped-charge liners provides a means to compensate for charge spin. Shear forming is commonly known by several other names which include rotary extrusion, spin forming, shear spinning, and flow turning. The shear-forming process, for shaped-charge liner manufacture, has been employed for nearly 30 years.<sup>1,18-20</sup> Essentially, the process is employed to produce axisymmetric forms by pressing a rotating tool against a rotating workpiece (originally in the shape of a flat disk), so that the workpiece deforms and assumes the shape of the mandrel (Figure 3). For compensating shaped-charge liners, the mandrel is conical in shape. The shape of the mandrel governs the profile of the inner surface of the deformed workpiece, and the path of the tool determines the outer profile of the deformed workpiece, the final thickness of the workpiece being determined by the preset spacing between the final tool path and the mandrel.

### 1.3.2 Fluting.

Another means to compensate for charge spin, which was mentioned above, is a technique known as liner fluting. Historically the most popular means of providing spin compensation, fluting a liner involves the introduction of surface contours to the liner known as flutes. A fluted liner still retains the basic shape of the liner (e.g., conical), but has periodic, controlled variations in the inner and/or outer surface of the liner. A cross section of a typical fluted liner is shown in Figure 4, where the surface variations known as flutes are clearly seen.

Spin compensation by fluted liners was studied extensively by Eichelberger and Pugh<sup>4</sup> in the 1950's. By appropriate design of flutes, they deduced that rotation could be induced in shaped-charge jets. However, the magnitude and even directional sense of compensation varied with flute design in a way which was not well understood. Recently, Weickert and Chou<sup>2,21</sup> have employed finite element techniques to model the collapse of fluted liners, in which they conclude that liner and explosive are counter-rotating. Lagrangian mesh distortion forced computation to be halted prematurely, so that determination of the angular momentum partition between jet and slug was impossible.

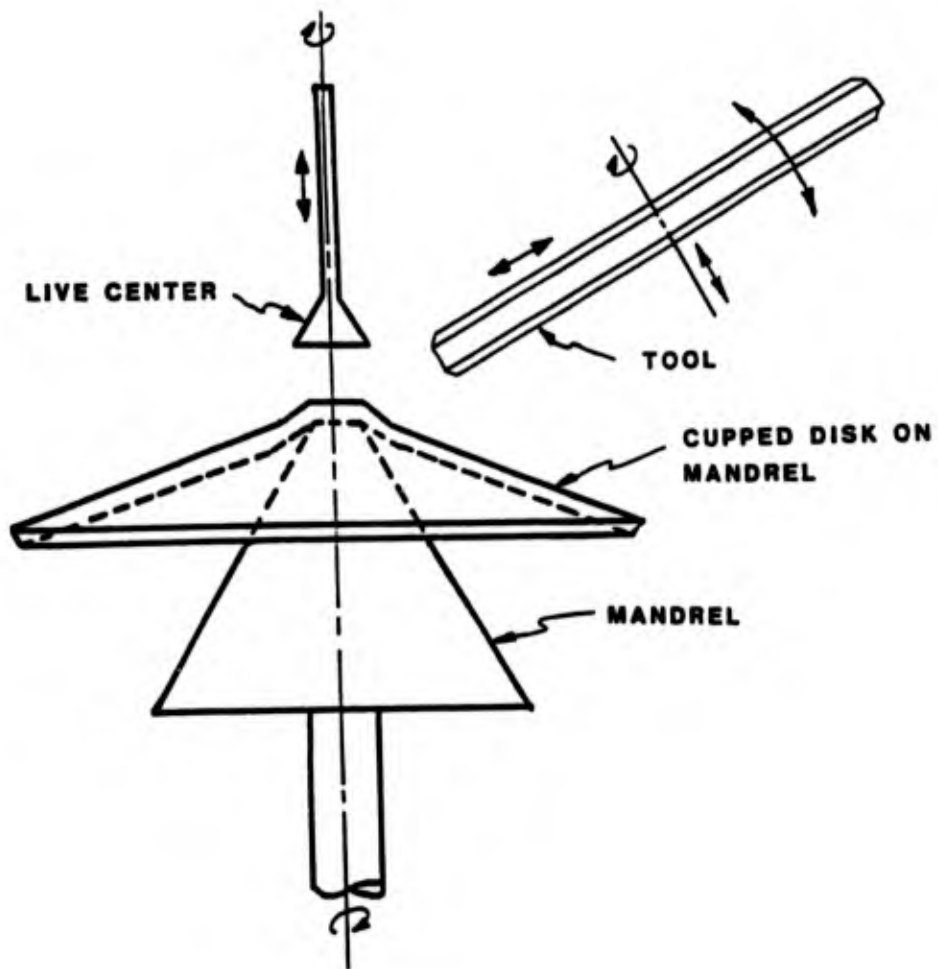


Figure 3. The shear-forming process for shaped-charge liners.

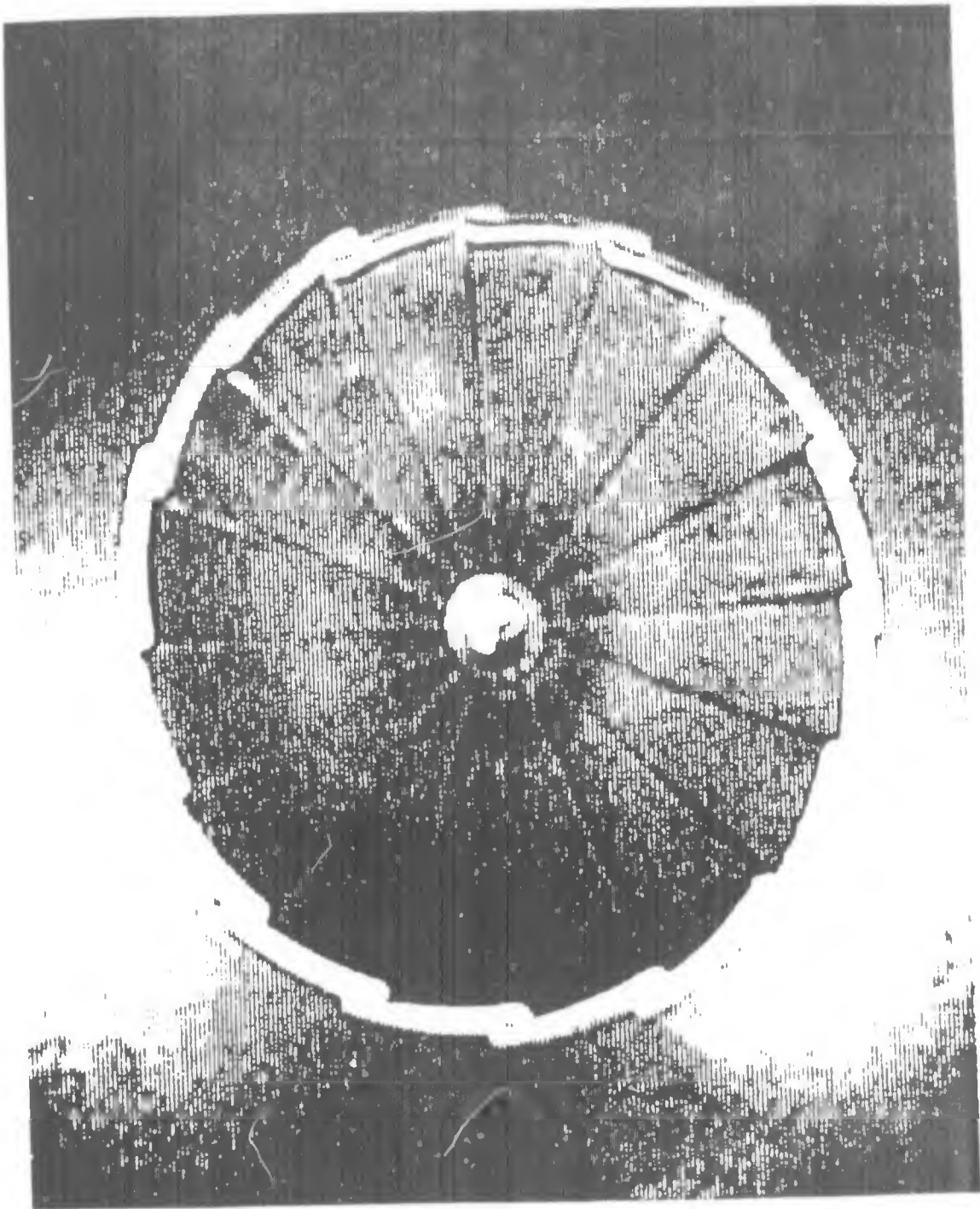


Figure 4. Cross sectional view of a typical fluted liner.

### 1.3.3 Electroforming.

The final technique, which was mentioned above, used to compensate liners for charge spin involves electroformation. Electroformed liners are manufactured by way of the electrodeposition process. With this process, a rotating mandrel, whose shape corresponds to the inner surface of the desired liner, is immersed in electrolytic fluid containing ions of the liner material. When current is passed to the mandrel, by way of the working fluid, ions of the liner material in the solution are deposited on the mandrel. When the deposited thickness of liner material is sufficient, the process is complete and the electrodeposited liner may be machined to final tolerances. Presumably because of the rotation of the mandrel, electroformed liners exhibit spin compensation behavior. The mechanism is surmised to be metallurgical in nature, which manifests itself in the form of anisotropy. Though little, if any, theoretical work has been done on the compensation mechanisms of electroformed liners, Simon and Zernow<sup>8,15</sup> have experimentally demonstrated the ability of electroformed liners to compensate to a degree similar to shear formed liners.

Though the present research concerns itself with shear-formed liners, much of the work, as it pertains to the mechanism of anisotropy, are relevant to the topic of spin compensation in electroformed liners as well.

## 2. THE EFFECT OF CHARGE ROTATION UPON SHAPED-CHARGE JET FORMATION

Interest in spin compensation was aroused when it was found that shaped charges experience a degradation in penetration as a direct result of spinning the charge. Since many shaped charges for military application were found in projectiles which were fired from rifled barrels, considerable resources were allocated by the military during the 1950's to study the issue of spinning jets and spin compensation.

When a projectile is fired from a rifled barrel, it acquires a spin rate which is dependent on both the muzzle velocity and the amount of rifling. Typical projectile spin rates fall in the 35 to 250 revolutions per second (rps) range. Were a shaped-charge jet subjected to such modest rotation rates, penetration degradation would not be a problem. However, the liner collapse process takes liner material from a radius on the order of

magnitude of the projectile diameter, and concentrates it along a jet, whose diameter may approach as little as 1 percent of the projectile diameter. Under these conditions, the jet will attempt to acquire a very large rate of rotation (tens of thousands of rps), in accordance with principles governing the conservation of angular momentum.

Unfortunately, the stresses that build up in a jet particle, as a result of excessive rotation rates, can exceed the yield strength of the material. Under these circumstances, the jet particle may split into two or more fragments (bifurcate or polyfurcate), each expanding radially from the axis of symmetry. It is this radial fragmentation of the jet which results in the degraded penetration.

## 2.1 Analysis.

In order to evaluate the conditions required for jet bifurcation, one must evaluate the stress acting on a rotating jet particle. The angular velocity of the jet particle must, however, be ascertained first. To this end, both the Ballistic Research Laboratory (BRL)<sup>22</sup> and Dyna East Corporation<sup>23</sup> have studied the influence of spin upon the collapse of, and stress state within, a cylindrical ring (meant to simulate a collapsing liner element). In the BRL study, the thickness of the ring was ignored, which precluded the ring from ever collapsing fully to the axis. In the Dyna East study, the thickness of the ring was retained, but was assumed thin enough so that the radial component of stress was identically zero. In the current analysis, neither of these limiting assumptions apply. The only assumption currently made is the assumption of an infinitesimal void within a forming jet element. This assumption was not necessary for the solution of the problem, but instead offers a worst case scenerio as to the stress state within the jet, since the infinitesimal void is found to introduce a stress concentration factor of two.

Figure 5 depicts the relationship between the moments of inertia for material initially in the liner, which eventually becomes a jet segment. Since the angular momentum is conserved during liner collapse, and the initial angular velocity of the charge is  $\Omega$ , then the angular velocity of the jet segment ( $\omega$ ) is given by

$$\omega = \frac{2R^2}{r_j^2} \Omega \quad , \quad (2-1)$$

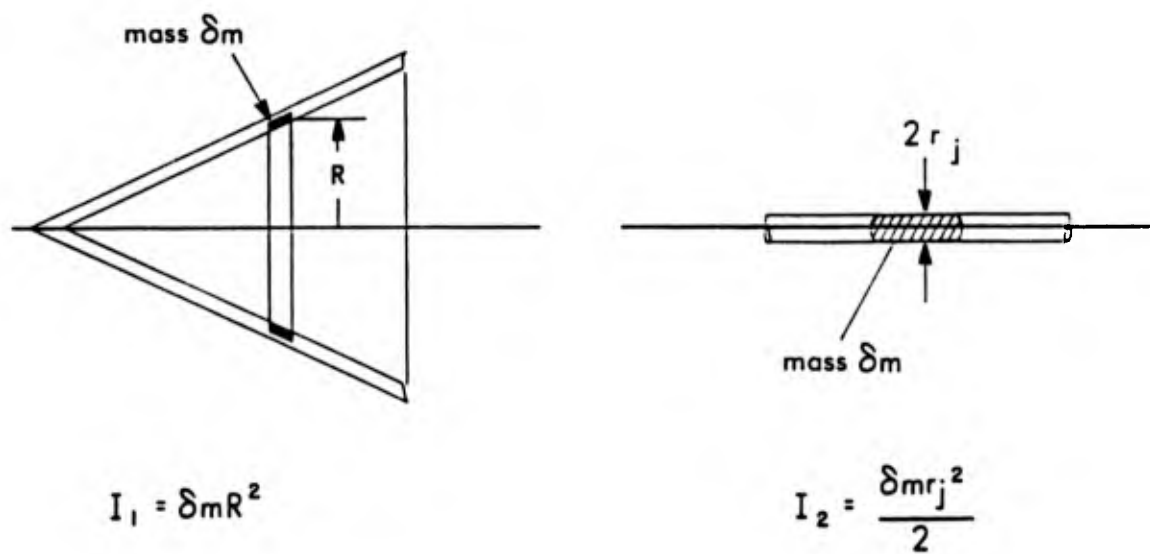


Figure 5. Moment of inertia relationship between a liner element and its resulting jet segment.

where:

$r_j$  - jet radius of element in question, and

$R$  - radius of liner element that produces jet segment of radius  $r_j$ ,

The theory of elasticity allows for the calculation of the stress distribution in the rotating jet (modeled in the worst case as a plane stress rotating disk). Knowledge of the elastic stress state within the rotating particle permits one to analyze the post-elastic behavior of the particle, when yielding is reached. If elastic incompressibility is assumed, as well as an infinitesimally small void at the center of the jet (this stress concentration factor is not an unreasonable assumption from a topological point of view), then Timoshenko<sup>24</sup> shows that the maximum stress differential occurs at the void. The Tresca yield condition implies that yielding (and thus fracture, if a perfectly plastic liner is assumed) will occur when this maximum hoop stress ( $\sigma_\theta$ ), given by

$$\sigma_\theta = \frac{7}{8} \rho \omega^2 r_j^2 \quad (2-2)$$

exceeds the yield strength of the jet. In equation (2-2), the term  $\rho$  represents the density of the liner material. This failure criterion (2-2) may be related to the original liner spin rate with the use of equation (2-1), and is given as

$$\frac{\sigma_\theta}{\Omega^2} = \frac{7}{8} \rho \frac{R^4}{r_j^2} \quad (2-3)$$

## 2.2 Comparison with Experiment.

Results of the Dyna East DESC code, were used to model the collapse of a ERII 81 mm charge, which is a 42 degree, copper lined, conical shaped charge. Values of  $(\omega/\Omega)$ , jet radius, and jet velocity have been computed along the jet at the typical jet breakup time of 125  $\mu$ s. Breakup, as it is used here, does not denote the radial bifurcation which results from excessive rotation. Rather, it refers to the normal axial partition of the jet into a discrete fragment train, which arises because of the velocity gradient present in the jet.

At the jet breakup time of  $125 \mu\text{s}$ , the maximum ratio of jet rotation rate to charge spin rate is on the order of 1,000. Zernow and Simon<sup>25</sup> were able to rotate an 89 mm copper liner to 15 rps before bifurcation occurred. If the 81 mm charge under consideration were rotated at 15 rps, then the jet should be rotating as high as 15,000 rps at breakup time. One complete rotation of a jet segment rotating at 15,000 rps takes place over the span of  $67 \mu\text{s}$ . Thus, one might expect the jet to make two complete revolutions between formation and breakup time at  $125 \mu\text{s}$ . Figure 6 portrays the projected angular velocity distribution along the jet, as a function of the jet's axial velocity. Because of the fact that the jet radius varies along the jet prior to axial breakup, the shape of the maximum hoop stress curve, plotted in Figure 7 as a function of jet velocity, is slightly different than that of angular velocity. Thus, if the failure stress of the jet were low enough, Figure 7 would indicate that the central portion of the jet would be expected to bifurcate from excessive rotation, since the stress state in this region is the highest. The fact that Figure 7 indicates that the jet should begin bifurcation in the middle of the jet agrees qualitatively with Figure 8, which portrays three views of an 89 mm liner spun at a rate of 30 rps.<sup>25</sup>

### 3. RESIDUAL STRESS

Residual stress relief in shaped-charge liners has been analyzed to determine the magnitude of jet rotation which may be imparted to a jet. In particular, it is desired to determine the likelihood that these stresses are large enough to produce the spin compensation which is experimentally evident from shear-formed liners. There exist an infinite number of residual stress systems which are feasible, though few are likely to produce spin compensation. In this analysis, a pure shear system will be studied, which seems most likely to produce spin compensation.

To imagine such a system, consider two press fitted thin-walled cones which, after being subjected to equal and opposite circumferential traction distributions at their interface, are welded together, thereby locking the stress distribution in place. Such a system is shown in Figure 9, where the surface traction per unit area, after welding, becomes the residual shear stress distribution  $\tau_{r,\theta}$  at the interface. If the quantity  $\delta$  represents the normal wall thickness of the inner cone, and the cone taper is small enough where the cone surface normal  $r'$  can be approximated by the radial vector  $r$ , then the equilibrium relation for a slice from the inner cone (the free body diagram of which is depicted in Figure 10) is approximated to the first order by

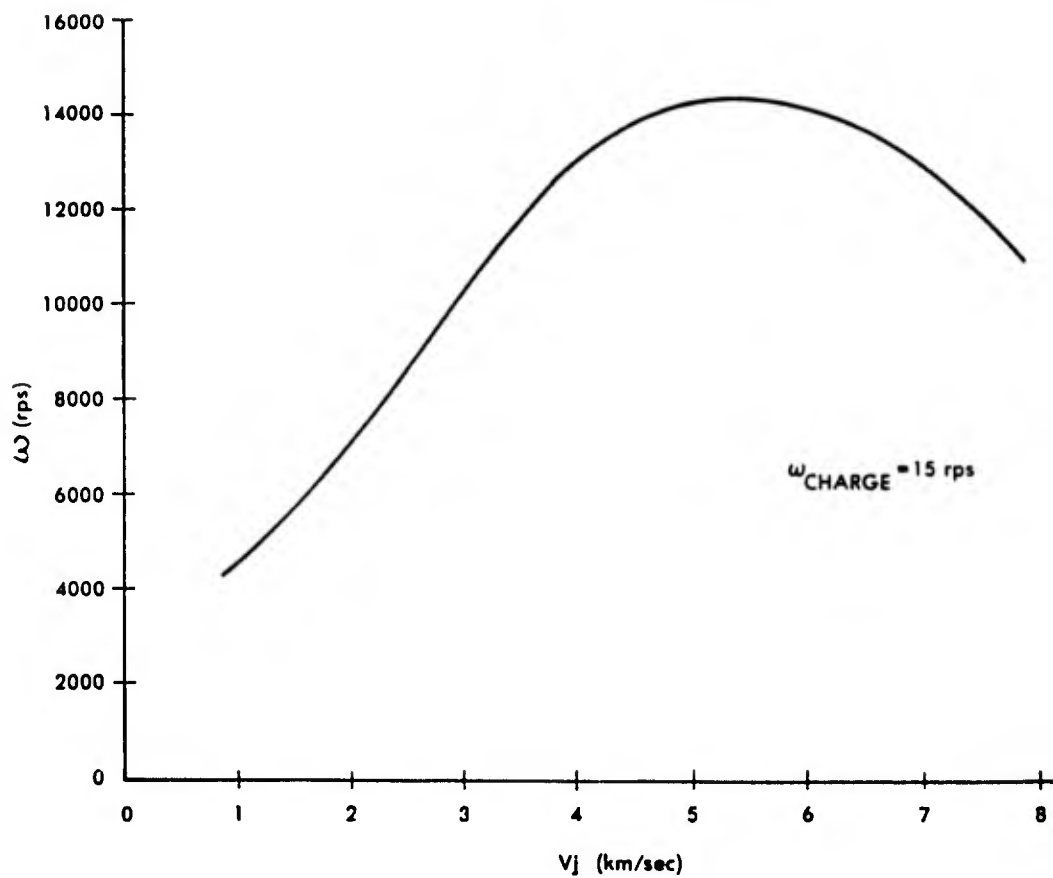


Figure 6. Computed jet angular velocity versus jet axial velocity for a BRL 3.2 liner at 125  $\mu$ s after liner collapse.

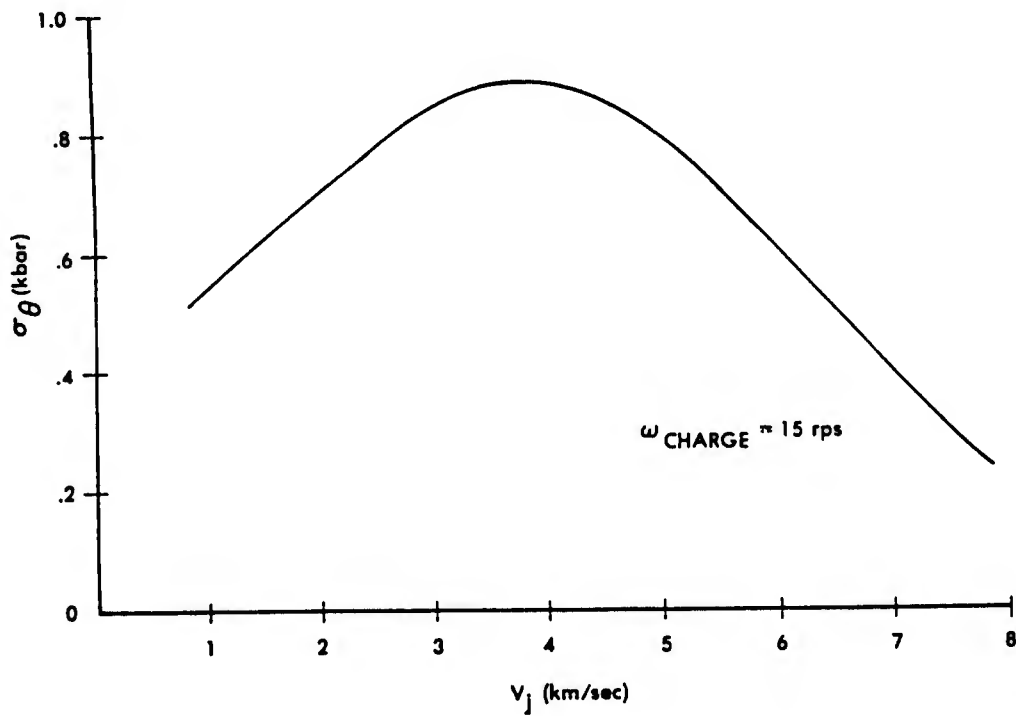


Figure 7. Maximum hoop stress in jet as a function of jet axial velocity.

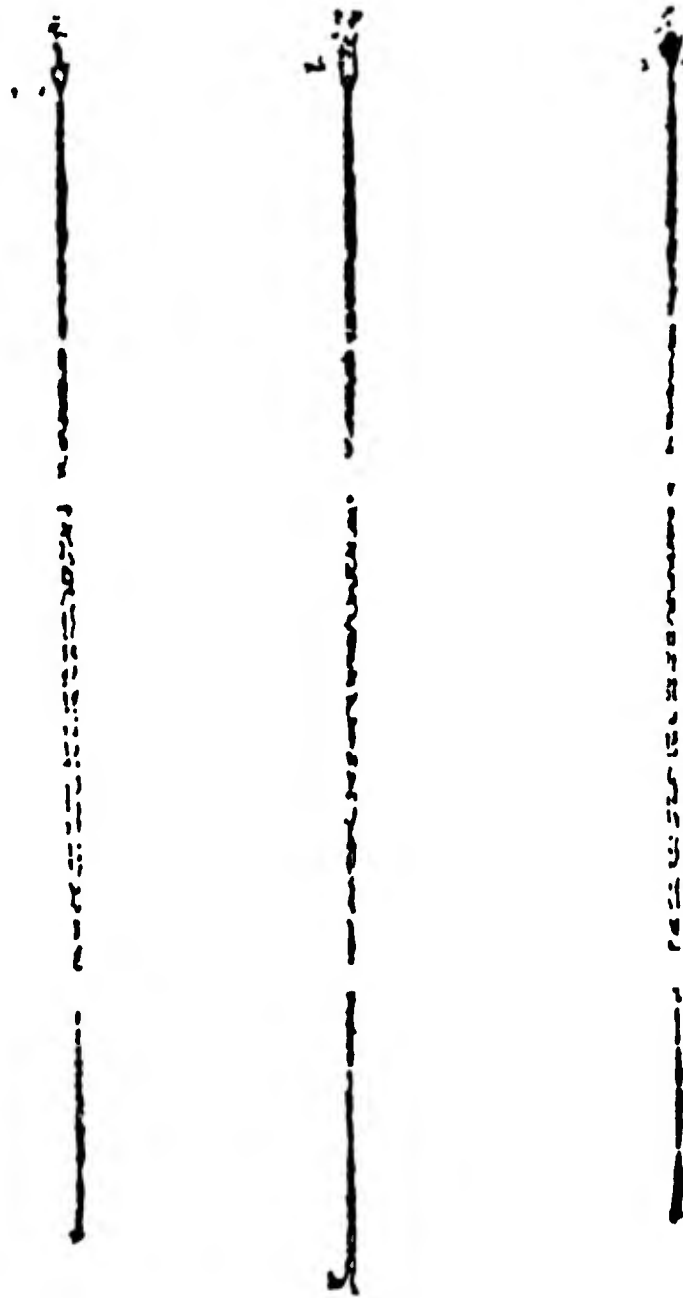


Figure 8. Three views of jet resulting from an 89 mm liner spun at 30 rps.

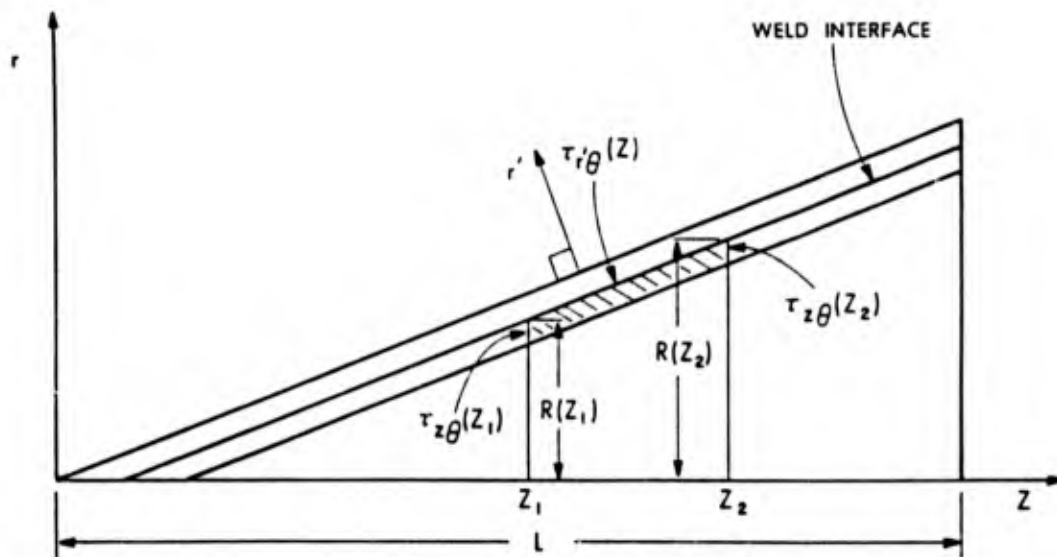


Figure 9. Residual stress system under consideration, formed by welding together two flush cones after applying opposite and equal traction distribution along weld interface.

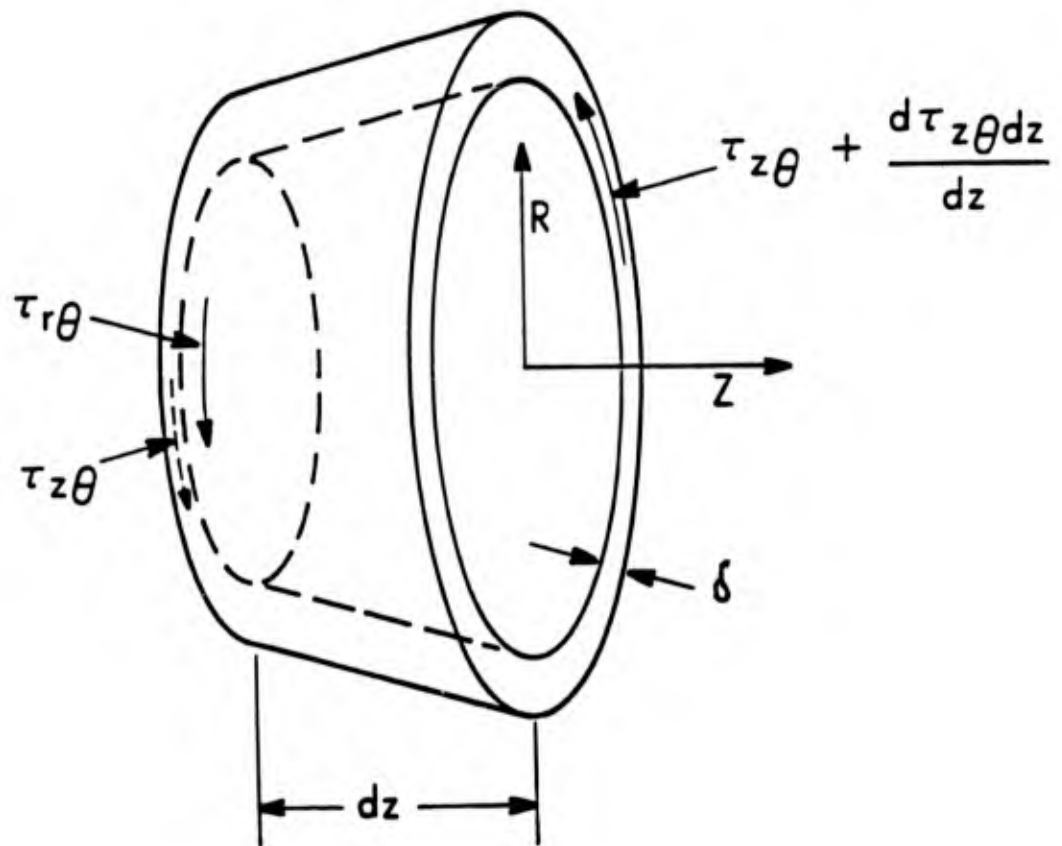


Figure 10. Free body diagram of a residually stressed liner slice.

$$\frac{d\tau_{z\theta}}{dz} = -\frac{\tau_{r\theta}}{\delta} \quad (3-1)$$

Thus, specification of a  $\tau_{r\theta}$  distribution will yield a  $\tau_{z\theta}$  distribution immediately. If  $\tau_{z\theta}$  does not fluctuate wildly in  $z$ , then an order of magnitude analysis reveals that

$$\tau_{r\theta} = O\left(\frac{\delta \tau_{z\theta}}{L}\right) \quad (3-2)$$

where  $L$  is the length of the cone. Thus, if the cone assumes the dimensions of a typical shaped-charge liner, where  $\delta \ll L$ , it is obvious that  $\tau_{r\theta} \ll \tau_{z\theta}$  so that  $\tau_{z\theta}$  will be the limiting stress when yield conditions are taken into consideration. Thus, an approximation to the von Mises yield condition is

$$k = (\tau_{z\theta}^2 + \tau_{r\theta}^2)^{(1/2)} \approx \tau_{z\theta} \quad (3-3)$$

where  $k$  is yield strength in simple shear.

In trying to evaluate the nature of spin compensation that might occur as a result of residual stresses, one must consider how the residual stresses might release themselves upon liner collapse. For purposes of illustration, the weld line of our two cone system will be taken to be the split line of the shaped-charge liner (i.e., that imaginary contour in the liner that separates material which will become jet from that which will become slug). Two possibilities exist, both of which consider stress relief following the removal of the welded interface of the two cone system:

**Mode 1:** after the liner element reaches the axis of symmetry and splitting occurs (i.e., the jet/slug interface disappears),  $\tau_{r\theta}$  can no longer resist torque and  $d\tau_{z\theta}/dz$  accelerates the forming jet circumferentially; or

**Mode 2:** as the liner element undergoes the initial shock of detonation, a spallation occurs on the inner skin of the liner, thus forcing the  $\tau_{r\theta}$  distribution to zero and allowing

$d\tau_{z\theta}/dz$  to circumferentially accelerate the liner during the collapse process. This mode of stress relief is depicted in Figure 11.

It will be shown that mode 2 has the potential to accelerate the liner to a greater degree, because the stresses accelerating the inner skins of the liner occur at a much larger radius than in mode 1, thus implying a larger accelerating torque. For both modes, the governing relationship is

$$T = \frac{d(I\omega)}{dt} \quad (3-4)$$

where T is the accelerating torque and I is the moment of inertia of the circumferential liner element.

### 3.1 Residual Stress Mode 1: Circumferential Acceleration after Jetting.

During the stress relief that occurs after jetting, it will be assumed that the jet segment's radius (and therefore its moment of inertia) does not change significantly. Though this assumption is not strictly true, the quantitative evaluation which follows this analysis computes the moment of inertia based on the smallest jet radius (that which occurs at jet breakup), which will in fact tend to yield the largest values of jet rotation rate (the liberal estimate). Equation (3-4) thus reduces to

$$\omega = \frac{1}{I} \int_0^{\Delta t} T dt \quad (3-5)$$

Furthermore, if the accelerating torque is assumed to be linearly decaying during the duration of stress relief  $\Delta t$ , from a value of  $T_0$  to 0, then the jet's final angular velocity may be expressed as

$$\omega = \frac{T_0 \Delta t}{2 I} \quad (3-6)$$

Upon jet formation, the liner segment originally of length  $\Delta z$  has stretched during liner collapse and jet formation to length  $\Delta \xi$ . The unbalanced stress across this jet element however, is still  $d\tau_{z\theta}/dz \Delta z$ . If one assumes that this unbalanced stress acts uniformly over

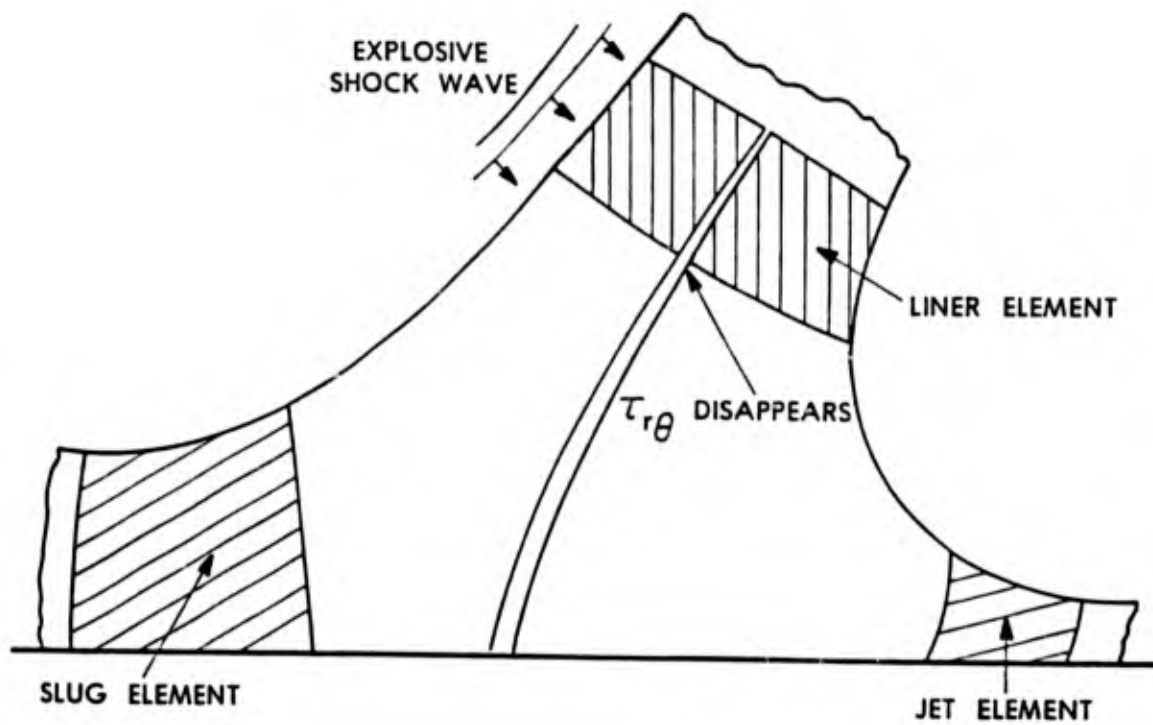


Figure 11. Mode 2 stress relief, which occurs after liner shock, and prior to jet formation.

the whole jet cross section, of radius  $r$ , then the accelerating moment on the jet segment of length  $\Delta\xi$  is given by

$$T_o = \frac{2\pi}{3} r_j^3 \frac{d\tau_{z\theta}}{dz} \Delta z \quad (3-7)$$

The moment of inertia of the jet segment under consideration is simply

$$I = \frac{1}{2} \rho \Delta\xi \pi r_j^4 \quad (3-8)$$

Thus, one may employ equations (3-5)-(3-8) to determine the angular velocity of the jet particle:

$$\omega = \frac{2}{3} \frac{(d\tau_{z\theta}/dz)\Delta t}{\rho r_j} \frac{\Delta z}{\Delta\xi} \quad (3-9)$$

By applying the principle of mass continuity, the jet radius  $r_j$ , appearing in equation (3-9), may be ascertained in terms of the liner segment's initial radius  $R$ , liner thickness  $\delta$ , the liner half angle  $\alpha$ , the liner and jet segment lengths  $dz$  and  $d\xi$ , and the liner segment mass fraction ( $f$ ) which eventually forms into jet. The expression for  $r_j$  is

$$r_j = \left( \frac{2 R f \delta}{\cos \alpha} \frac{\Delta z}{\Delta\xi} \right)^{(1/2)} \quad (3-10)$$

Equations (3-9) and (3-10) may be combined to express the jet angular velocity ( $\omega$ ) of the formed jet segment as a result of mode 1 residual stress relief:

$$\omega = \frac{\sqrt{2}}{3} \frac{(d\tau_{z\theta}/dz)\Delta t}{\rho} \left( \frac{\cos \alpha}{R f \delta} \frac{\Delta z}{\Delta\xi} \right)^{(1/2)} \quad (3-11)$$

It is unlikely that residual stress relief would occur for a long period of time following jet formation. However, a liberal assumption will be made in which stress relief occurs between the time of jet formation and the time of jet breakup. If we thus apply equation

(3-11) to the case of a BRL 81 mm charge (like the one analyzed in Section 2.2), a quantitative estimate may be obtained of the rotation rate likely to occur from mode 1, residual stress relief. Recall that spinning the BRL 81 mm charge at 15 rps would likely produce rotation rates as high as 15,000 rps at jet breakup time.

Figure 12 shows an idealized  $\tau_{z\theta}$  distribution which satisfies the boundary condition  $\tau_{z\theta}(L)=0$ , while attempting to maximize the effects of residual stress relief. The magnitude of the slope of the stress distribution in the region of the liner which forms the bulk of the jet ( $.4 < z/L < .9$ ) is  $(2k/L)$ , where  $k$  is the yield strength of the material in simple shear. Other measured (or calculated) parameters for the BRL 81 mm shaped-charge liner are:

duration of stress relief	: $\Delta t = 125 \mu s$
density	: $\rho = 8.9 \text{ g/cc}$
radius of typical liner element	: $R = 35 \text{ mm}$
shear strength of copper	: $k = 1.7 \text{ kbar}$
length of liner	: $L = 130 \text{ mm}$
thickness of liner	: $\delta = 1.5 \text{ mm}$
mass fraction into jet	: $f = .2$
liner half angle	: $\alpha = 21 \text{ degrees}$
breakup jet length/liner length	: $\Delta\xi/\Delta z = 6.5$

Substitution of these parameters into equation (3-11) give an angular velocity of 2,023 rad/s or 322 rps. This number is much smaller than the 15,000 rps which would be produced by the 81 mm liner rotated at 15 rps. In fact, the magnitude of spin for which this residually stressed liner element may compensate may be computed, using equation (2-1). The result is less than 1 rps. As a result of these computations, one is forced to conclude that mode 1 residual stress relief is not the primary mechanism which contributes to spin compensation in shaped charges.

### 3.2 Residual Stress Mode 2: Circumferential Acceleration after Liner Shock.

Recall, during this mode of stress relief, that the shear stress component  $\tau_{r\theta}$  disappears following shock acceleration of the liner. Such a condition would be conceivable if, for instance, the liner spalled after being shocked. For this mode of stress relief, it is assumed that acceleration occurs in a very small time frame after liner shock,

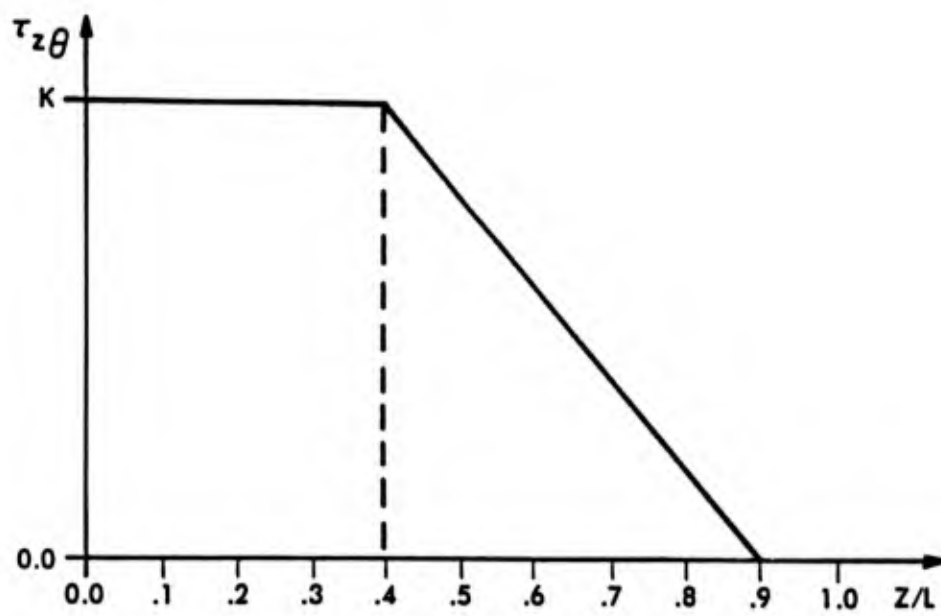


Figure 12. Idealized  $\tau_{z\theta}$  distribution assumed for residual stress analysis.

during which time the radius (and hence moment of inertia) of the liner element changes negligibly. Thus, equation (3-4) again reduces to equations (3-5), (3-6).

Note that the difference from mode 1 is the radius at which acceleration occurs (jet radius for mode 1, and liner radius for mode 2). If R is the initial radius of the liner element corresponding to a liner segment of axial length dz, then using the nomenclature of the previous section, the accelerating torque on the liner is given by

$$T_o = \left( \frac{d\tau_{z\theta}}{dz} \Delta z \right) \left( \frac{2\pi R\delta}{\cos \alpha} \right) \left( R \right) \quad (3-12)$$

The first term of equation (3-12) represents the unbalanced stress acting on the liner element. The next term is the area over which it acts, and the final term is the moment arm for the unbalanced stress. The moment of inertia of the liner segment is simply

$$I_o = \frac{2\pi \rho R^3 \delta \Delta z}{\cos \alpha} \quad (3-13)$$

Thus, the angular velocity of the liner element (see equation (3-6), which is also valid for mode 2 stress relief), while still located at radius R, is given by

$$\hat{\Omega} = \frac{(d\tau_{z\theta}/dz) \Delta t}{2 \rho R} \quad (3-14)$$

This angular velocity expressed in (3-14) is the angular velocity which a liner element possesses prior to collapse. It is, in essence, the angular spin rate for which the liner element is able to compensate. This liner element, even in the absence of additional accelerating torques, will continue to accelerate circumferentially as its radius decreases during the subsequent jet formation process, in accordance with equation (2-1). The resulting jet element acquires an angular velocity of (substituting equation (3-10) for  $r_j$ )

$$\omega = \frac{(d\tau_{z\theta}/dz) \Delta t \cos \alpha}{2 \rho f \delta} \frac{\Delta \xi}{\Delta z} \quad (3-15)$$

Making the same assumption about the  $\tau_{z\theta}$  distribution as for mode 1 stress relief, and using the typical values of parameters for the BRL 81 mm shaped charge:

duration of stress relief :  $\Delta t = 10 \mu s$   
density :  $\rho = 8.9 \text{ g/cc}$   
radius of typical liner element :  $R = 35 \text{ mm}$   
shear strength of copper :  $k = 1.7 \text{ kbar}$   
length of liner :  $L = 130 \text{ mm}$   
thickness of liner :  $\delta = 1.5 \text{ mm}$   
mass fraction into jet :  $f = .2$   
liner half angle :  $\alpha = 21 \text{ degrees}$   
breakup jet length/liner length :  $\Delta\xi/\Delta z = 6.5$  ,

equations (3-15) and (3-14) give a jet rotation rate of 4,727 rps, which equates to a charge compensation capacity of 6.6 rps. This value, though larger than that expected from mode 1 acceleration, is still much smaller than that experimentally observed from shear-formed liners.

It can be seen that the data used for mode 2 stress relief differs from that of mode 1 in one fashion: duration of stress relief is only  $10 \mu s$  as compared to  $125 \mu s$ . This difference arises because of the fact that compensation must occur during collapse, and not after jet formation. The duration of collapse seen by a liner element, from the onset of shock until jet formation, for the 81 mm charge being studied, is less than  $15 \mu s$  for the typical jet element. An assumption of the current analysis is that the jet radius does not change appreciably during the duration of circumferential acceleration. In this sense, the current analysis overestimates the compensation ability of mode 2 stress relief, because the accelerated liner element is permitted to conserve angular momentum from its initial radius  $R$ , in equation (3-15). In fact, at the conclusion of the  $10 \mu s$  acceleration, the radius of the liner element would be significantly smaller than its initial radius. As a result, conservation of angular momentum, taken from the smaller radius following acceleration, would result in less compensation ability.

### 3.3 Residual Stress: Summary.

Analyses were performed to determine the ability of a residually stressed liner to circumferentially accelerate a shaped-charge liner to produce a rotating jet. The analyses provided consider a pure shear stress state in equilibrium in which one of the shear components is disturbed by the collapse of the liner. For a mode 1 collapse, the shear stress disturbance does not occur until the jet forms at the collapse axis. For mode 2 collapse, the stress disturbance occurs when the liner is explosively shocked.

Mode 2 collapse provides for a jet with a rotational velocity approximately one order of magnitude larger than mode 1 collapse, with rotational jet velocities, at breakup, on the order of 5,000 rps. However, such rotational jet velocities, when related back to spin compensation frequencies, are only about 6 rps, and are much lower than the experimentally observed values of 30-45 rps.

Despite all the liberal assumptions taken in an attempt to make spin compensation via residual stress relief more feasible, the analyses for both modes of stress relief indicate that residual stress, if present, can not alone account for the values of spin compensation observed in shear-formed liners.

## 4. ANISOTROPY

Early on in the study of shear-formed liners, anisotropy was proposed as a possible mechanism causing spin compensation. The early attempts at understanding the shear-formed compensation phenomenon were generally performed by metallurgists, who used simple x-ray diffraction as a means of measuring the degree of anisotropy in the liner. Poulter's<sup>26</sup> technique involved aiming an x-ray beam at a liner element, in such a way that the beam was coplanar with the liner axis of symmetry. The angle formed between the beam and the liner was fixed, and the intensity of the diffracted beam was measured (at a particular reflection angle) as the liner was rotated, so that diffraction measurements were acquired around the complete circumference of the liner. Variations in the reflected intensity were indicative of anisotropy, and qualitative parallels were drawn between this measured anisotropy and subsequent jet performance.

Though Poulter's technique may have helped to enhance understanding of the spin compensation process, it failed to draw any quantitative conclusions regarding the spin compensation frequency. Possibly for this reason, Simon and Martin<sup>18</sup> approached the problem differently. Their technique involved scribing a radial line on the liner blank (the disk-shaped piece of metal prior to shear forming) and measuring the angle which this scribe mark rotated circumferentially during the shear-forming process. This deformation angle is a crude measure of the shear strain introduced into the liner during the forming process. They then correlated empirically the deformation angle to the spin compensation frequency of the liners under consideration.

Later attempts aimed at correlating anisotropy to spin compensation were performed by Gainer, Glass, and Moss<sup>19,20</sup> who used an x-ray diffraction technique. Their study was much more comprehensive than earlier studies, in that x-ray diffraction intensities were measured for a variety of incidence angles, thereby introducing metallographic pole figures to the study of spin compensation. Pole figure data were correlated back to crystal orientation within the liner. X-ray diffraction data were gathered for various locations beneath the liner surface, which were exposed via chemical etching. Finally, data derived on crystal orientation were empirically correlated to the spin compensation frequencies of the liners under consideration.

Metallographic pole figure analysis continues to be used, by Witt, Feng, and Lee,<sup>27-31</sup> to gauge anisotropy in shaped-charge liners. The emphasis in these more recent studies tends to be on determining properties of metal formability, rather than the nature of spin compensation. In fact, since the shear-forming process is today being used to manufacture liners which are not intended to compensate, pole figure analysis is used in conjunction with heat treatment as a means to verify the removal of metallurgical anisotropies from the liner. These recent studies are indicative of a more general trend in the shaped-charge community to emphasize the importance of metallurgy on the performance of jets.<sup>32-35</sup>

One common thread in each previous effort is the semi-empirical nature of the analysis. It is not hard to understand why this is the case, when one considers the multi-disciplinary nature required for the solution of this complex problem. A full treatment of the problem requires three discrete steps:

1. an understanding of the metallurgy within the shear-formed liner (e.g., properties like grain size, dislocation density, crystallographic orientation, etc.);
2. the ability to transform these metallurgical properties of the liner material, determined in step one, into macroscopic continuum anisotropic mechanical properties (e.g., Young's moduli, yield strengths, etc.); and finally,
3. a continuum mechanical analysis of shaped-charge jet formation, employing the anisotropic mechanical properties obtained in step two.

The successful conclusion of step three will result in the determination of the spin compensation properties of the liner at hand. Previous efforts<sup>19,20,27-31</sup> have been aimed at understanding the metallurgy of the liner, in accordance with step one. Step two is not unique to the problem of shaped-charge collapse, but is a field of study in its own right, having been given the name quantitative texture analysis. Though of longstanding concern to scientists, the interpretation of preferred crystal orientation has only recently reached a level of understanding to where quantitative methods have been employable.<sup>36</sup> Modeling of shaped-charge jet formation is an area which has been studied extensively for isotropic liners. To the author's knowledge however, no previous work has been done in modeling the collapse of anisotropic liners. As such, it is step three which is the focus of the current research.

#### 4.1 Determination of Anisotropic Mechanical Properties.

In order to model the spin compensation capacity of an anisotropic liner, the material properties must be available. In the previous section, a three step technique was proposed by which the complete characterization of shear-formed liner compensation could be accomplished. It was also pointed out that the third step, the continuum mechanical modeling of anisotropic liner collapse, was to be the focus of the current research. The first two steps, though beyond the scope of the current research, are discussed within the following section of this report. In particular, the actual techniques for accomplishing material characterization from metallurgical considerations are discussed.

For the current research, material characterization is still important. In the absence of metallurgical tests, however, tensile testing of specimens was performed on rotary forged

copper, whose anisotropic characteristics are believed similar to those of shear-formed copper. These tests and their rationale, will be addressed in Section 4.1.2 of this report.

#### 4.1.1 Metallurgical Determination of Properties.

The determination of mechanical properties from the knowledge of crystallographic orientation is in the domain of quantitative texture analysis. The first phase of the determination requires the acquisition of the metallographic pole figure for the material in question. A pole figure is an empirical measure of crystal plane orientation density expressed in a graphical format by way of a stereographic projection, an example of which is shown in Figure 13.<sup>37</sup> For each type of crystal, (e.g., face centered cubic) there are several principal crystal planes (e.g., 111, 220) whose orientation density may be measured. The orientation density of each crystal plane is characterized by a separate pole figure, the set of which characterize the texture of the specimen.

Pole figure acquisition is an experimental procedure by which x-rays are diffracted from a specimen surface at a variety of incidence angles, with the various reflections being measured. A practical problem which arises in the acquisition of pole figures is one of grazing angles of x-ray incidence. In particular, the already small size of the specimen appears minute at grazing incidence angles, which thus prohibits the acquisition of the reflections at such angles. However, methods have been developed to fill in the gaps of these incomplete pole figures, by making use of the fact that pole points which fall onto the missing range of one pole figure will have a pole in the available range of another pole figure.

With a complete pole figure set in hand, the next step in material characterization involves the determination of the orientation distribution function (ODF) of the material.<sup>36</sup> The ODF specifies the volume fraction of crystals aligned in any arbitrary direction. Because there are a set of orientations which will reflect to the same pole location, the pole figure intensity at a given location represents an integral of the ODF over these orientations. Thus, were one given the ODF initially, determination of the pole figures would be a straightforward task. However, the reverse is not true. As such, various methods (e.g., the harmonic method, the vector method, and the WIMV method, named for its authors Williams, Imhof, Matthies, and Vinel) have been developed for extracting the ODF from the pole figure set.

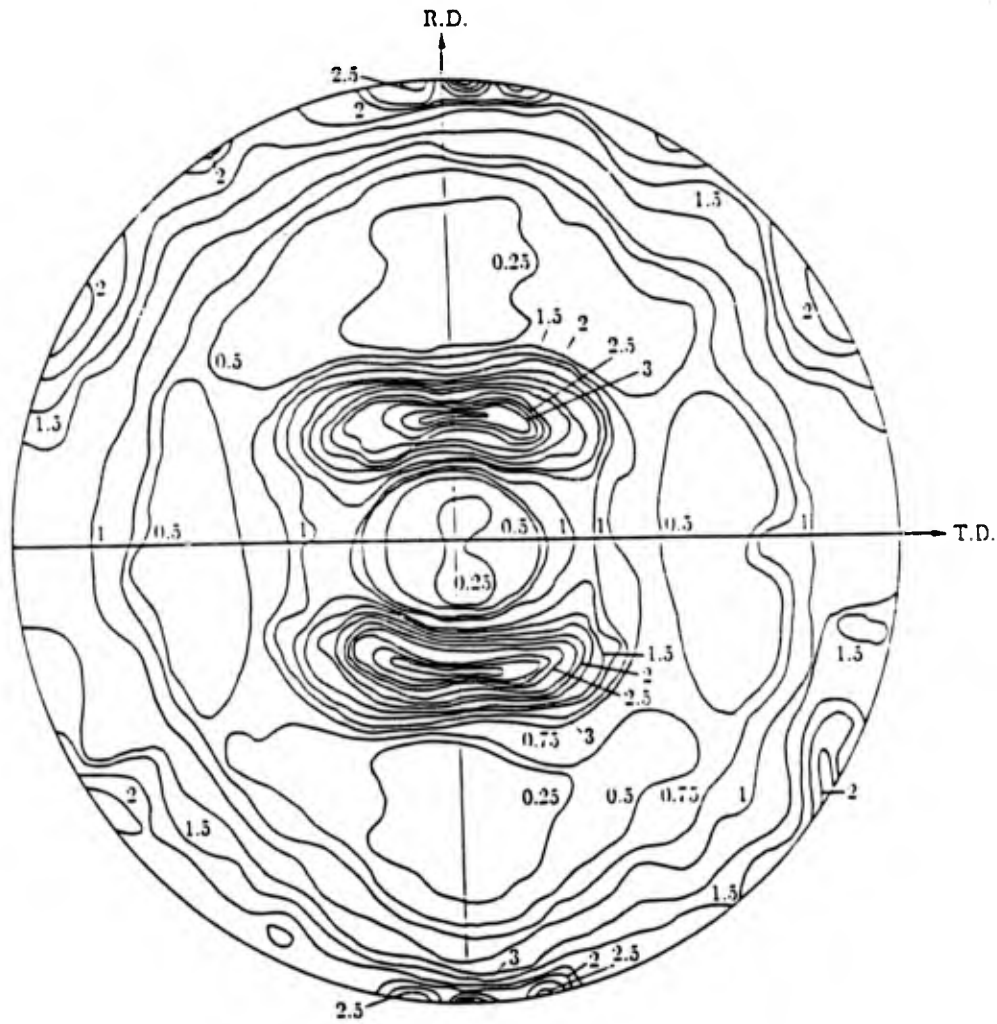


Figure 13. (110) pole figure of recrystallized low-carbon steel.<sup>37</sup>

Once the ODF is determined, the final step is to determine the macroscopic yield parameters. Codes presently exist<sup>38</sup> which convert the ODF into such a set of anisotropic yield parameters compatible with continuum yield conditions like that of Hill.<sup>39</sup> To accomplish this, these codes couple knowledge of the single crystal behavior of a material with the determined ODF.

#### 4.1.2 Experimental determination of properties.

In hopes of acquiring material data on which to base the subsequent liner collapse analysis, tensile tests were performed. Because shear-formed shaped-charge liners are conical in shape and hollow, it is impossible to acquire straight tensile tabs from the liner in the various orientations necessary to characterize the degree of mechanical anisotropy. This being the case, an alternative metalworking process was required which employed a shearing action similar to shear forming and at the same time could produce a flat workpiece from which surrogate tensile tab specimens could be cut. Because of its similarity to the shear-forming process, rotary forging was chosen as the alternative process to study the effects of metalworking on mechanical anisotropy. The tests were merely designed to reveal information on the magnitude of mechanical plastic anisotropy which might be introduced into a copper liner as a result of the shear-forming process. Though elastic anisotropy was considered a viable compensation mechanism early on in the study, it was recognized that the elastic properties of copper were not going to acquire a significant degree of anisotropy from the shear-forming or rotary forging process. As such, and based on the recommendations of Franz,<sup>40</sup> it was decided not to expend resources acquiring elastic data.

Various types of the rotary forging (also known as orbital forging) process are depicted in Figure 14, and have been described in some detail in the literature<sup>41</sup>. The process consists of two forging dies whose axes of symmetry are not quite parallel, but which intersect the axis of the workpiece. Through rotational and/or orbital motion of the dies, the axisymmetric workpiece is forged. The advantage of the rotary forge lies in the fact that only a fraction (typically 20 percent) of the workpiece is in contact with the dies at any instant, so that a fraction of the forging tonnage is required for a given workpiece.

A series of tests were done on specimens cut from rotary forged copper disks in order to characterize the plastic anisotropic mechanical properties of rotary forged copper. Disks

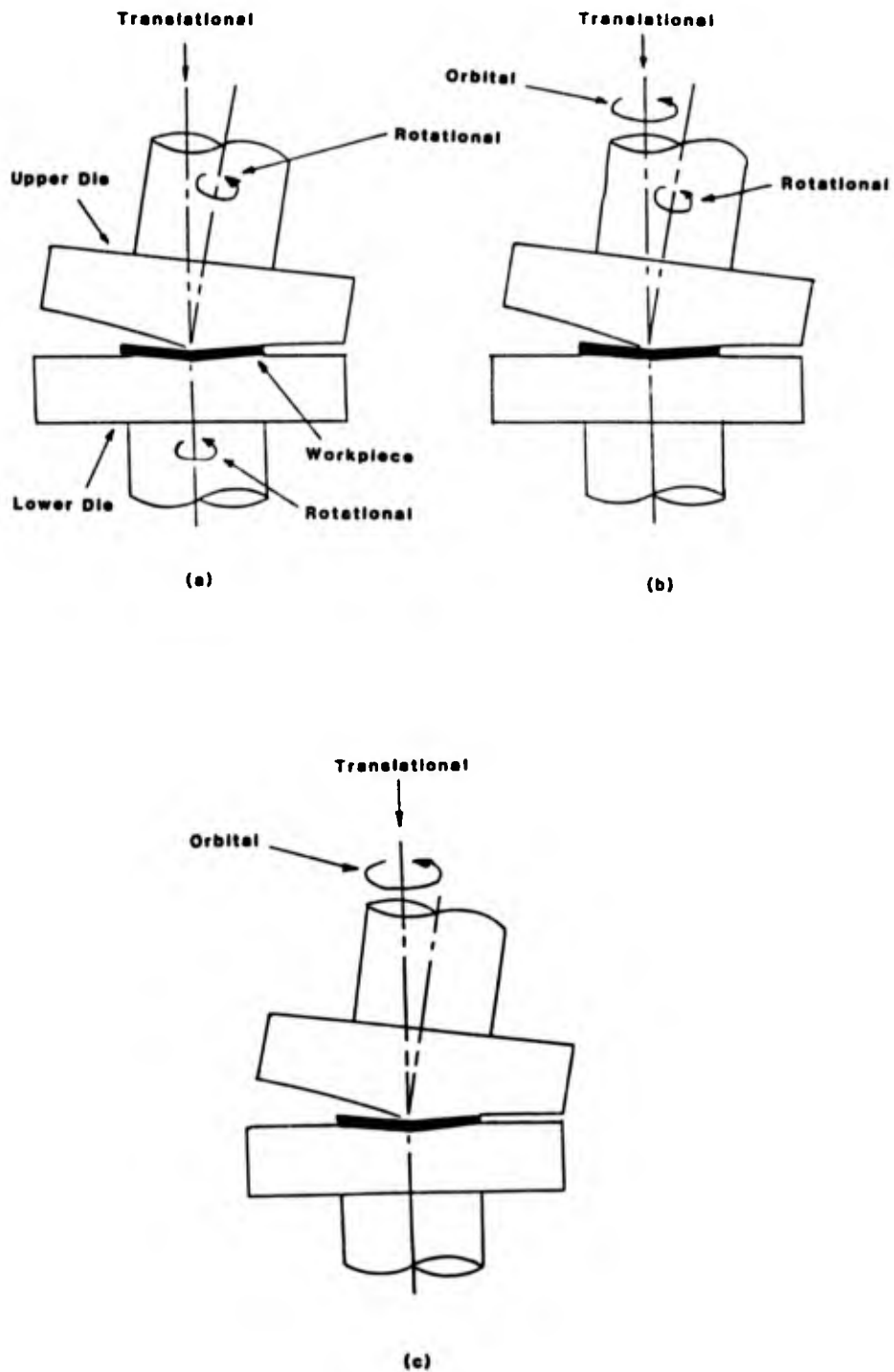


Figure 14. Types of rotary forges: (a) Type 1a is only one die is driven and one follows, Type 1b if both dies are driven; (b) Type 2, and (c) Type 3.

were rotary forged by Dyna East Corporation with various percent reductions in such a way as to give nominally identical final disk thicknesses. Dog-bone tensile tabs were then cut from the disks by Dyna East to produce radial, tangential, and skew specimens as depicted in Figure 15. The specimens were then delivered for mechanical testing.

#### 4.1.3 Tensile test results.

The size of the tensile tabs (1" total) was limited by the size of the rotary forged disks (~3.5" diameter) which, in turn, was limited by the maximum force of the forge (50 tons). Unfortunately, the size of the tabs was such that an extensometer could not be fit to the available gauge length of the tabs (.25"). As such, an accurate measure of dynamic strain is not available from the data. Nonetheless, grip displacement has been used in place of the extensometer to provide a measure of strain, albeit less accurate than an extensometer. The hysteresis of the equipment is such that strain sensitive measurements such as the Young's modulus are grossly inaccurate, though general stress strain behavior may be ascertained from the data. Fortunately, the measurement of maximum engineering tensile stress, which for the cold worked copper in question is roughly equal to the yield strength, is not affected by the use of grip displacement as a basis for strain measurement. Occasional slippage between grip and specimen was noted, but redundant testing provided the means to remove anomalies from the data.

In addition to the several samples which were cut directly from unworked bar stock, specimens were cut from rotary forged workpieces which had undergone 50, 70, 80, and 90 percent reductions. Tensile strength noticeably increased with increasing amounts of workpiece reduction (from 37 ksi [2.55 kbar] for the unworked copper to 56 ksi [3.86 kbar] for copper reduced by 90 percent), as seen in Figure 16. Engineering fracture strain decreased from approximately .42 for unworked material to .25 for all values of reduction tested, the fracture strain seemingly insensitive to the amount of cold work (the strains are based on the original gauge length of the specimen, with localized necking effects being ignored).

Variation of strength with planar specimen orientation only became significant with reductions above 80 percent. For specimens undergoing 90 percent reduction, yield strength in the radial and tangential directions was 95.8 percent of that in the skew direction. These results are in agreement with work of Baldwin,<sup>42</sup> which indicates that the

NOTE: ALL DIMENSIONS IN INCHES.

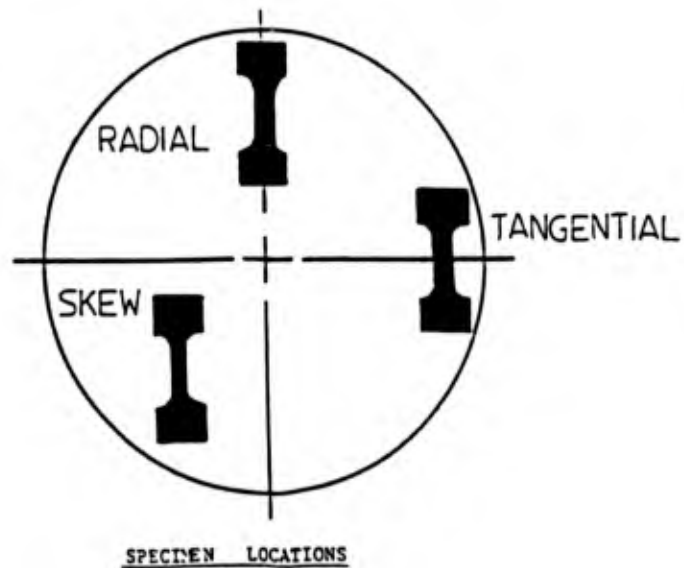
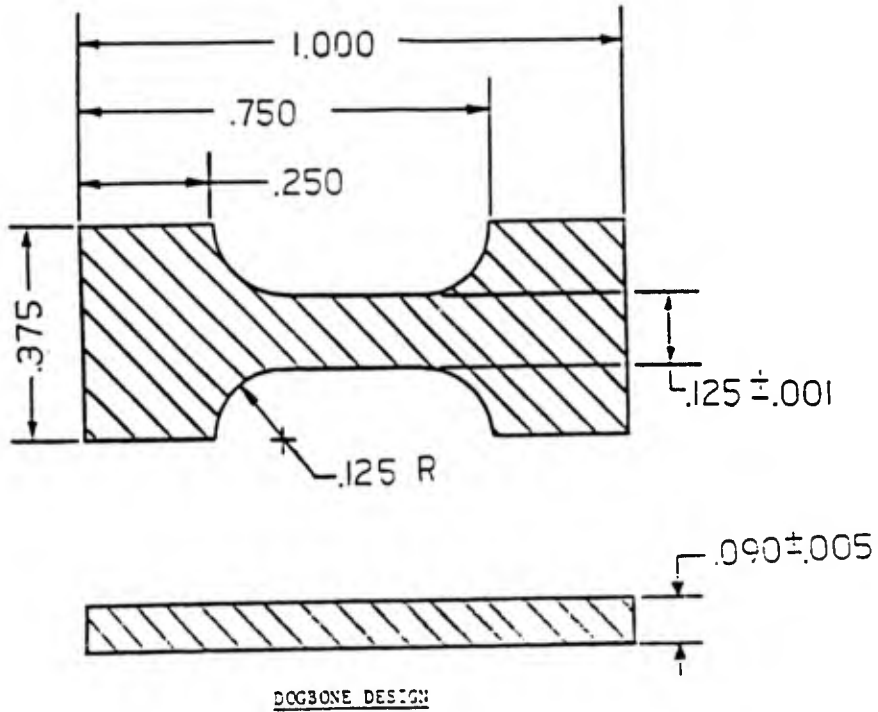


Figure 15. Details of rotary forged dog bone specimens used for tensile testing.

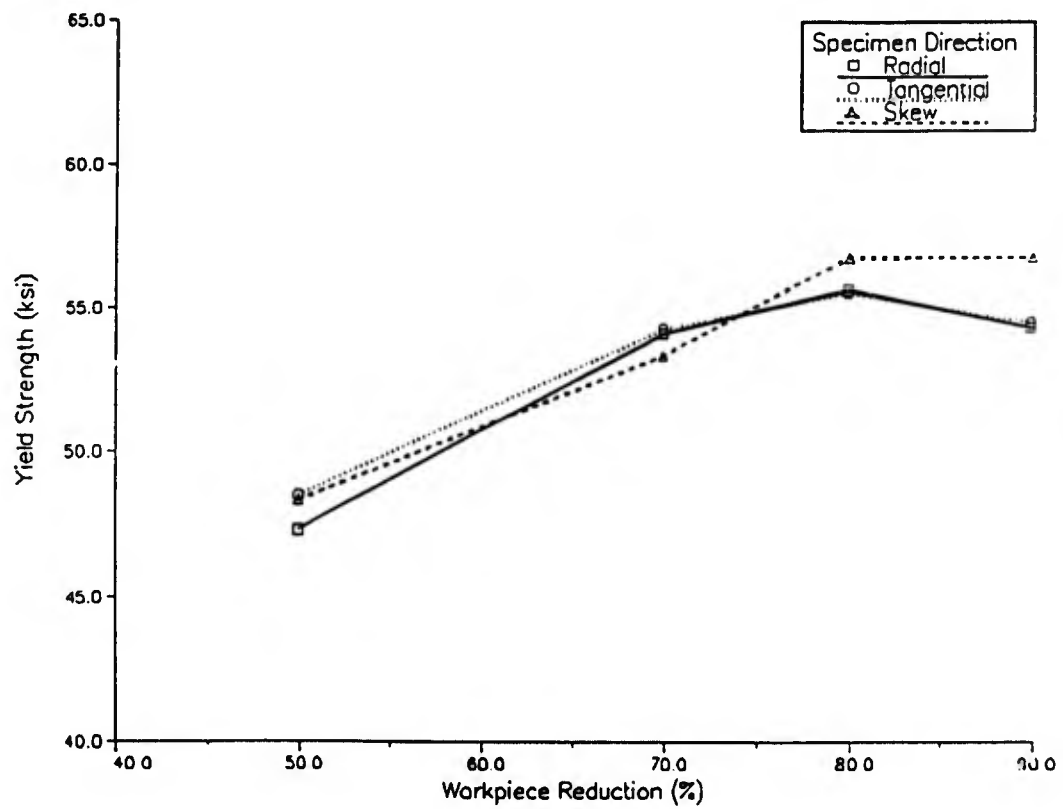


Figure 16. Yield strength versus percent workpiece reduction, for three orientations of tensile specimen.

percentage of grain alignment in copper (grain alignment being responsible for mechanical anisotropy) only becomes significant for reductions in excess of 80 percent. It should be pointed out that Baldwin's measurements were taken after the reduced specimens were annealed, whereas no annealing was performed in the present tests, since shear-formed shaped-charge liners are generally not annealed after forming. Annealing of severely reduced specimens has the unique effect of producing a large percentage of cubically aligned grains in the structure of copper, which produces a characteristic strength versus orientation relation which is shown in Figure 17.<sup>42</sup> In spite of the fact that annealing was not done on the present specimens, a strength dependence was noted with specimen orientation which qualitatively agrees with Baldwin's data.

In particular, tangential and radial strengths were roughly equal, while strengths of specimens in the skew direction (45 degrees with respect to the circumferential "rolling" direction) are greater than strengths in the radial and tangential directions. However, the observed strength in the skew direction is only 4.6 percent greater than radial and tangential strengths (which were roughly equal), while the copper strip data of Figure 17 indicates an 8.5 percent increase in tensile strength. Discrepancies may be attributed to several factors. The data in Figure 17 is for annealed electrolytic copper specimens, in contrast to the oxygen free, high conductivity non-annealed specimens used in the present study. Consider also the fact that only one small region of the gauge section of a skew oriented specimen used in the present study (Figure 15) is oriented at 45 degrees with respect to the tangential. The effect of this second factor is exaggerated because of the relatively large size of the specimen with respect to the workpiece coupled with the fact that change of strength with orientation (indicated by Figure 17) is large in the vicinity of the 45 degree skew direction. Additionally, Baldwin<sup>42</sup> points out that actual strength values reported by various authors do not coincide, though the general shape of the strength-orientation curves follow the same pattern.

In addition to studying the variations in properties that occur in the plane of the rotary forged specimen, it is desired to see whether these planar properties are different from those normal to the plane of the rotary forged workpiece. To do this, width ( $w$ ) and thickness ( $t$ ) measurements were taken at various locations along the gauge length of the broken tensile tabs. A fit was made to the measurements to determine the so called "r-value", which is a constant, defined as

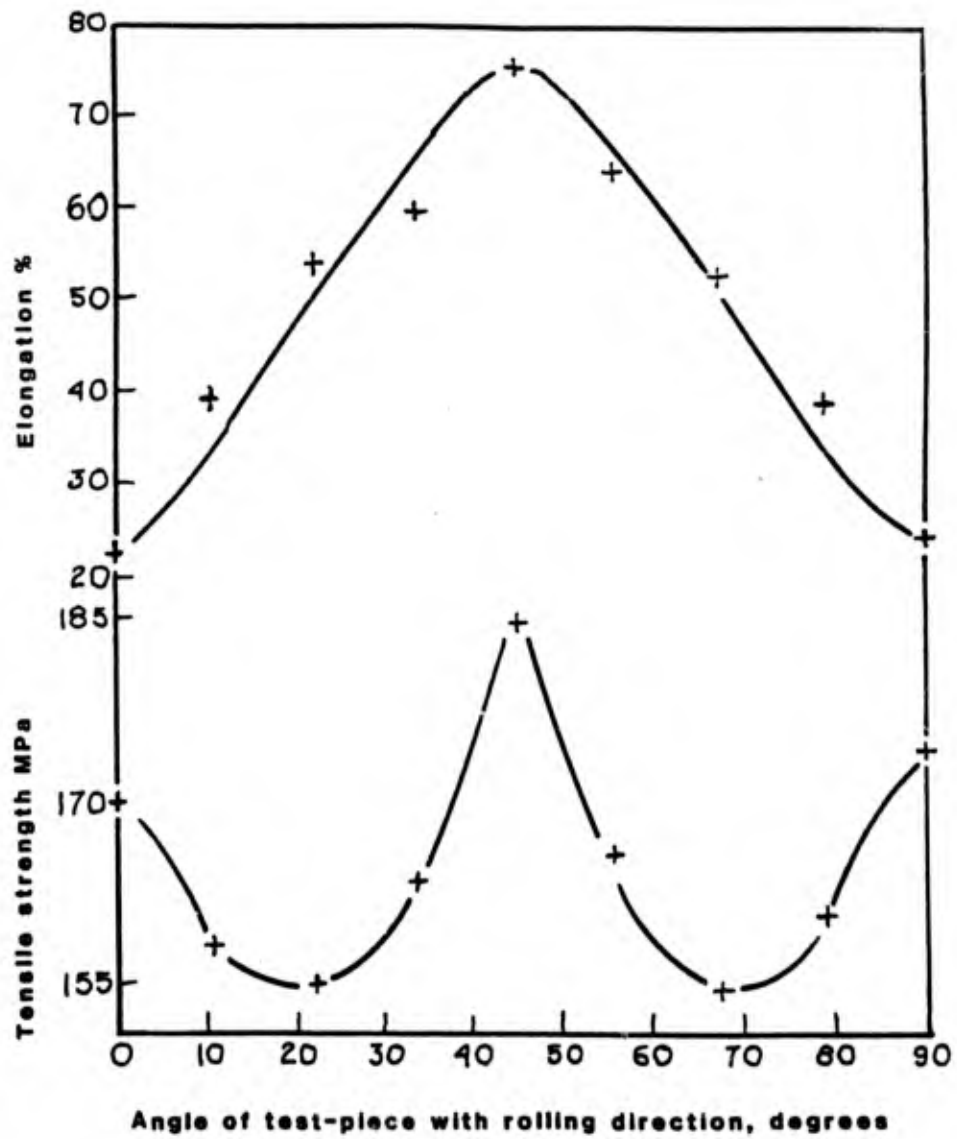


Figure 17. Characteristic strength/elongation versus orientation graph for rolled copper sheet.<sup>42</sup>

$$r = \epsilon_w / \epsilon_t = \ln (w/w_0) / \ln (t/t_0) \quad (4-1)$$

By manipulating equation (4-1) into the form

$$\ln(w) = r \ln(t) + B \quad (4-2)$$

where  $B = \ln(w_0) - r \ln(t_0)$ , the logarithms of the measured thickness and width values were used in a least squares fit to determine values of  $r$  and  $B$ . The initial specimen thickness  $t_0$ , which varied slightly from specimen to specimen, could then be verified through the fit constant  $B$ . A plot showing typical measured data and the fit thickness profile is given in Figure 18.

Present results for copper indicate that it is the thickness strain which consistently exceeds the width strain. The scatter in the data is large, but nonetheless trends may be gathered from the the mean and standard deviations of the  $r$ -values for the three orientations of specimens (see Table 2). In particular, the tangentially oriented specimens have the smallest width to thickness strain ratio, while the radially oriented specimens have the greatest. It is important to note that even though radial and tangential specimens have virtually equal yield strengths, the different  $r$ -values in these two orientations assures that radial and tangential properties are not uniform.

#### 4.1.4 Tensile test analysis.

It is desired to characterize the plastic anisotropic material parameters for the rotary forged copper tested. A successful characterization would be used to model shear-formed liner collapse with the DEFEL finite element code<sup>43</sup> which has been suitably modified for anisotropic use<sup>44</sup> (see Appendix A). Assuming the material to be perfectly plastic, there are six independent parameters which must be determined in order to characterize the plastic behavior of an orthotropic material. Two of the material parameters (normal strengths in the radial and tangential directions) were directly measured during the experiments. The "in plane" shear strength and "through thickness" normal strength may also be inferred from the given tests. Unfortunately, the "through thickness" shear strengths may not be deduced from the tests performed. As such, the tests are merely used to acquire information on the magnitude of anisotropy present as a result of rotary forging.

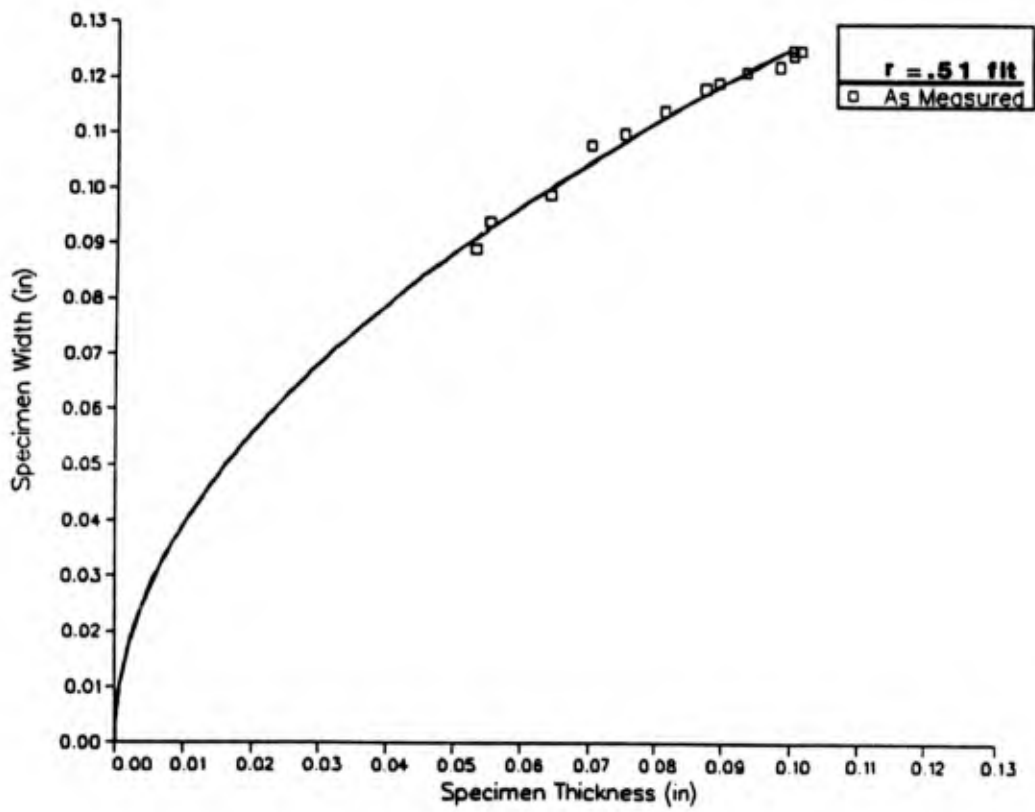


Figure 18. Measured values of specimen width and thickness, along with curve fit, for typical rotary forged tensile tab.

TABLE 2. Width to Thickness Strain Ratio ( $r$ ) and Standard Deviation ( $\sigma$ ) for Various Specimen Orientations after a 90 Percent Reduction via Rotary Forging.

Specimen Orientation	Test #	Width to Thickness Strain Ratio ( $r$ )
Radial:	1	0.62
	2	0.64
	3	0.55
	4	0.71
	Avg. +/- 1 $\sigma$	0.63 +/- .057
Tangential:	1	0.51
	2	0.55
	3	0.52
	4	0.55
	Avg. +/- 1 $\sigma$	0.53 +/- .018
Skew:	1	0.65
	2	0.53
	3	0.64
	4	0.54
	Avg. +/- 1 $\sigma$	0.59 +/- .055

It has been shown that the radial and tangential directions, though exhibiting identical yield strengths, show different  $r$ -values. It can thus be concluded that the laboratory frame does not identically coincide with the preferred material coordinate system. Nonetheless, it is precisely this laboratory frame which will be assumed to be the preferred material frame of reference. Given that there is not enough data to determine the preferred frame of reference, there are several advantages provided by assuming the laboratory frame to coincide with the preferred material frame:

- a. experimentally measured properties are already in the assumed material frame of reference, so no transformations are necessary;
- b. the number of unknown material parameters is reduced; and
- c. the difference between normal yield strengths in an orthogonal frame of reference is greatest for the preferred material frame of reference. Thus, the difference in the measured values of normal yield strengths will be less than or equal to the difference in the actual values in the preferred material frame of reference, thereby providing a conservative estimate as to the magnitude of the actual anisotropy.

The primary drawback of making the assumption on the material coordinate system is that the actual orientation of the preferred material frame remains unknown. This deficiency is addressed in subsequent shaped-charge collapse analyses by means of a parametric study, in which the orientation of the material frame is varied with respect to that of the laboratory frame.

Figure 19 depicts the  $\pi$ -plane of a perfectly plastic anisotropic material in its material coordinate system and under the condition of no shear stress. Recall that the  $\pi$  plane is the geometric plane which is normal to the hydrostatic vector in the Cartesian  $\sigma_1, \sigma_2, \sigma_3$  stress space. The  $\pi$  plane thus represents states of deviatoric stress. The projections of the three stress axes onto the  $\pi$  plane form convergent rays with each axis forming 120 degree angles with the other two stress axes. The isotropic Tresca and von Mises yield criterion project respectively as a hexagon and a circle in the  $\pi$  plane, while the anisotropic yield criterion of Hill projects as an ellipse.

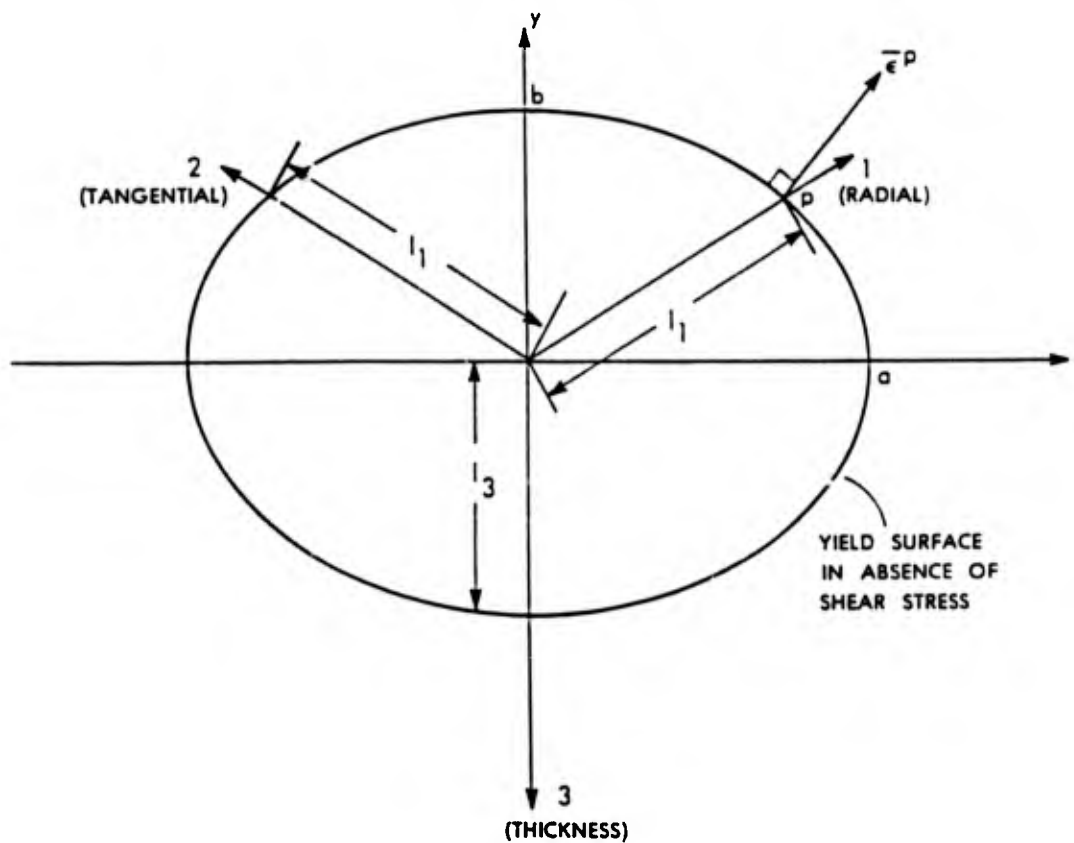


Figure 19.  $\pi$ -plane of a perfectly plastic anisotropic material under conditions of no shear stress. Point P denotes stress state from uniaial stress in one direction.  $\bar{\epsilon}^P$  denotes plastic strain vector after yield.

Unlike the isotropic yield surface in which the yield strength is independent of coordinate rotation, the yield strengths of an anisotropic material may in fact, vary with coordinate direction. It is desired though, to retain the coordinate reference of the material's preferred orientation. As a result, the introduction of shear stress, in accordance with Hill's yield criterion, will make the yield ellipse shrink in size, though it will retain the same shape and orientation. In accordance with the observed behavior of the rotary forged copper, the yield strengths in directions 1 and 2 have been made identical. The parameter to be determined next will be yield strength in the thickness direction (i.e., material direction 3).

For a specimen in simple tension along the radial material axis (direction 1), the  $\pi$ -plane stress behavior will follow axis 1, until such time that yield is reached at point P as shown in Figure 19. At this time, the stress state will remain at point P on the yield ellipse, so as to enforce the stress free conditions along material axes 2 and 3 (if material directions 2 and 3 are stress free, then deviatoric stresses in directions 2 and 3 are equal; this can only be satisfied by having the deviatoric stress state aligned with the 1 axis).

However, the plastic flow rule dictates that the increment of plastic strain be normal to the yield surface. The plastic strain increment  $\bar{\epsilon}P$  is displayed in Figure 19 normal to the yield surface at point P. Projecting the plastic strain vector along the 2 and 3 material axes, it can be seen that the 2 and 3 components of plastic strain are not identical. It is desired to determine the value of normal yield strength in material direction 3 (the thickness direction) so that the ratio of thickness plastic strain to the plastic strain in the tangential direction matches the empirically determined value for rotary forged copper. The assumption that the radial, tangential, and thickness directions coincide exactly with the material directions coupled with the observation that yield strengths in directions 1 and 2 are equal implies that r-values for both radial and tangential specimens should be equal. Observations in Table 2 show the values to be close but not equal (.63 versus .53). Since the assumptions employed on the frame of reference orientation would have them equal, an average value of .58 is used in the determination of yield strength for material direction number 3.

Consider the  $\pi$ -plane of the anisotropic copper depicted in Figure 19. By introducing a Cartesian x-y frame to coincide with the major axes of the yield ellipse, the calculation will be greatly simplified. If the strengths along directions 1 and 2 are equal, then the minor

axis of the yield ellipse will coincide with the 3 direction. For the ellipse shown with major and minor axes lengths of  $2a$  and  $2b$  respectively, the equation governing the yield surface in the  $x$ - $y$  coordinate system is

$$\frac{x^2}{a^2} + \frac{y^2}{b^2} = 1 \quad (4-3)$$

The outward normal to the yield surface at any point  $(x,y)$  on the yield surface is given by

$$\hat{n} = \frac{b^2x \hat{i} + a^2y \hat{j}}{(b^4x^2 + a^4y^2)^{1/2}} \quad (4-4)$$

For the point P which lies on the yield surface along the 1 axis, the ratio  $x:y$  is  $\sqrt{3}:1$ , and the outward normal is

$$\hat{n} = \frac{(\sqrt{3})b^2 \hat{i} + a^2 \hat{j}}{(3b^4 + a^4)^{1/2}} \quad (4-5)$$

and thus the plastic strain is given by

$$\bar{\epsilon}^P = \frac{(\sqrt{3})b^2 \hat{i} + a^2 \hat{j}}{(3b^4 + a^4)^{1/2}} |\bar{\epsilon}^P| \quad (4-6)$$

To determine the 2 and 3 components of plastic strain (i.e., the width and thickness strains in the radially oriented specimen), one merely takes the dot product of the plastic strain with the unit direction vectors for directions 2 and 3. This gives the following results:

$$\epsilon_2^P = \frac{-3b^2 + a^2}{2(3b^4 + a^4)^{1/2}} |\bar{\epsilon}^P| \quad (4-7)$$

$$\epsilon_3^P = \frac{-a^2}{(3b^4 + a^4)^{1/2}} |\bar{\epsilon}^P| \quad (4-8)$$

The ratio of width to thickness strain ( $\epsilon_2^P/\epsilon_3^P$ ) was previously given the symbol  $r$ , and from equations (4-7) and (4-8), its value can be shown to be

$$r = \frac{-3b^2 + a^2}{-2a^2} \quad (4-9)$$

In a similar fashion, the major to minor axis ratio may be expressed as

$$\frac{a}{b} = \left( \frac{3}{2r + 1} \right)^{1/2} \quad (4-10)$$

Finally, after one determines that the ratio  $l_1/a$  from the geometry of the yield ellipse to be  $2b/(3b^2+a^2)^{1/2}$  and that  $b/l_3$  is unity, one may deduce the desired yield strength ratio:

$$\frac{Y_1}{Y_3} = \frac{l_1}{l_3} = \frac{l_1}{a} \frac{a}{b} \frac{b}{l_3} = \left( \frac{2}{1+r} \right)^{1/2} \quad (4-11)$$

For the experimentally determined  $r$ -value of 0.58, a ratio ( $Y_1/Y_3$ ) of 1.13 is determined. It is interesting to note that the experimentally observed variation in  $r$ -values (ranging from 0.53 to 0.63) corresponds to a variation in the yield strength ratio ( $Y_1/Y_3$ ) of only 1.110 to 1.145. This small variation in yield strength ratio seems within the bounds of experimental variability, so that it is not clear whether significance should be applied to the observed variation in plastic strain ratio.

It has just been demonstrated that normal strengths in the material coordinates may be determined, if one knows the thickness to width plastic strain ratios in the material coordinates. It is now necessary to determine the material parameters which characterize the shear strength of the material. Unfortunately, not all of the three remaining parameters may be determined from the data obtained in the simple tension tests that were performed. However, the shear strength parameter for the radial-tangential plane can be evaluated.

The term may be evaluated using the tensile data from the skew oriented tensile specimens. By transforming the skew coordinate frame test data into the assumed material coordinates (the radial-tangential frame), the simple tension test becomes one in which the

radial and tangential normal stresses ( $\sigma_1, \sigma_2$ ) as well as the radial-tangential shear stress ( $\sigma_{12}$ ) are all equal to half of the applied tensile stress value of the skew frame ( $Y_{skew}$ ). Inserting these stress values into Hill's yield function

$$1 = F(\sigma_y - \sigma_z)^2 + G(\sigma_z - \sigma_x)^2 + H(\sigma_x - \sigma_y)^2 + 2L\tau_{yz}^2 + 2M\tau_{zx}^2 + 2N\tau_{xy}^2 \quad (4-12)$$

gives the result:

$$(H+G)Y_1^2 = \frac{(F+G)}{4} Y_{skew}^2 + \frac{N}{2} Y_{skew}^2 \quad (4-13)$$

Knowing by definition that  $(F+G) = 1/Y_3^2$ ,  $(H+G) = 1/Y_1^2$  and  $N = 1/2Y_{12}^2$ , the equation may be solved for  $Y_1/Y_{12}$  in terms of known ratios. The result is:

$$\left( \frac{Y_1}{Y_{12}} \right)^2 = 4 \left( \frac{Y_1}{Y_{skew}} \right)^2 - \left( \frac{Y_1}{Y_3} \right)^2 \quad (4-14)$$

Using the (previously discussed) experimentally observed values for  $(Y_1/Y_{skew})$  of .958 (see Figure 16) and  $(Y_1/Y_3)$  of 1.13, the parameter ratio  $(Y_1/Y_{12})$  is determined to be 1.55. For isotropic materials obeying the von Mises yield criterion, this ratio would be 1.73.

#### 4.1.5 Tensile test conclusions.

Rotary forging exhibits many similarities to rolling. Test results support this assertion, which indicate that for specimens reduced 90 percent in thickness via rotary forging, significant mechanical anisotropy is observed. The anisotropy is similar in character and order of magnitude to that observed in rolling, if one takes the rotary forged tangential direction as the direction of rolling.

The data which have been gathered from the tests performed may now be made available for use in computer simulations involving anisotropic copper. A similarity between

the rotary forging and shear-forming processes exists to the extent that both processes undergo a shearing mode of deformation. However, the type and degree of deformation in the two processes is significantly different. Also, the strain rates at which the tensile tests were performed differs vastly from the actual conditions of explosively loaded liner collapse. Nonetheless, it is hoped that the use of anisotropy of the magnitudes experimentally observed, in the computational simulation of shear-formed liner collapse, will yield relevant results.

#### 4.2 Analytical Studies.

In a fashion similar to that used in the residual stress analysis, it is useful to develop closed form analytical models to examine the behavior of collapsing anisotropic liner elements. The results of such a study would indicate the magnitude of anisotropic shear coupling necessary to produce jet rotation of a magnitude large enough to produce spin compensation (shear coupling is the phenomenon which exists in anisotropic materials which makes it possible to produce shear strains from the application of normal stress). After such necessary shear coupling ratios have been determined, the laws of elasticity and plasticity may be exercised to see if, in fact, such coupling ratios are obtainable from the deformation of anisotropic materials of given anisotropy characteristics.

##### 4.2.1 Elastic vs. plastic anisotropy.

At the onset of this study, both elastic and plastic anisotropy were being considered as viable mechanisms to produce compensation. However, it was eventually concluded that of the two, plastic anisotropy was a more likely cause of jet rotation, and the formulation of elastic models of spin compensation was thus suspended. There were two reasons for arriving at the conclusion regarding elastic anisotropy.

First of all, the elastic properties of copper are not going to acquire a significant degree of anisotropy from the shear-forming or rotary forging process.<sup>40</sup> Of more importance however, is the fact that for problems of proportional loading (by which the early stages of liner collapse may be approximated), elastic properties become insignificant soon after yield is reached, and the stress behavior of the material becomes totally governed by the plastic flow rule. To understand the significance of this, consider the  $\pi$ -planes of a material with an isotropic yield surface, as shown in Figure 20. If the elastic behavior of the material is

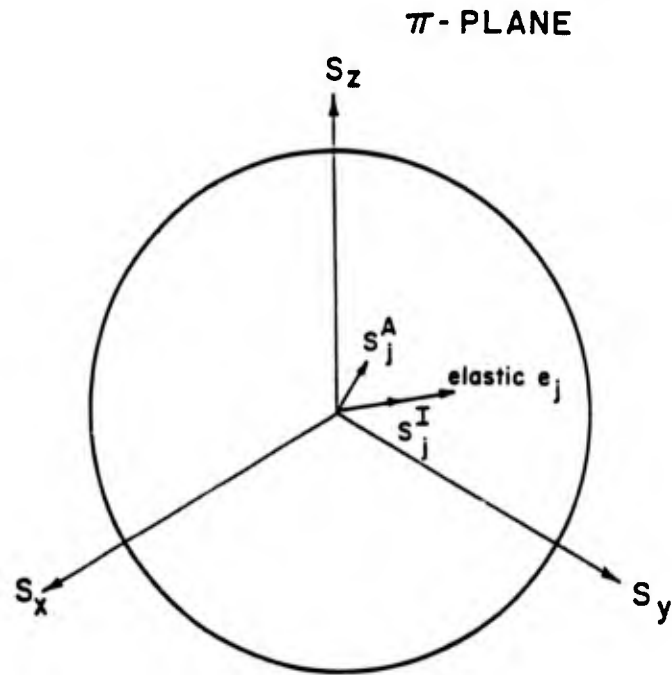


Figure 20.  $\pi$ -plane of a material, strained to  $e_j$ , prior to yield. Anisotropic stress state  $s_j^A$  differs from the isotropic stress state  $s_j^I$ .

isotropic, the deviator stress state ( $s_j^I$ ) follows the direction of strain ( $e_j$ ). The elastic stress state of an anisotropic material will not follow the strain direction, but instead a different direction (schematically shown as  $s_j^A$  in Figure 20).

Under steady state conditions of proportional strain loading (which describes the early stages of liner collapse very well), the stress quickly reaches a state on the yield surface where the yield surface normal is proportional to the strain loading vector. This process is depicted in Figure 21. The steady state stress condition is independent of the elastic properties of the material, even if the yield surface is anisotropic. Thus, even if a large amount of elastic anisotropy were present in the material, its effect on liner collapse would be essentially limited to a very short duration (fractions of a microsecond) following the onset of plastic deformation.

#### 4.2.2 Collapsing anisotropic liner element.

In order to achieve spin compensation, the circumferential velocity imparted to a collapsing liner element from anisotropy ( $V_o$ ) must be able to exactly counter the velocity due to compensating spin ( $\Omega R$ ). For this analysis, the concept of shear velocity is introduced. Consider a disk extracted from the original liner by slicing perpendicular to the axis of symmetry. The reference frame for the analysis is acquired by taking an  $r \, d\theta$  wedge shaped section of the disk, as shown in Figure 22, using a primed 1-2-3 Cartesian system.

Shear velocity in the current context is the circumferential velocity imparted to the liner as a direct result of coupled shear strain. Figure 23 depicts such a shear velocity distribution of a collapsing liner element, as viewed in the  $r-\theta$  plane. Though the forces on the element result from either normal stress components or radial inertia ( $-a \, \delta m$ ), the shear strain responsible for the shear velocity arises from the anisotropic nature of the material. Because the jet is formed from the inner surface of the collapsing liner, the shear velocity concept results in jet/slug counter-rotation.

A direct result of the flow rule associated with anisotropic materials following Hill's yield criterion is that the strain increment tensor over an infinitesimal period of time is proportional to the stress state of the material. This result is also valid for isotropic materials obeying von Mises yield condition/Prandtl Reuss flow rule. Where anisotropic

$\pi$  - PLANE

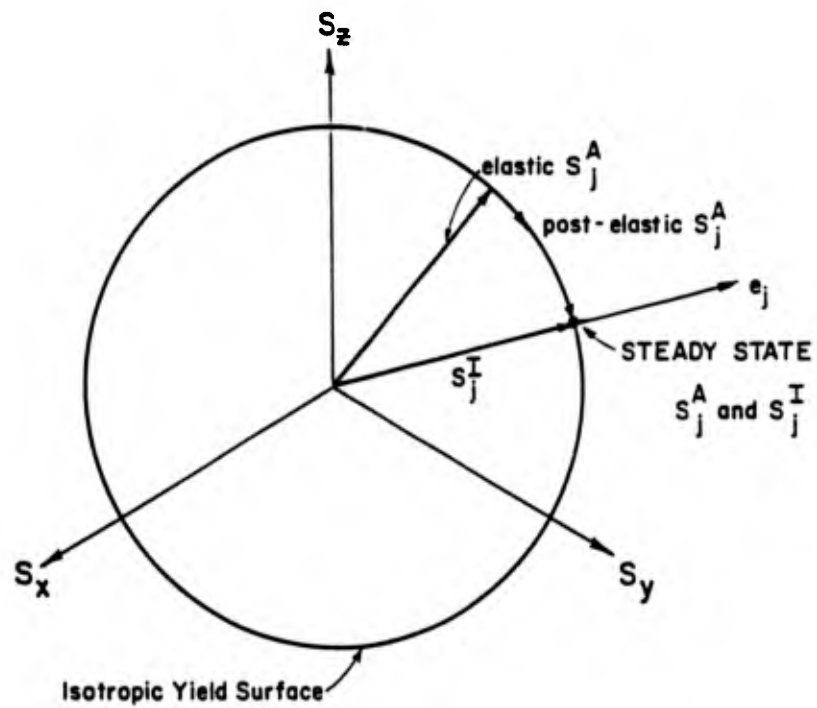


Figure 21.  $\pi$ -plane of a material, strained to  $e_j$ , following yield. Anisotropic stress state  $s_j^A$  rapidly approaches the isotropic stress state  $s_j^I$ .

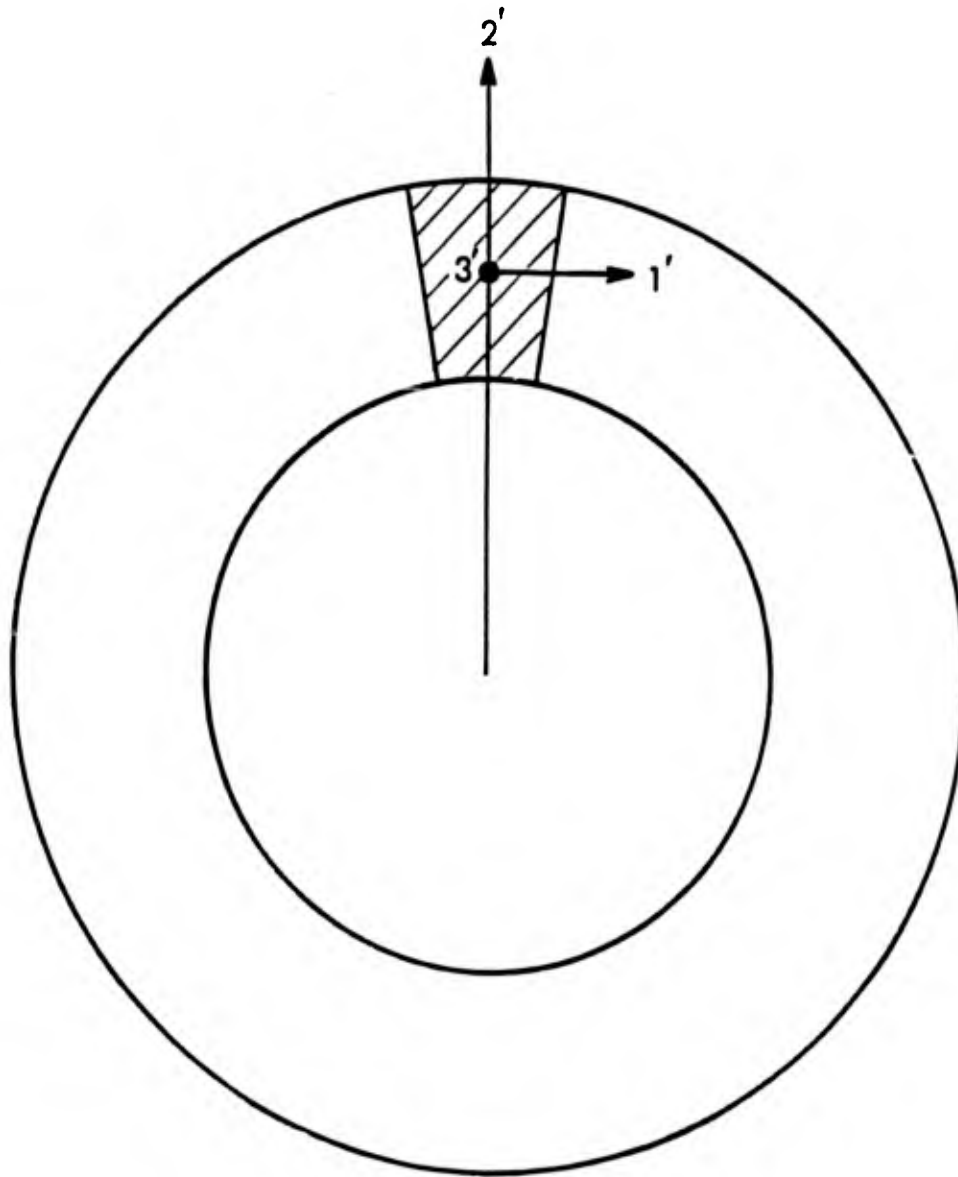


Figure 22. Primed 1-2-3 laboratory coordinate system used for shear velocity analysis.

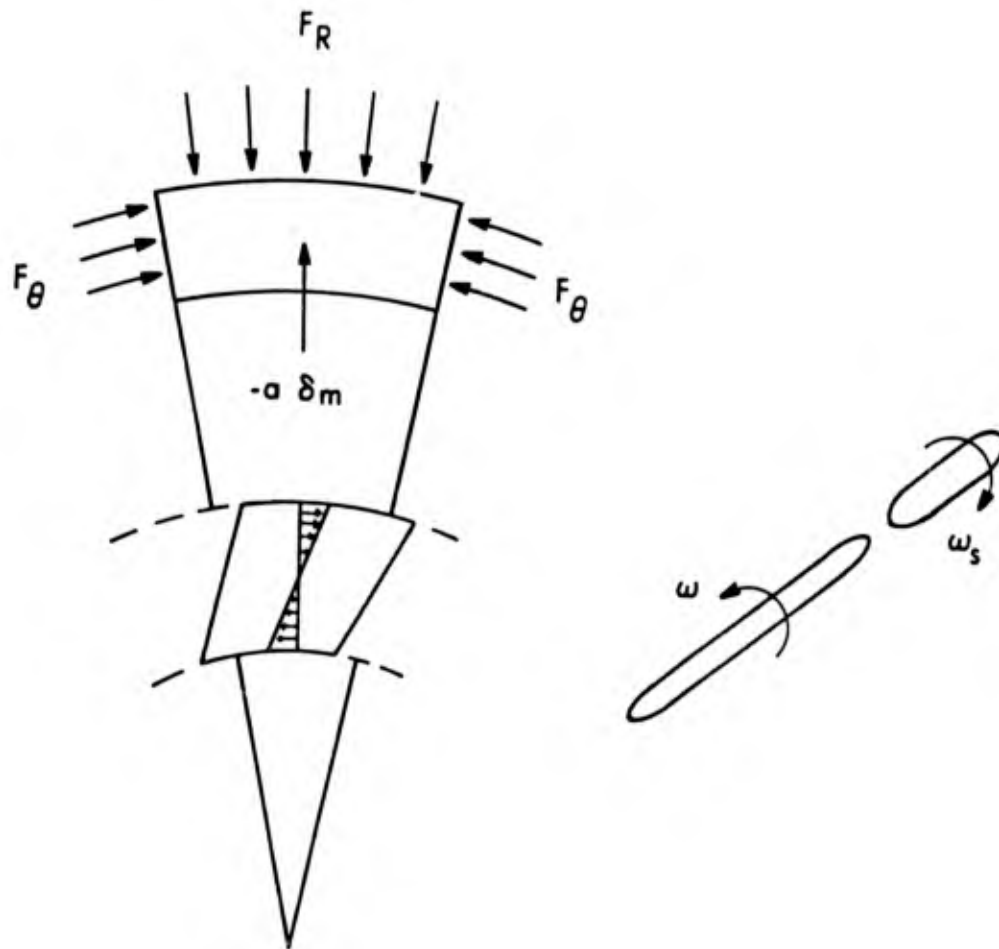


Figure 23. Schematic illustration of shear velocity concept, with resultant counter-rotation of jet and slug.

materials differ from isotropic ones is that the shear strain increments for anisotropic materials may, in fact, be proportional to the normal stress state. This coupling of normal stress to shear strain is known as shear coupling. If the yield condition does not evolve under material deformation, and if the loading history is proportional, then the ratio of any two strain components (and thus their rates) will be constant throughout the duration of proportional plastic deformation.

Because of shear velocity, the circumferential velocity of the inner skin of the liner element ( $V_o$ ) is given by

$$V_o = \frac{\dot{\gamma}_{12}'\delta}{2} = \dot{\epsilon}_{12}'\delta \quad , \quad (4-15)$$

where  $\delta$  is the liner thickness,  $\gamma_{12}'$  and  $\epsilon_{12}'$  are respectively the engineering and tensorial shear strains, in the laboratory frame of reference. Because the early stages of liner collapse may be approximated by the conditions of proportional loading, the shear velocity ( $V_o$ ) may be related to hoop strain rate ( $d\epsilon_1'/dt$ ) by way of the shear/normal coupling ratio ( $\epsilon_{12}'/\epsilon_1'$ ) as follows:

$$V_o = \left( \frac{\epsilon_{12}'}{\epsilon_1'} \right) \dot{\epsilon}_1'\delta \quad , \quad (4-16)$$

The hoop strain rate, governed by the collapse of the liner, is independent of the anisotropy, and is expressible in terms of the radial coordinate ( $r$ ) and its time derivative. The initial value of hoop strain rate, at the onset of collapse (when  $r=R$ ), is given as

$$\dot{\epsilon}_1' = \frac{(dR/dt)}{R} \quad , \quad (4-17)$$

Equations (4-16) and (4-17) may be used when setting the shear velocity ( $V_o$ ) equal to the compensation velocity ( $\Omega R$ ), and an expression for the coupling ratio necessary to produce compensation results, and is given by

$$\frac{\epsilon_{12}'}{\epsilon_1'} = \frac{\Omega R^2}{\delta (dR/dt)} \quad , \quad (4-18)$$

The values of radial collapse velocity  $dR/dt$  vary for each element throughout the liner, and were acquired from Baker's MJCON code<sup>45</sup> for a collapsing BRL 81 mm liner. Thus, the necessary values to compute the shear coupling vary from liner apex to base as:

	Liner Apex	to	Liner Base
$\delta$	= 2 mm	to	2 mm,
R	= 17.8 mm	to	32.4 mm, and
$dR/dt$	= 2,156 m/s	to	1,528 m/s.

In Section 1.3, it was shown, based upon existing shear formed liner data, that the expected value of scaled compensation frequency ( $\Omega D$ ) was 2,850 mm rps. For the 81 mm charge currently under consideration, this equates to an expected compensation frequency of 35 rps (220 rad/sec). For such a spin rate, then the necessary coupling ratio ( $\epsilon_{12}'/\epsilon_1'$ ) varies from .016 near the liner apex to .076 near the base of the liner. When mass averaged over the liner, the necessary coupling ratio of approximately .05 is computed. Thus, if the shear to hoop strain ratio coupling is found to take on values exceeding .05 under loading conditions of liner collapse, then compensation by way of plastic anisotropy is indeed feasible.

#### 4.2.3 Shear coupling.

In the previous section, it was shown that shear coupling of 1'-2' shear strain to normal strain in direction 1' (hoop strain) may introduce shear velocity in a collapsing liner to the extent where spin compensation is feasible. That feasibility hinged upon the coupling ratio being of magnitude .05 or greater. It is therefore of interest to examine the coupling ratio analytically to see how its behavior is influenced by the various material parameters. The material parameters in question include both the magnitudes of anisotropy in the preferred reference frame of the material, and the orientation of that frame with respect to the laboratory coordinate system. Because plastic strain increments are proportional to the plastic potential gradient (the partial derivative of the yield potential function with respect to each component of the stress state), analysis of the coupling ratio necessarily requires derivation of the plastic potential gradient.

As such, equations are derived for the plastic potential gradient of an orthotropic material in a non-preferred reference frame, but restrict the difference between laboratory and preferred material frames to a single rotation about one of the laboratory axes. Because the previous analysis depends on shear coupling in the 1'-2' plane, it will be assumed that the preferred set of material axes (denoted in this section as the 1-2-3 coordinate system) will be formed by a rotation of the laboratory coordinate system counter-clockwise by an angle  $\Gamma$  about the 3' axis. The resulting plastic flow rule exhibits several interesting properties: it is conveniently expressed as the sum of the material's preferred frame plastic potential gradient and deviation terms. Also, the deviation terms combine in a recurring fashion so that, even with seven input quantities (six material parameters and an orientation), there appear only four independent terms which comprise the deviation plastic potential gradient.

If the plastic potential is a scalar function of stress, then the components of the plastic strain increment are proportional to the gradient of the potential (i.e., the yield surface normal):

$$d\epsilon_i^P = d\lambda \frac{\partial f}{\partial \sigma_i} \quad (4-19)$$

where:

$f$  is the plastic potential function, which defines the yield surface in terms of the stress state  $\sigma_i$ ,

$d\lambda$  is the non-negative proportionality constant, and

$d\epsilon_i^P$  is the (plastic) strain increment, with tensorial shear strain components (i.e.,  $\epsilon_{12} = 1/2 \gamma_{12}$ ).

In the material's preferred reference frame, the gradient of the plastic potential is expressed for an anisotropic material, using the notations of Hill by taking the partial derivative of the yield function (4-12) with respect to each of the stress components.

$$\frac{\partial f}{\partial \sigma_i} = A_{ij} \sigma_j = \begin{pmatrix} (H+G) & -H & -G & 0 & 0 & 0 \\ -H & (F+H) & -F & 0 & 0 & 0 \\ -G & -F & (F+G) & 0 & 0 & 0 \\ 0 & 0 & 0 & L & 0 & 0 \\ 0 & 0 & 0 & 0 & M & 0 \\ 0 & 0 & 0 & 0 & 0 & N \end{pmatrix} \begin{pmatrix} \sigma_1 \\ \sigma_2 \\ \sigma_3 \\ \sigma_4 \\ \sigma_5 \\ \sigma_6 \end{pmatrix} \quad (4-20)$$

Because the yield function (4-12) is expressed in terms of a convenient (albeit non-tensorial) six dimensional contracted "stress vector" space, it must be realized that terms like  $\sigma_{12}$  in reality represent the sum of two equal valued shear stresses (the 12 and 21 stresses). As such, the partial derivatives with respect to shear stresses are one half of that computed strictly on the basis of equation (4-12). Using relations (4-19) and (4-20), one can conclude

$$d\epsilon_i^p = d\lambda A_{ij} \sigma_j \quad (4-21)$$

If one wishes to express this form of the flow rule in terms of a laboratory reference (denoted with the use of primes), one must make use of transformation relations for converting stress and strain from one reference frame to another:

$$\begin{aligned} \sigma_i &= T_{ij} \sigma'_j \\ \epsilon_i &= T_{ij} \epsilon'_j \end{aligned} \quad (4-22)$$

in order to acquire

$$d\epsilon_i^{p'} = d\lambda (T_{ik}^{-1} A_{kl} T_{lj}) \sigma'_j \quad (4-23)$$

Therefore, the laboratory frame version of the plastic potential gradient ( $A_{ij}'$ ) matrix is  $(T_{ik}^{-1} A_{kl} T_{lj})$ .

It is convenient to express the laboratory frame plastic potential gradient ( $T^{-1}AT\sigma'$ ) as the sum of the preferred frame plastic potential gradient ( $A\sigma'$ ) and a deviation term ( $\tilde{A}\sigma'$ ):

$$A_{ij}' = T_{ik}^{-1} A_{kl} T_{lj} = (A_{ij} + \tilde{A}_{ij}) \quad (4-24)$$

so that the flow rule becomes:

$$d\epsilon_i^{P'} = d\lambda (A'_{ij} + \tilde{A}_{ij}) \sigma_j' \quad , \quad (4-25)$$

Under the proposed transformation to the material's preferred coordinate system (rotation by an angle  $\Gamma$  about the 3' axis), the transformation matrix is readily expressed as

$$T_{ij} = \begin{pmatrix} m^2 & n^2 & 0 & 0 & 0 & 2mn \\ n^2 & m^2 & 0 & 0 & 0 & -2mn \\ 0 & 0 & 1 & 0 & 0 & 0 \\ 0 & 0 & 0 & m & -n & 0 \\ 0 & 0 & 0 & n & m & 0 \\ -mn & mn & 0 & 0 & 0 & (m^2-n^2) \end{pmatrix} \quad , \quad (4-26)$$

where  $m$  and  $n$  are  $\cos \Gamma$  and  $\sin \Gamma$ , respectively.

The matrix expansion depicted by equation (4-24) is straight forward, but lengthy. It was performed to determine the deviation matrix  $\tilde{A}_{ij}$ , which is shown in Table 3. Notice that even though  $\tilde{A}_{ij}$  is composed of the six material constants and one orientation parameter, the terms combine in a way such that only four parameters are needed ( $Q_1, Q_2, Q_3$  and  $\Gamma$ ).

Under the hypothetical loading conditions of  $\sigma'_i = \langle \sigma \ 0 \ 0 \ 0 \ 0 \ 0 \rangle$ , equation (4-25) may be applied to determine the ratio of 1'2' (i.e.,  $r\theta$ ) shear strain to 1' (i.e.,  $\theta$ ) normal strain. The relationship is

$$\frac{\epsilon_{12}'}{\epsilon_1'} = \frac{mn[Q_2 n^2 - Q_1 m^2]}{(G+H) + n^2[2Q_1 m^2 + (Q_1 - Q_2)n^2]} \quad . \quad (4-27)$$

To see how this relationship varies with preferred material frame orientation, one must insert values for the anisotropy magnitudes. The material constants acquired from the rotary forged tensile test, in the assumed preferred material frame of reference, were

$$Y_i = \langle 3.86 \ 3.86 \ 3.41 \ 2.49 \ ?? \ ?? \rangle \text{ kbar.}$$

TABLE 3. Plastic Potential Deviation Matrix  $\tilde{A}_{ij}$

$$\tilde{A}_{ij} = \begin{pmatrix} n^2[2Q_1m^2 + (Q_1 - Q_2)n^2] & -(Q_1 + Q_2)m^2n^2 & n^2(Q_2 - Q_1) & 0 & 0 & 2mn(Q_2n^2 - Q_1m^2) \\ -(Q_1 + Q_2)m^2n^2 & n^2[2Q_2m^2 + (Q_2 - Q_1)n^2] & n^2(Q_1 - Q_2) & 0 & 0 & 2mn(Q_2m^2 - Q_1n^2) \\ n^2(Q_2 - Q_1) & n^2(Q_1 - Q_2) & 0 & 0 & 0 & 2mn(Q_1 - Q_2) \\ 0 & 0 & 0 & n^2Q_3 & mnQ_3 & 0 \\ 0 & 0 & 0 & mnQ_3 & -n^2Q_3 & 0 \\ mn(Q_2n^2 - Q_1m^2) & mn(Q_2m^2 - Q_1n^2) & mn(Q_1 - Q_2) & 0 & 0 & -m^2n^2(Q_1 + Q_2) \end{pmatrix}$$

where:  
 $Q_1 = N - 2H - G$   
 $Q_2 = N - 2H - F$   
 $Q_3 = M - L$   
 $m = \cos \Gamma$   
 $n = \sin \Gamma$

For this analysis, a transversely isotropic material will be adopted for the sake of simplicity, with isotropy being preserved in the 2-3 plane. The normal strength components from the tensile tests will be used with axis permutation to give:

$$Y_i = \langle 3.41 \ 3.86 \ 3.86 \ \ ? \ ? \ ? \rangle \text{ kbar.}$$

Because 2-3 transverse isotropy is assumed, the strength  $Y_4$  is determinable on the basis of symmetry. Hill<sup>39</sup> expressed the transversely isotropic constraint in his yield function (4-12) as  $L = 2F + G$  which, when employed with the values at hand, gives  $Y_4 = 2.34$  kbar. The remaining constants,  $Y_5$  and  $Y_6$ , must be equal under transversely isotropic considerations. For lack of other data, their value was chosen to preserve the following ratio:  $Y_1/Y_4 = Y_2/Y_5$ . The implications of this choice will be discussed below. Thus, the values of anisotropy in the preferred material frame, which are proposed for subsequent study, are

$$Y_i = \langle 3.41 \ 3.86 \ 3.86 \ 2.34 \ 2.65 \ 2.65 \rangle \text{ kbar.}$$

If one uses these values of strength for the material, then Hill's constants are readily determinable as

$$\langle F \ G \ H \ L \ M \ N \rangle = \langle .024 \ .043 \ .043 \ .0913 \ .0712 \ .0712 \rangle \text{ kbar}^2.$$

These values may be employed in equation (4-27) to give shear coupling ratios. The coupling ratios are tabulated in Table 4, as a function of material frame orientation  $\Gamma$ . Coupling ratios in excess of .23 are observed, for  $\Gamma$  equal to 30 degrees. Recall that the analytical study of the collapsing anisotropic liner element indicate that coupling ratios of .05 are sufficient to spin compensate a shaped-charge liner.

A parametric study was done to reveal how shear coupling is influenced by the choice of shear strength,  $Y_6$ . Results indicate, regardless of  $Y_6$ , that the shear coupling ratio (maximized wrt  $\Gamma$ ) always exceeds the .05 value necessary for spin compensation. If, for example, the experimentally measured shear strength value of 2.49 kbar had been assumed for  $Y_6$ , a  $\Gamma$  maximized coupling ratio of .19 results, which still exceeds the .05 required for spin compensation. The parametric study has revealed, through variation in the 12 shear strength ( $Y_6$ ), that the coupling ratio (maximized wrt  $\Gamma$ ) reaches an absolute

TABLE 4. Shear to Normal Coupling Ratios for Material with Yield Characteristics  
 $Y_i = \langle 3.41 \ 3.86 \ 3.86 \ 2.34 \ 2.65 \ 2.65 \rangle$  kbar

$\Gamma$ (degrees)	$(\epsilon_{12}'/\epsilon_1')$
0	.0000
10	.1136
20	.2025
30	.2308
40	.1609
50	.0107
60	-.1183
70	-.1492
80	-.0948
90	.0000

minimum when  $Y_6$  is chosen at 2.05 kbar. Under this condition, the resulting coupling ratio of .063 still exceeds the amount necessary for spin compensation. The choice of  $Y_6$  equal to 2.65 kbar is thus reasonable, since the conclusions regarding the ability of anisotropy to produce spin compensation are unaffected by its variation.

It can be shown, if the  $A'_{ij}$  evaluation of (4-24) is carried out for rotations of  $\Gamma$  about the 1' axis (instead of the 3' axis), that there is no shear coupling of 1'2' ( $r\theta$ ) shear strain to any normal stresses. The implication of this fact is that the 1' ( $\theta$ ) direction can not be a preferred material direction if shaped-charge spin compensation is to result.

#### 4.3 Computational Studies.

In order to complement the analytical results showing the effect of anisotropic shear coupling on shaped-charge spin compensation, a computational modeling effort was put forth. The DEFEL<sup>43</sup> (Dyna East Finite Element Lagrangian) code was chosen as the modeling tool. As its name implies, DEFEL is a two dimensional explicit integration, Lagrangian, finite element code, which was designed to model explosive and/or isotropic material behavior. Its two dimensional nature permits modeling of plane strain, plane stress, or axisymmetric systems.

In order to make DEFEL usable in the present context of anisotropic material modeling, substantial modifications were necessary to DEFEL's constitutive model. An innovative formulation was developed for adding both elastic and plastic anisotropy modeling to DEFEL,<sup>44</sup> and are discussed in Appendix A. This formulation, limited to the study of plane stress and strain problems, was employed to study the behavior of collapsing thin walled copper cylinders. This work, described in a Section 4.3.1, closely parallels the analytical work on collapsing anisotropic cylinders from Sections 4.2.2 and 4.2.3.

It was desired, if possible, to computationally model the collapse of an anisotropic shaped-charge liner. Unlike Weickert's problem of modeling fluted liner collapse,<sup>2</sup> where the problem is truly three dimensional, the collapse of an anisotropic liner is a generalized axisymmetric ( $d/d\theta = 0$ ) problem. As such, there is no theoretical reason why it can not be modeled by an two dimensional axisymmetric code like DEFEL. However, a practical limitation exists in that DEFEL does not keep track of three dimensional element rotation (it

only tracks rotation in the r-z plane). For the modeling of an anisotropic material, in which the properties in the laboratory frame are very dependent on the orientation of the material's preferred coordinate system with respect to the lab frame, a means to track rotation out of the r-z plane was required. Such a means was developed, and is described in Appendix B.

Following validation of the axisymmetric code version, the collapse of a BRL 81 mm shaped-charge liner was modeled. The results, presented in detail in a subsequent section, confirm the analytical results which indicate that spin compensation via mechanical anisotropy is highly feasible.

#### 4.3.1 Plane stress collapse of anisotropic cylinders.

Though the simulations represent the plane stress collapse of circular cylinders, the size of the cylinder and the collapse velocity were chosen to approximate a slice of a typical shear-formed shaped-charge liner. The cylinder geometry used in the simulation is shown in Figure 24. The initial collapse velocity (V) was set to 2 km/sec. The material characteristics in the preferred coordinate system are the same as those employed in previous analyses, namely

$$Y_i = \langle 3.41 \ 3.86 \ 3.86 \ 2.34 \ 2.65 \ 2.65 \rangle \text{ kbar.}$$

The anisotropy angle in the r- $\theta$  plane ( $\Gamma$ ) was systematically varied from 0 to 90 degrees in increments of 10 degrees. Additionally, the case of  $\Gamma$  equal to 45 degrees was also examined.

Using the periodic boundary condition formulation described by Weickert<sup>2</sup>, the simulation of the circular cylinder was possible by considering only a single row of computational elements, aligned in the radial direction.

In all the simulations, the anisotropy manifested itself by causing the inner and outer surfaces of the cylinder to counter-rotate. A typical ( $\Gamma = 10$  degree) distorted geometry plot is shown in Figure 25. The figure depicts the collapsing cylinder at 11.2 microseconds. Naturally, the original cylinder is still a cylinder, albeit thicker and of smaller radius. However, the line of elements, originally aligned with the radial axis, have distorted in the

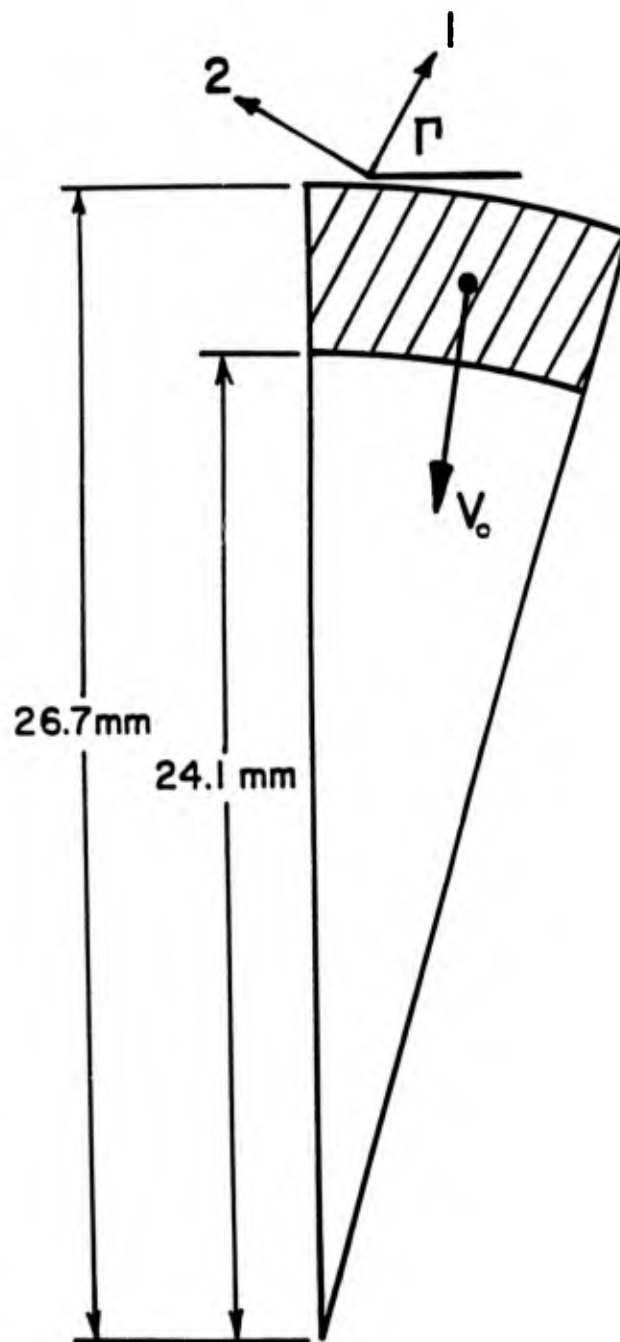


Figure 24. Cylinder geometry used to study collapse of anisotropic cylinders, under conditions of plane stress and strain.

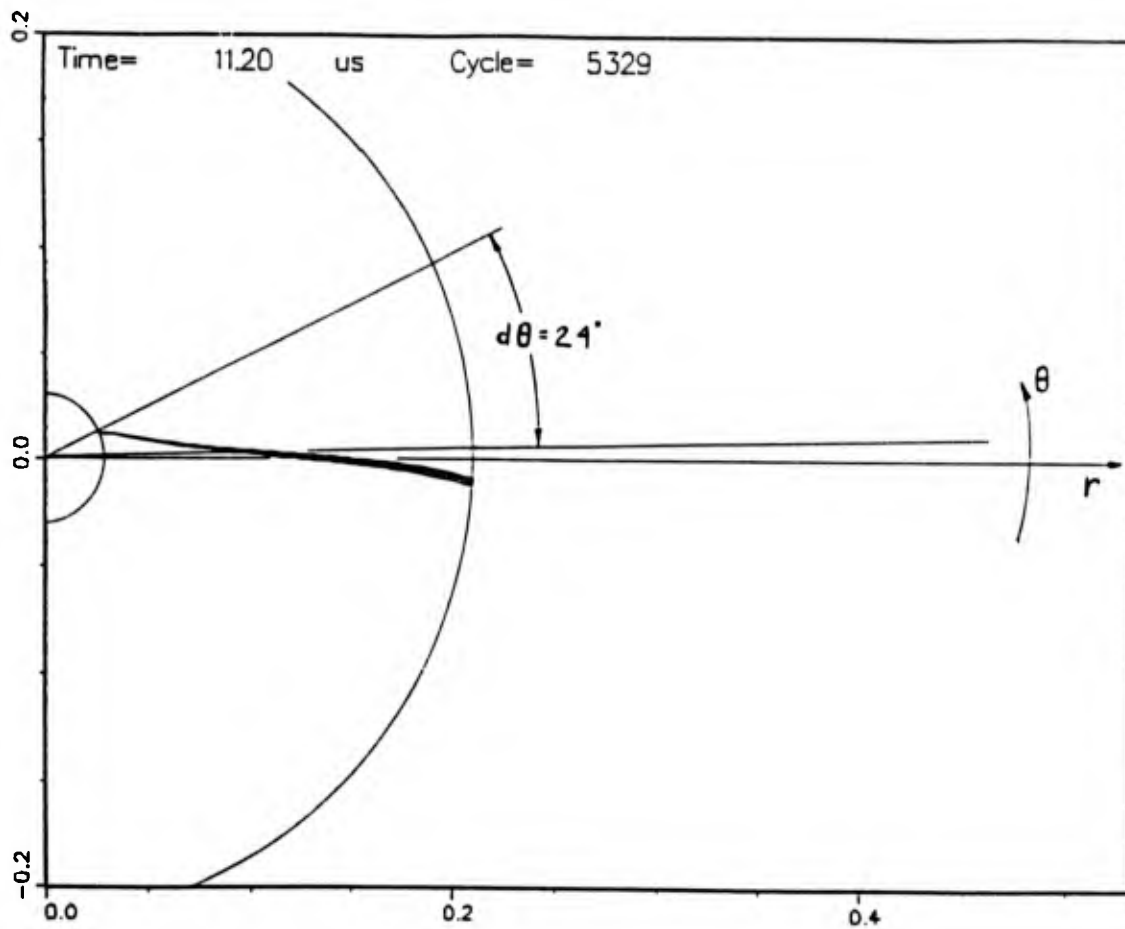


Figure 25. Distorted cylinder geometry plot of plane stress cylinder at 11.2  $\mu$ s. Inner surface of cylinder has rotated 24 degrees.

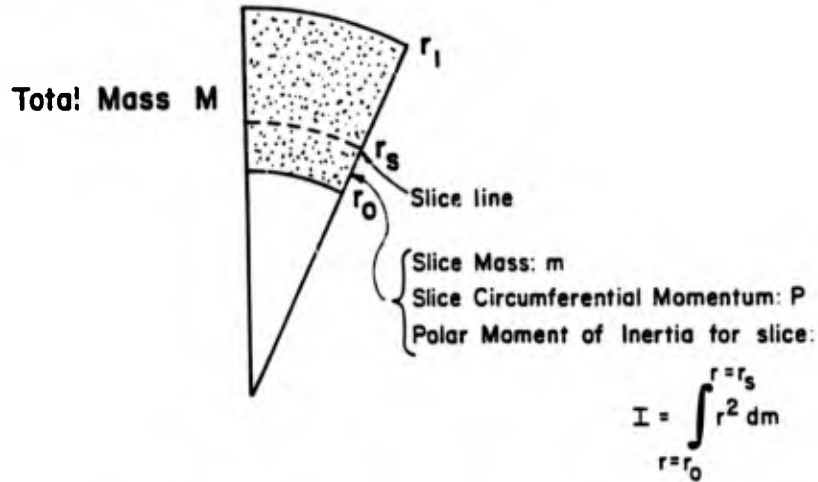
$\theta$  direction. As shown on the figure, the inner surface of the cylinder has circumferentially rotated approximately 24 degrees during the collapse. The cylinder has not collapsed totally onto the axis as of 11.2 microseconds, but computational element distortion caused the computational time step to become prohibitively small, forcing further computation to be abandoned.

A suitable means was sought to represent the data acquired during the simulations. One technique which provides good insight into the situation involves taking progressively larger slices from the inside of the cylinder, and observing the cumulative momentum characteristics of the particular slice. The technique is depicted in Figure 26. The advantage of displaying data in momentum averaged form through the slice is that the comparison to shaped-charge jet data becomes relevant, since the net spin of a jet is exactly this momentum averaged rotation rate from the inside skin of the liner, since it is the inner liner skin which forms the jet.

The net spin was determined as a function of slice size, for all cases of the parametric study. As described in Figure 26, the spin is a momentum averaged rotation rate through a given thickness of the cylinder, expressed in terms of the mass fraction of the cylinder slice. The plot of the net cylinder spin versus the mass fraction of the slice is depicted for a typical case ( $\Gamma = 10$  degrees) in Figure 27. This figure shows the inner surface of the liner to be rotating at a very high angular velocity (200,000 rps). However, as the slice size increases, the net angular velocity quickly drops off. When the inner 25 percent of the liner mass is considered, the net angular velocity is 30,000 rps. Naturally, when the full cylinder is considered (mass fraction of 100 percent), the net cylinder spin is identically 0 rps, since angular momentum of the system is conserved.

A notable trend is observed in the data. Namely, the sense of spin changes as the principal frame of anisotropy varies between the  $\Gamma = 50$  and 60 degree cases. Recall that for the analytical study (Section 4.2.3) whose results are depicted in Table 4, the shear coupling also reverses sign between 50 and 60 degrees. In both the analysis of Section 4.2.3 and the current simulations, hoop stress provides the only force on the collapsing body. It is thus encouraging to note that both analysis and numerical computation agree on this point. It should be mentioned that the shear coupling, and thus the angle at which shear coupling changes sign, are dependent upon the stress/strain loading conditions.

Total Circumferential Momentum = 0



$$\omega_{net} = \frac{P}{I} = \omega_{net} \left( \frac{m}{M} \right)$$

Figure 26. Net angular velocity of liner slice ( $\omega_{net}$ ) may be acquired as a function of cumulative mass fraction ( $m/M$ ).

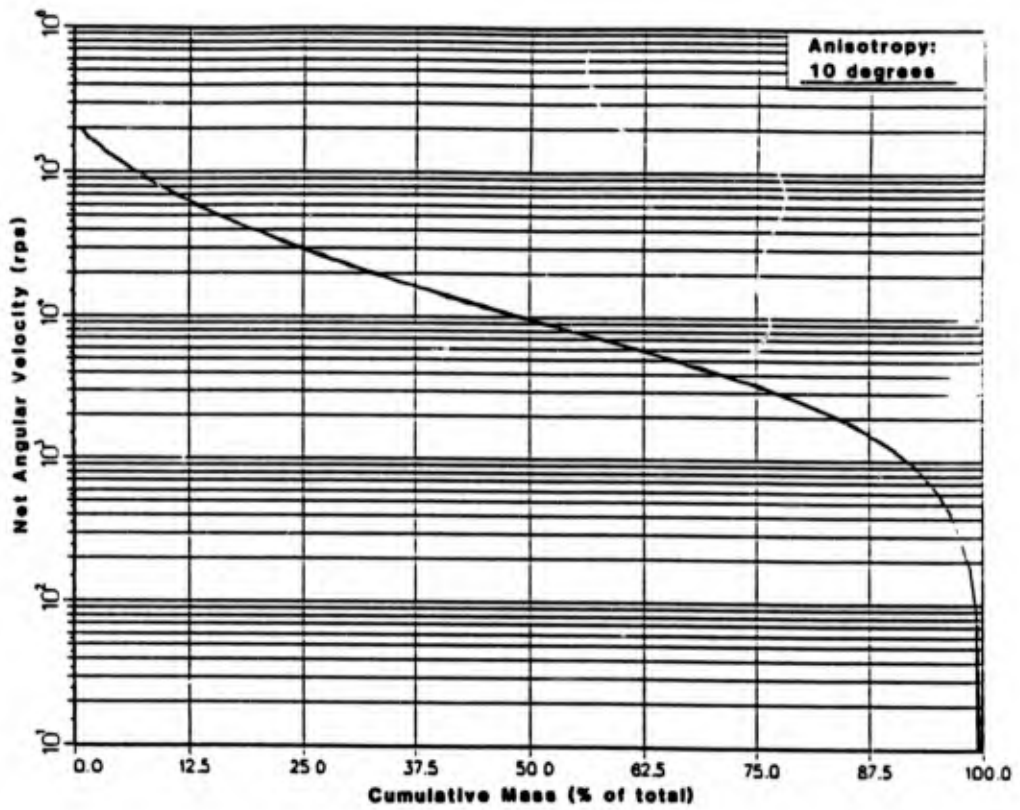


Figure 27. Net angular velocity of liner slice versus percentage of cumulative mass (m/M), for an anisotropic plane stress cylinder,  $\Gamma = 10$  degrees.

Thus, different boundary conditions will produce a different transition angle at which shear coupling reverses sign.

To this end, a series of plane strain (infinitely long) hollow cylinder collapses were modeled, with various anisotropy angles  $\Gamma$ . The effect of modeling in plane strain, as it applies to the current study, is that an axial stress is applied to the collapsing cylinders. The transition angle of shear coupling reversal was found to be 45 degrees. This 45 degree plane strain transition angle may be verified on a theoretical basis, since the principal direction of strain for a plane strain collapsing cylinder is along a direction 45 degrees from the radial. Thus, with the orientation of principal strain coinciding with the material's preferred coordinates, there is no tendency to produce shear strain coupling.

Returning to the plane stress cylinder collapse simulations of interest, one may consider the inner 25 percent of the cylinder mass, and plot the net spin versus anisotropy angle  $\Gamma$ . This has been done in Figure 28. As previously mentioned, the direction of liner spin changes at an orientation between 50 degrees and 60 degrees for these plane stress simulations. The 25 percent choice for mass fraction in Figure 28 is chosen to simulate the mass fraction of a shaped-charge jet, though the qualitative dependence of spin on anisotropy direction is demonstrable with any mass fraction.

Finally, it should be pointed out that computations for cylinder spin were carried out on data gathered 11.2  $\mu$ s after the onset of cylinder collapse. It would be desirable to know the data at total collapse; i.e., when the hollow cylinder reduces to a solid one. The distorted nature of the computational elements preclude this, but an estimate may be obtained by ignoring material strength, and letting the cylinder collapse under its own inertia. By conserving angular momentum, the limiting spin value may be obtained for various mass fractions of the cylinder. Figure 29 portrays this limiting value of spin, which incidentally has been plotted adjacent to the curve calculated at 11.2  $\mu$ s. Because the cylinder's proximity to the axis of symmetry at 11.2  $\mu$ s, the increases in spin rate are not very large except near the inner skin of the liner. For instance, at the 25 percent mass fraction location, the net spin increases from 30,000 rps to approximately 38,000 rps. The increase is significant, but not excessive.

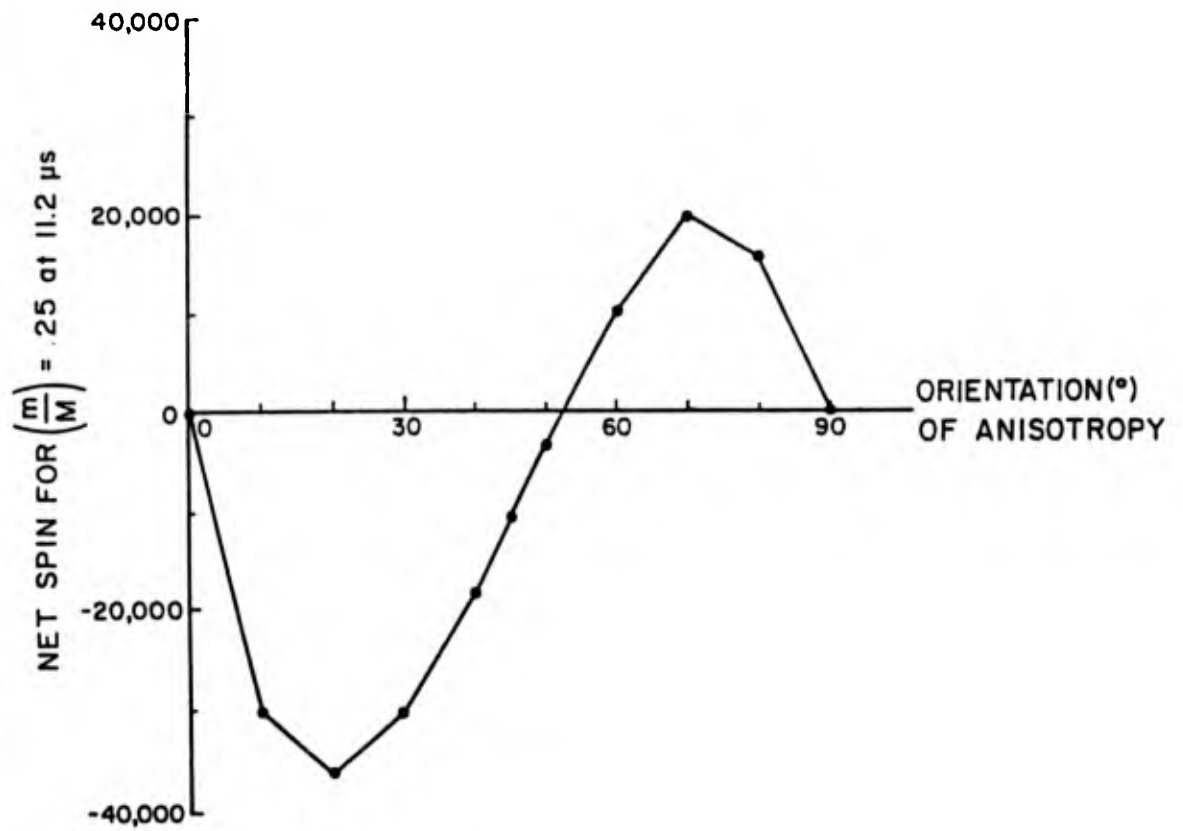


Figure 28. Net spin of inner 25 percent of liner slice, as a function of anisotropy orientation angle  $\Gamma$ , for fplane stress simulations at 11.2  $\mu$ s.

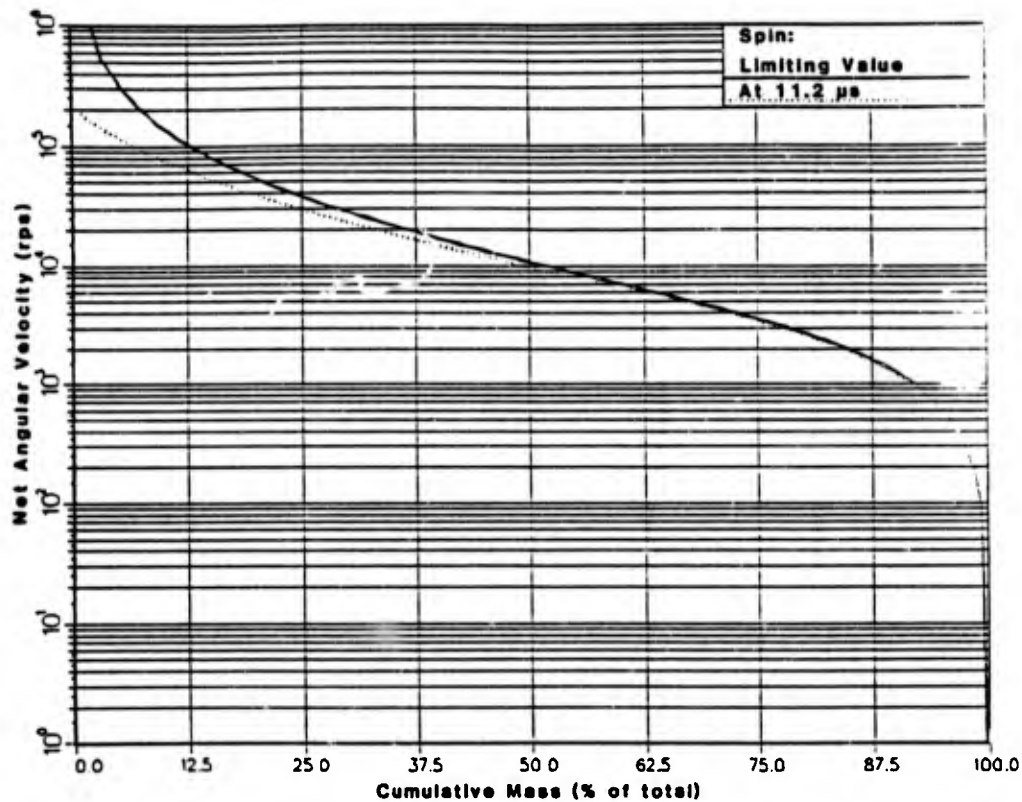


Figure 29. Limiting value and value at 11.2 μs of net angular velocity as a function of percentage cumulative mass (m/M), for anisotropic plane stress cylinder,  $\Gamma = 10$  degrees.

#### 4.3.2 Axisymmetric code validation.

The axisymmetric formulation was validated by means of collapsing cylinder simulations. For these simulations, the radial collapse of an axially thin, hollow cylinder (i.e., a washer) was modeled. Various anisotropies were introduced to the cylinder in an idealized fashion, so that simulation results could be checked with qualitative predictions, based on analysis of the plastic potential function.

In one simulation, a preferred material axis coincided with the  $\theta$  direction, with the other two preferred directions being offset 25 degrees in the r-z plane. Though asymmetric distortion occurred in the r-z plane, no tendency existed for the collapsing cylinder to experience motion in the  $\theta$  direction, in accordance with the plastic potential analysis of Section 4.2.3.

Another simulation had a preferred material axis coinciding with the z direction, and the remaining two material axes offset in the r- $\theta$  plane. As predicted by the cylinder collapse and shear coupling analyses of Sections 4.2.2 and 4.2.3, shear velocity was experienced in the r- $\theta$  plane, the inside of the cylinder rotating in one direction, the outside in the other direction.

The final validation simulation had a preferred material direction coincide with the cylinder's radial axis, the other two offset in the z- $\theta$  plane. The results of this cylinder collapse had the top and bottom of the cylinder (the +z and -z sides) rotating in opposite directions. The motion of the cylinder is antisymmetric about a plane  $z = \text{constant}$  located at the midplane of the cylinder. Again, such simulation behavior is in accordance with anticipated results.

#### 4.3.3 Axisymmetric collapse of an anisotropic liner.

The explosively actuated collapse of a BRL 81 mm shaped-charge liner was modeled with the DEFEL code modified for axisymmetric anisotropic behavior. The initial geometry grid of the charge is shown in Figure 30. Material characteristics in the preferred direction are identical to those employed in previous analyses, namely

$$Y_i = \langle 3.41 \ 3.86 \ 3.86 \ 2.34 \ 2.65 \ 2.65 \rangle \text{ kbar.}$$

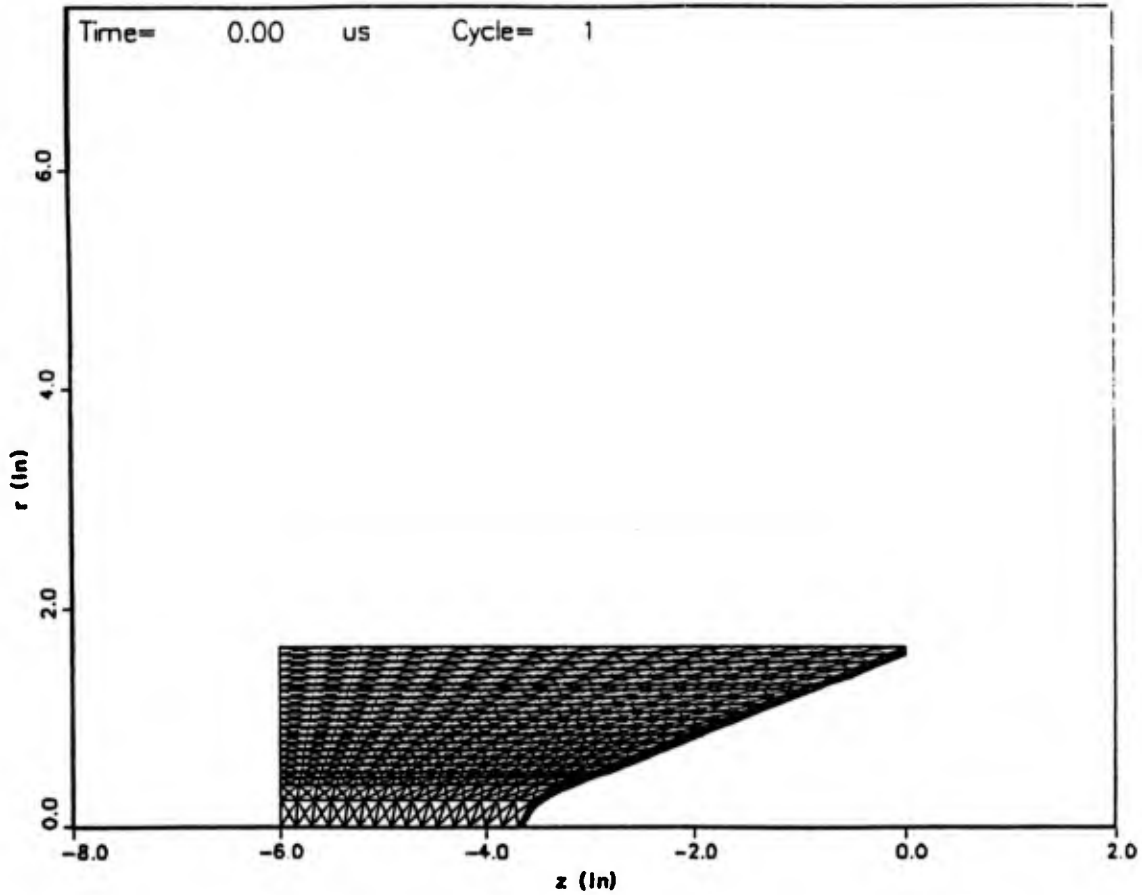


Figure 30. Initial grid geometry of the axisymmetric simulation involving the collapse of an anisotropic BRL 3.2 liner.

The anisotropy angle in the  $r-\theta$  plane ( $\Gamma$ ) was chosen so that the 1 axis is located 5 degrees from the  $\theta$  direction. This choice of  $\Gamma$  produces  $r-\theta$  shear coupling of .058, which approximates the .05 value analytically computed as necessary to produce the expected value of 35 rps spin compensation in the BRL 81 mm shaped-charge liner. The deformed geometry at 45 microseconds is displayed in Figure 31, along with a plot of angular velocity versus jet position. This figure clearly shows evidence of a rotational jet. The angular velocity plot in Figure 31 was generated by dividing the simulation into discrete axial zones, and taking the ratio of the angular momentum to the moment of inertia for each of the various zones. The discrete angular velocity points, corresponding to the center of each zone, were then connected via a smooth curve.

To get a better idea of the distribution of angular velocity within the jet, the outline of the distorted geometry at 45  $\mu$ s is plotted with several angular velocity contours in Figure 32. The aspect ratio of the  $r-z$  axis system has been altered, to give a clearer picture of the internal angular velocity contours. The figure shows that the angular velocity through a given jet cross section is generally uniform.

Similar contours are plotted for the same jet at an earlier stage of jet formation (25  $\mu$ s) in Figure 33. Though the rotational velocities are of a similar magnitude near the jet core, the surface of the thicker jet is rotating at a reduced magnitude. This trend is in accordance with predictions, since a jet radius which decreases in time will cause the angular velocity to correspondingly increase.

To demonstrate that it is the decreasing jet radius, and not anisotropy effects which accelerate the jet following the onset of jet formation, angular momentum contours are plotted for the same two formation times (25 and 45  $\mu$ s) in Figures 34 and 35. It is seen in these figures that the same contours occur at essentially the same physical location in the jet at these two times; thus, the angular momentum of material points in the jet is not changing with time. It can therefore be concluded that anisotropy introduces angular momentum to the liner prior to jet formation. When one examines the non-collapsed liner portion of Figure 34, it is seen that the same angular momentum contour which is found in the fully formed jet exists in the liner early on in the collapse process, prior to jet formation. Such behavior is in full agreement with the shear velocity model proposed in Section 4.2.2 of this report. To further illustrate this point, the angular momentum of several points on the liner is shown in Figure 36, with the locations of these points on the

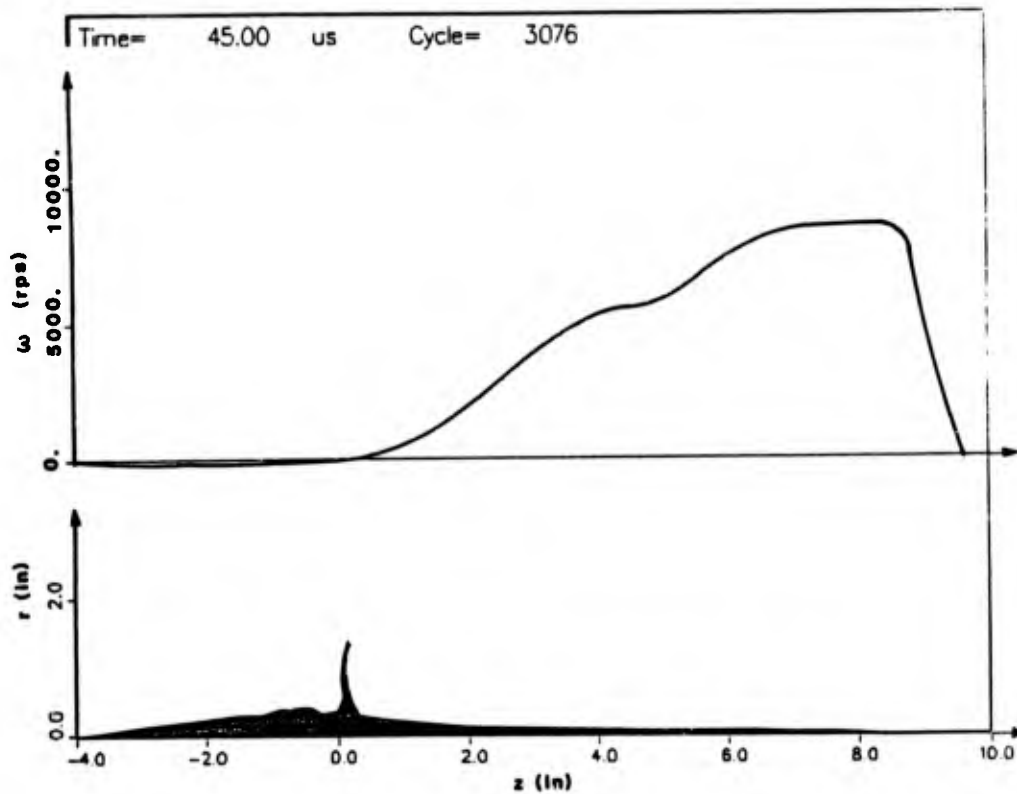


Figure 31. Deformed grid geometry of anisotropic jet, with a plot of jet angular velocity versus jet location, both at 45  $\mu$ s.

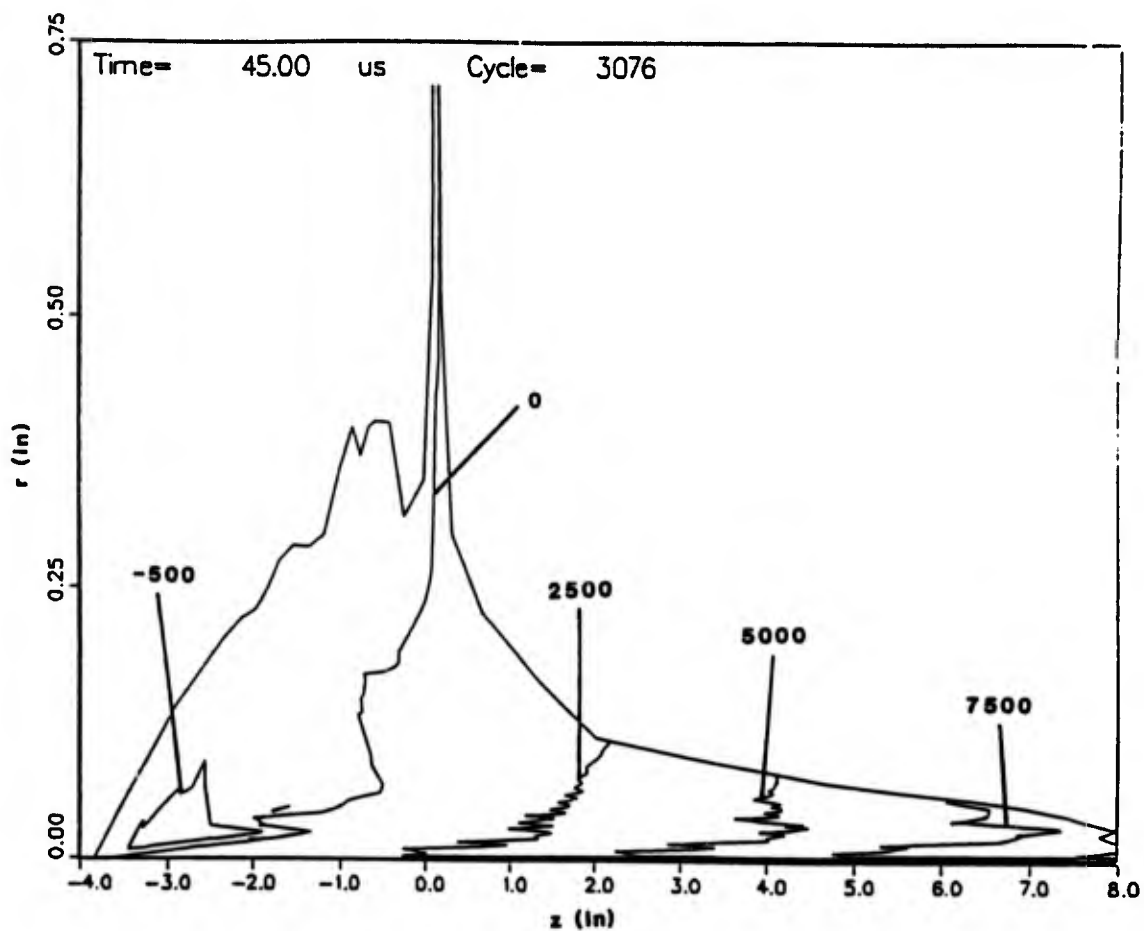


Figure 32. Angular velocity contour plot of anisotropic jet at 45  $\mu$ s.  
 Unity aspect ratio has not been preserved.

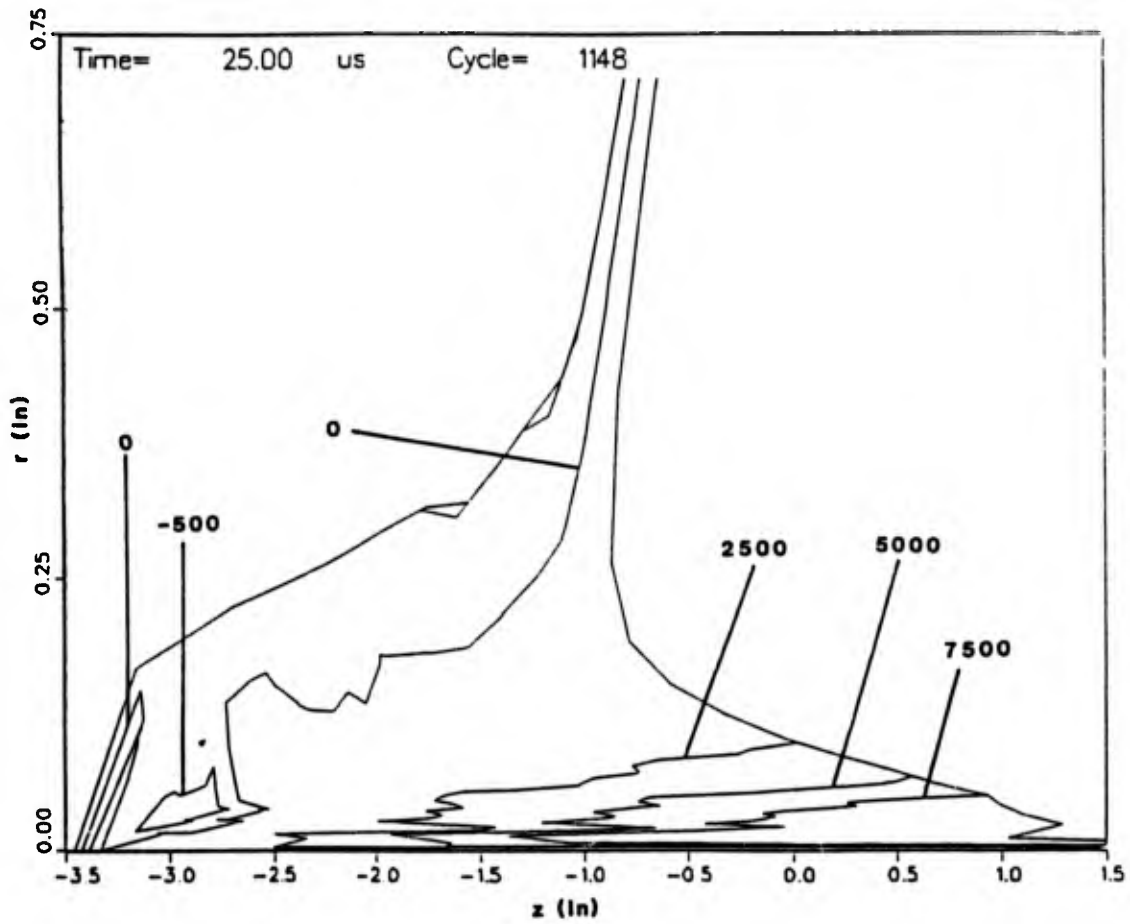


Figure 33. Angular velocity contour plot of anisotropic jet at 25  $\mu$ s.  
Unity aspect ratio has not been preserved.

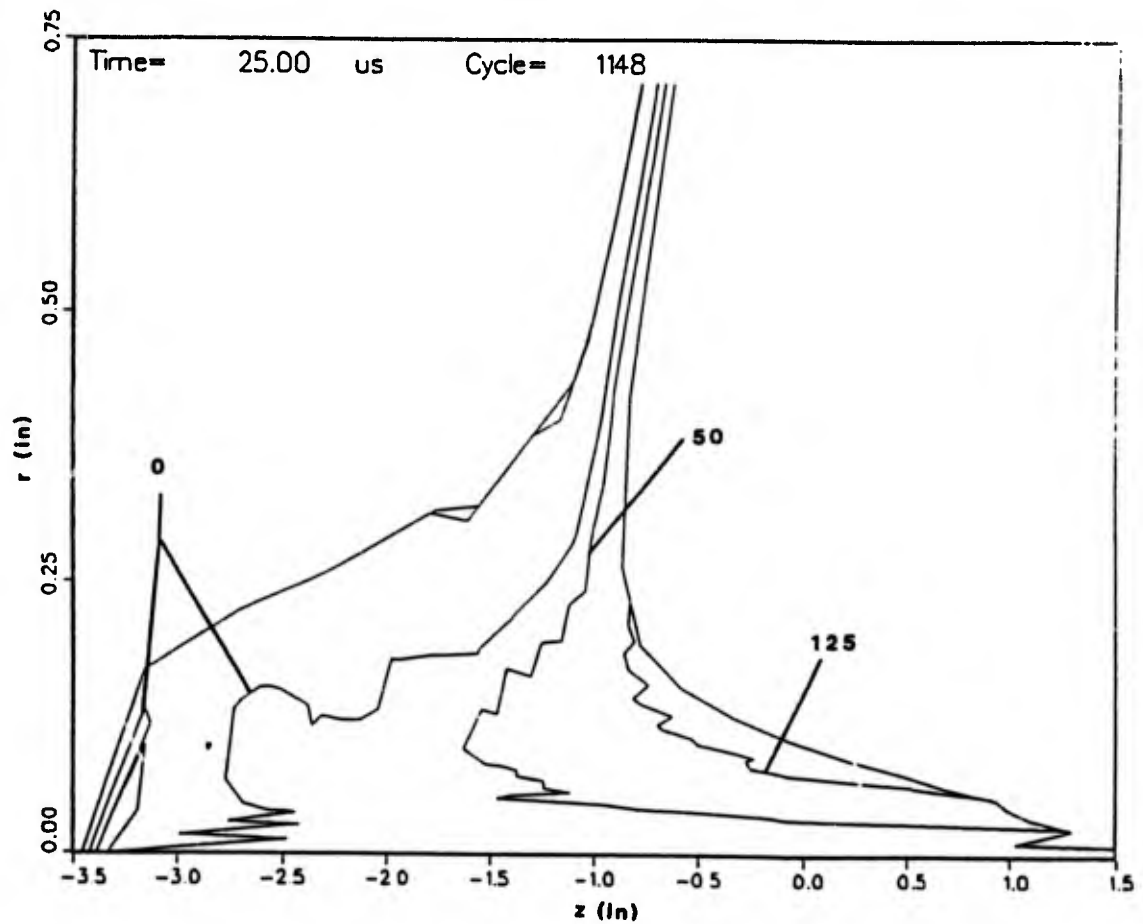


Figure 34. Angular momentum per unit mass ( $\text{in}^2/\text{s}$ ) contour plot of anisotropic jet at 25  $\mu\text{s}$ . Unit aspect ratio has not been preserved.

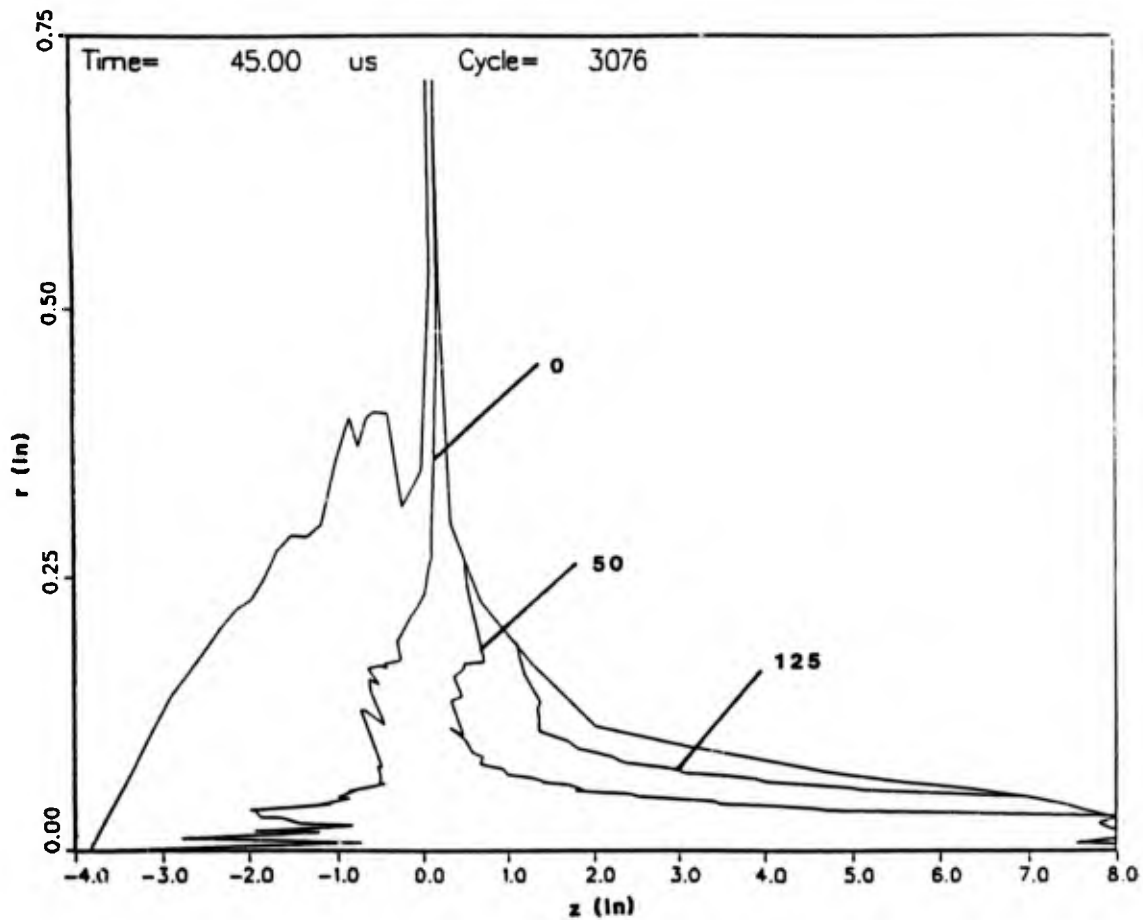


Figure 35. Angular momentum per unit mass ( $\text{in}^2/\text{s}$ ) contour plot of anisotropic jet at  $45 \mu\text{s}$ . Unity aspect ratio has not been preserved.

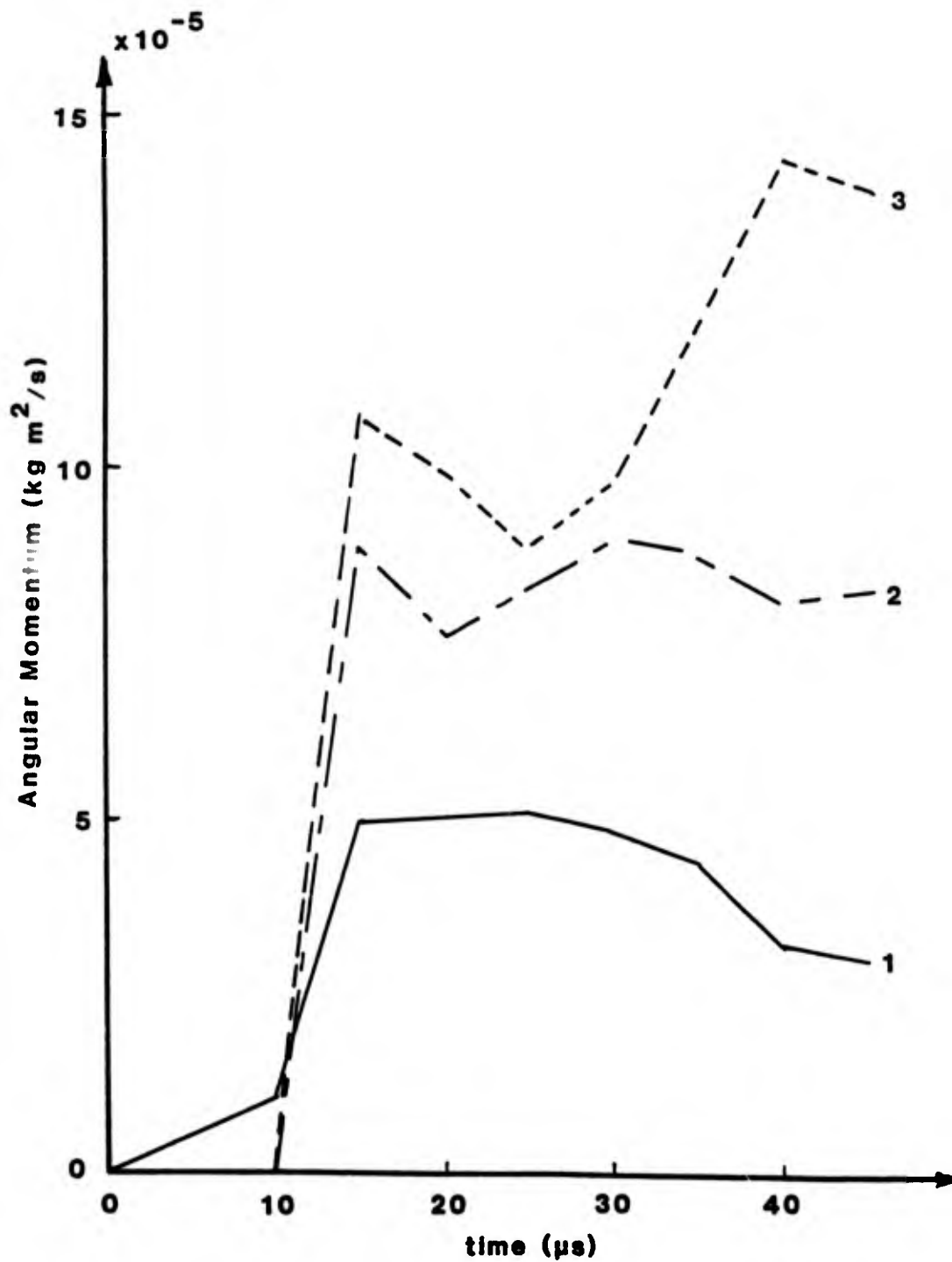


Figure 36. Time history graph of angular momentum for several points on the anisotropic BRL 3.2 liner.

original liner depicted in Figure 37. For points on the inside liner surface (those which end up in the jet), momentum is acquired quite early in the collapse process, and changes little thereafter.

In order to determine the spin compensation frequency of the anisotropic BRL 81 mm liner under study, other numerical simulations were performed in which initial charge spin was placed on the liner (in a direction opposite the observed anisotropy induced spin). By observing the angular velocity characteristics of the resultant jets, it was determined that the spin compensation frequency for the charge under study is indeed the expected value of 35 rps. A plot of the jet spin versus axial particle velocity is shown in Figure 38 for both the unspun anisotropic charge originally simulated and the same charge rotated 35 rps. It is seen that at the spin compensation frequency, the angular velocity of the jet is nearly negligible.

It was shown earlier from analytical considerations, if the  $\theta$  direction is a preferred material direction (so called r-z anisotropy, since the anisotropy angle  $\Gamma$  lies in the r-z plane), that induced jet rotation was not possible. However, it was shown, if the radial r direction was a preferred material direction, that induced  $\theta$  motion was possible. As such, a final axisymmetric simulation was performed of the collapsing liner with z- $\theta$  anisotropy. The results indicate small, random, material rotations in and out of the r-z plane, but more than an order of magnitude below the results of r- $\theta$  anisotropy discussed earlier. Though there is indeed variation of properties in the r- $\theta$  plane with the case of z- $\theta$  anisotropy, a transformation of the strengths into the laboratory r-z- $\theta$  coordinate system reveals that strength extrema in the r- $\theta$  plane coincide exactly with r and  $\theta$  coordinate directions. Under these conditions, there is no tendency for r- $\theta$  shear coupling, and thus any coupling must be z- $\theta$  coupling. Apparently, the stresses tending to produce out of plane rotations from z- $\theta$  coupling are not mutually constructive as in the case of r- $\theta$  anisotropy, and compensation therefore does not result.

## 5. CONCLUSIONS AND RECOMMENDATIONS

This report has addressed several mechanisms by which rotation might be induced in a jet of a stationary shaped charge which employs a shear-formed liner. In particular, two modes of residual stress relief have been examined, along with elastic and plastic mechanical anisotropy. Results indicate that plastic anisotropy is the only mechanism

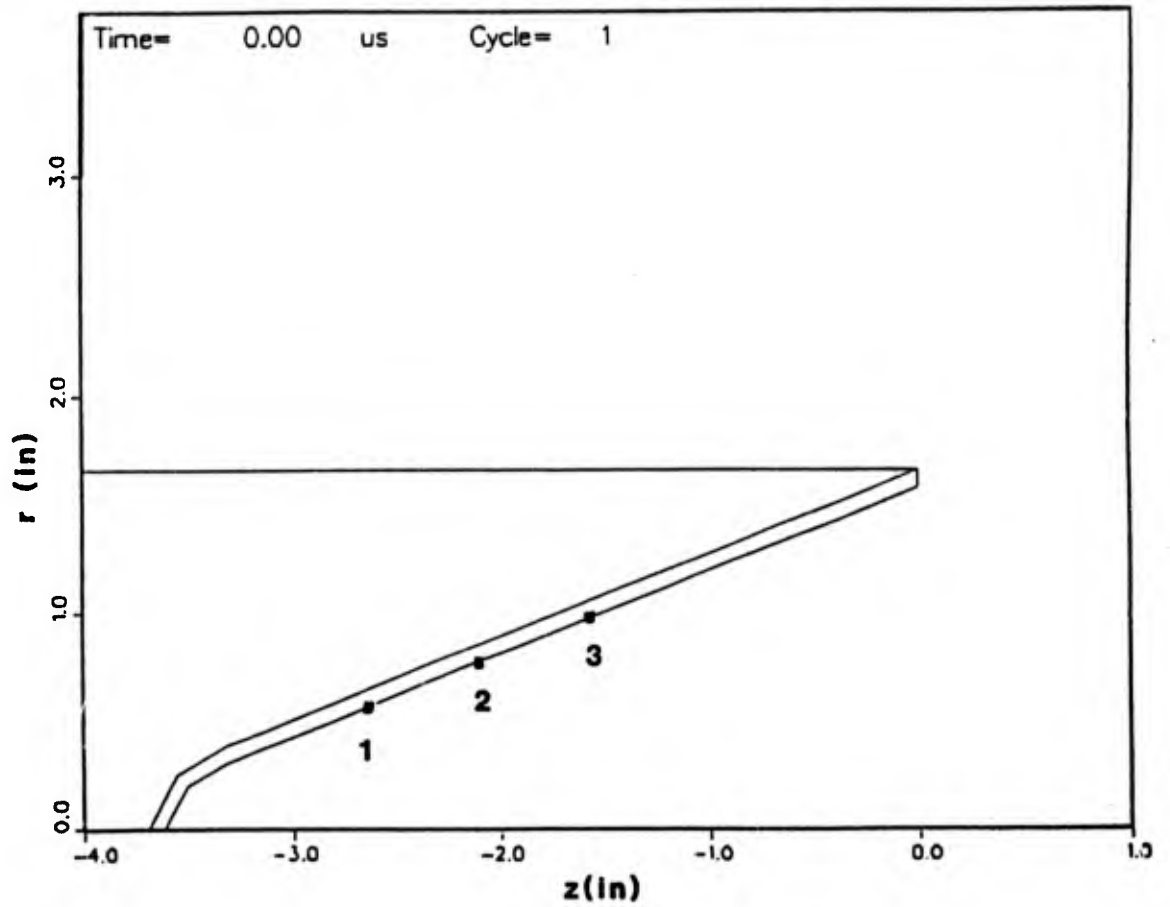


Figure 37. Initial outline of simulation geometry, depicting material points whose angular momentums have been traced in time.

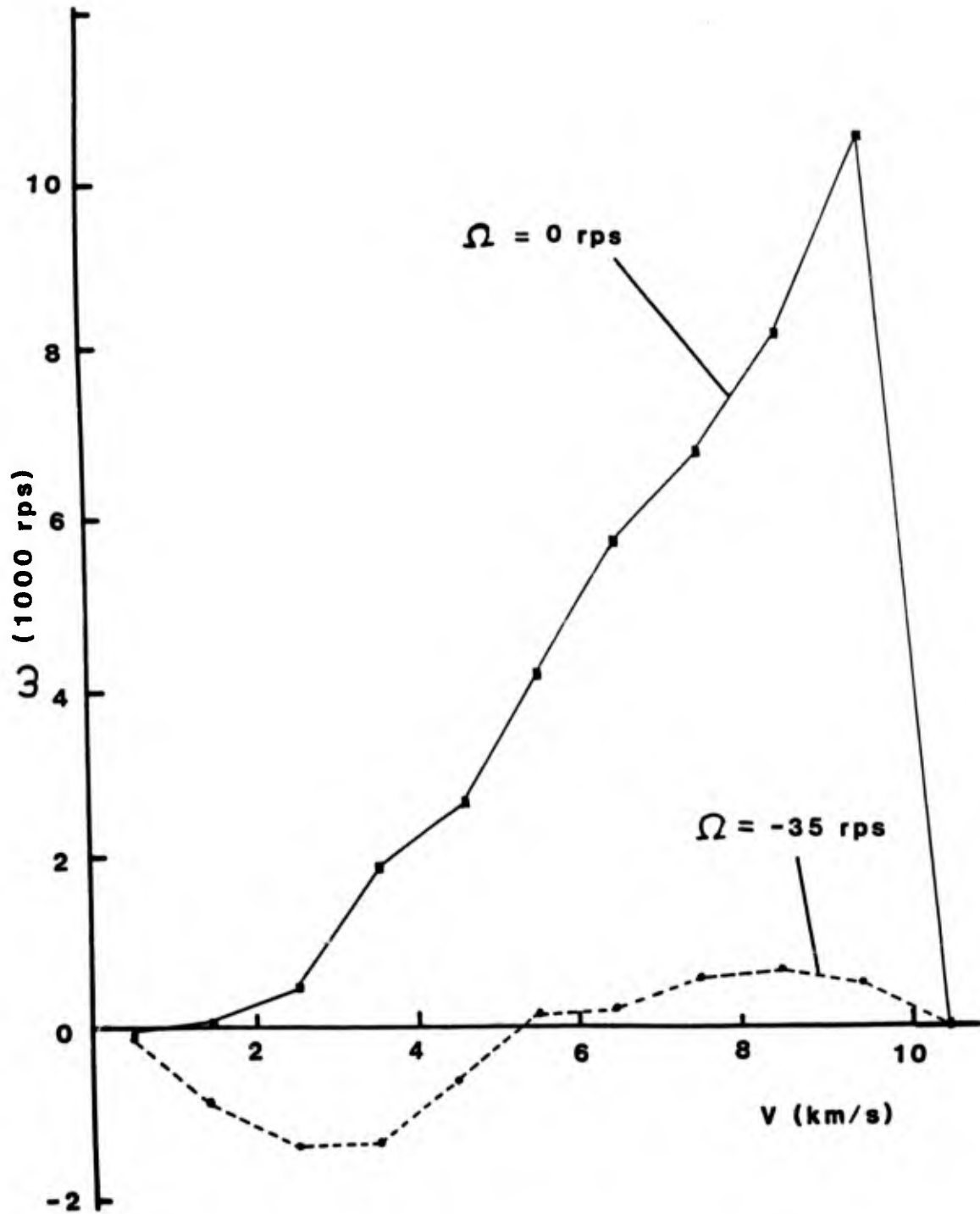


Figure 38. Jet spin versus axial jet velocity for unspun charge and charge spun at 35 rps opposite direction of spin compensation.

studied which is capable of producing jet rotation rates of the magnitude observed experimentally in shear-formed shaped-charge liners. In support of the report, several advances were made in related areas.

A computational anisotropic formulation was developed<sup>44</sup> which offers significant benefits over previous anisotropic formulations, in terms of computational accuracy. The computational formulation, being the first treatment of anisotropy from a deviator stress/strain perspective, provides an enhanced understanding of the mechanics of anisotropic deformation.

In a related effort, a means was developed to track the rotation of computational elements out of the r-z plane. The formulation is instrumental in performing anisotropic computational simulations in axisymmetry mode.

The analytical model developed to predict the spin compensation resulting from plastic anisotropy was compared to computational results of anisotropic liner collapse. The 2-D anisotropic plane stress and axisymmetric computational results match the analytical predictions in both magnitude and character, thereby supporting the validity of the analytical model of anisotropic spin compensation.

The plastic potential gradient of an anisotropic material was derived for a specific non-preferred coordinate system, resulting from a single coordinate rotation. The resulting plastic flow rule has been expressed in terms of the preferred coordinate system potential gradient augmented by a deviation potential gradient. Though the potential is not derived for arbitrary (three parameter) rotations from the preferred coordinate system, it nonetheless provides a useful tool for examining the effect of coordinate system rotations on shear coupling ratios.

Future examination of the report topic would be quite valuable from the perspective of material characterization. As it was, anisotropic material parameters for shear-formed liners were extrapolated from incomplete rotary forged tensile data. In the long term, the acquisition of macroscopic mechanical properties (e.g., yield strengths) of liner material from metallurgical considerations, though beyond the scope of the current research, would provide the vital link which might allow one to choose the metal forming process necessary to produce a liner of the proper anisotropic characteristics. Through this means, one

should be able predict the spin compensation ability of the shaped-charge liner in advance of manufacture. In the near term, the development of better methods to acquire the necessary macroscopic mechanical properties of liner material would permit one to predict spin compensation behavior of a liner without actually conducting a costly experimental shaped-charge testing program.

## 6. REFERENCES

1. Walters, W., "Fundamentals of Shaped Charges," Fundamentals of Shaped Charges, Vol. 1, Baltimore: Computational Mechanics Associates, pp. 20-40, 1988.
2. Weickert, C.A., "Spinning Self-Forging Fragments and Shaped Charges," Ph.D. Thesis, Drexel University, June 1986.
3. Birkhoff, G., MacDougall, D.P., Pugh, E.M., and Taylor, Sir G., "Explosives with Lined Cavities," *Journal of Applied Physics*, 19:6, pp. 563-582, June 1948.
4. Eichelberger, R.J., "Spin Compensation," Critical Review of Shaped Charge Information, BRL Report 905, Chapter VIII, pp. 215-253, May 1954.
5. Zernow, L., "The Effect of Rotation Upon Shaped Charge Jets," Critical Review of Shaped Charge Information, BRL Report 905, Chapter VII, pp. 177-213, May 1954.
6. Zernow, L. and Simon, J., "Flash Radiographic Study of Spin Compensation with 105 mm Fluted Liners," *Shaped Charge Journal*, 1:1, July 1954.
7. Zernow, L. and Simon, J., "Flash Radiographic Study of Spin Compensation in Shear Formed Liners (ITE)," *Shaped Charge Journal*, 1:1, July 1954.
8. Simon, J. and Zernow, L., "'Metallurgical' Spin Compensation in Smooth Electroformed Liners," *Shaped Charge Journal*, 1:1, July 1954.
9. Litchfield, E.L. and Eichelberger, R.J., "Performance of 57 mm Fluted Cones Made for Dynamic Testing," *Shaped Charge Journal*, 1:2, October 1954.
10. Becker, K.R., "57 mm Fluted Liners," The Ordnance Corps Shaped Charge Research Report, BRL 4-55, October 1955.
11. Becker, K.R., "75 mm Fluted Liners," The Ordnance Corps Shaped Charge Research Report, BRL 4-55, October 1955.
12. Simon, J., "Flash Radiographic Study of Spin Compensation With 105 mm Fluted Liners," The Ordnance Corps Shaped Charge Research Report, BRL 4-55, October 1955.
13. Simon, J. and Zernow, L., "Flash Radiographic Study of Spin Compensation in 105 mm Copper Liners Manufactured by Controlled 'Spinning'," The Ordnance Corps Shaped Charge Research Report, BRL 4-55, October 1955.

14. DiPersio, R. and Simon, J., "An Empirical Approach to the Design of a Spin Compensating Shaped Charge," BRL Memorandum Report 1251, February 1960.
15. Zernow, L. and Simon, J., "High Strain Rate Plasticity of Liner Materials and Jet Behavior," BRL Report 954, August 1955.
16. Simon, J., DiPersio, R., and Eichelberger, R.J., "Shaped Charge Performance With Linear Fluted Liners," BRL Memorandum Report 1231, September 1959.
17. Simon, J. and Zernow, L., "Flash Radiographic Study of Certain Anomalous Electroformed Liners for Shaped Charges," BRL Memorandum Report 892, June 1955.
18. Simon, J. and Martin, T.K., "Spin Compensation of Shaped Charge Liners Manufactured by the Rotary Extrusion Process," BRL Memorandum Report 1181, December 1958.
19. Glass, C.M., Gainer, M.K., and Moss, G.L., "Effects of Anisotropies in Rotary Extruded Liners," BRL Report 1084, November 1959.
20. Gainer, M.K. and Glass, C.M., "A Study of Metallurgical Effects in High Velocity Deformation of Copper Using Rotary Extruded Liners," BRL Report 1167, May 1962.
21. Weickert, C.A. and Chou, P.C., "Shaped Charge Spin Compensation with Fluted Liners," Proc. 9th International Symposium on Ballistics, Shrivenham, UK, 29-30 April, 1 May, 1986.
22. Karpp, R. and Simon, J., "An Estimate of the Strength of a Copper Shaped Charge Jet and the Effect of Strength on the Breakup of a Stretching Jet," BRL Report 1893, June 1976
23. Dyna East Corporation, "Study of Jet Breakup and the Collapse of Spinning Liners," Quarterly Tech. Report for Contract DAAK11-78-C-0101, March 1979.
24. Timoshenko, S.P. and Goodier, J.N., Theory of Elasticity, 3rd ed. New York: McGraw Hill Book Co., Inc., 1970.
25. Zernow L. and Simon, J., "Flash Radiographic Study of Special Liners for Shaped Charges," BRL Report 936, June 1955.
26. Poulter, T., "A Study of Material for Shaped Charges: The Effect of Crystal Orientation on Jet Formation," Tech. Report No. 3, Poulter Laboratories, SRI Project No. GU-863 for BRL Contract No. DA-04-200-ORD-257, 15 February 1955.
27. Witt, F., "X-ray Studies on the Flared Cone Component for Metal Parts Assembly M456A1E1," FA-TR-74046, December 1974.
28. Witt, F., "X-ray Studies of Belgian Produced 105 mm HEAT-T-M456 Spin Compensated Shaped Charge Liners," FA-TR-75001, January 1975.
29. Feng, C., Witt, F., and Lee, F., "A Metallurgical Evaluation of Shear-Spun and Deep Drawn Copperhead Liners," ARDC Report MMB-57-80, 1980.

30. Feng, C., Lee, F., and Witt, F., "Metalurgical Comparisons Between Two Starting Stock Materials Used in the Improved TOW Shaped Charge Liner," ARDC Report MMB-18-81, March 1981.
31. Witt, F., US Army Armament Research, Development and Engineering Center, Picatinny Arsenal, NJ, private communication, December 1987.
32. Majerus, J., Golaski, S., and Merendino, A., "Influence of Liner Metallurgy, Apex Configuration and Explosive/Metal Bond Strength upon Performance of Precision Shaped-Charges," BRL Report ARBRL-TR-02451, December 1982.
33. Crilly, M., et al., "Evaluation of the Effect of Liner Grain Size on Shaped-Charge Performance," Project M13, Drexel University Senior Design Report, May 1984.
34. Nuclear Metals, Inc., "Material Certification and Dimensional Inspection Data for Ballistic Research Laboratory Contract No. DAAD05-85-C-4156," June 27, 1985.
35. Duffy, M. and Golaski, S., "Effect of Liner Grain Size on Shaped Charge Jet Performance and Characteristics," BRL Report BRL-TR-2800, April 1987.
36. Wenk, H.R., ed. Preferred Orientation in Deformed Metals and Rocks: An Introduction to Modern Texture Analysis, Orlando: Academic Press, 1985.
37. Cullity, B.D., Elements of X-ray Diffraction, Reading: Addison-Wesley, 1978.
38. Schiferl, S., Los Alamos National Laboratory, Los Alamos, NM, Private Communication, February 1988.
39. Hill R., The Mathematical Theory of Plasticity, London: Oxford Press, 1950.
40. Franz, R., US Army Ballistic Research Laboratory, Aberdeen Proving Ground, MD, Private Communication, January 1987.
41. Chou, A. and Labriola, M. Jr., "Rotary Forging - A Precision Process," *Mechanical Engineering*, 107:3, pp. 73-77, March 1985.
42. Baldwin, W.M., Jr., "Effect of Rolling and Annealing upon the Crystallography, Metallography, and Physical Properties of Copper Strip," Proc. 9th Sagamore Army Materials Research Conference, Raquette Lake, NY, August 28-31, 1962.
43. Flis, W.J., Miller, S., and Clark, W.J., "DEFEL: A Finite-Element Hydrodynamic Computer Code," Dyna East Technical Report DE-TR-84-05, November 1984.
44. Segletes, S., "Deviatoric Constitutive Relationship for Anisotropic Materials," BRL Report BRL-TR-2825, June 1987.
45. Baker, P., US Army Ballistic Research Laboratory, Aberdeen Proving Ground, MD, Private Communication, September 1988.
46. Dyna East Corporation, "DEFEL User's Manual," Dyna East Corporation Technical Report DE-TR-85-02, Second Revision, May 1985.

47. Johnson, G.R., "EPIC-2, A Computer Program for Elastic-Plastic Impact Computations Plus Spin," Final Report, Contract No. DAAD05-77-C-0730, US Army Ballistic Research Laboratory, December 1977.
48. Walsh, J.M. et al., "HELP, A Multi-Material Eulerian Program for Compressible Fluid and Elastic-Plastic Flows in Two Space Dimensions and Time." Vols. I and II, Systems, Science and Software, 3SR-350, June 1970.
49. Johnson, W. and Mellor, P.B., Engineering Plasticity, Chichester: Ellis Horwood, Chapter 5, 1983.
50. Hageman, L.J. et al., "HELP, A Multi-Material Eulerian Program for Two Compressible Fluid and Elastic-Plastic Flows in Two Space Dimensions and Time," Systems, Science and Software, SSS-R-75-2654, July 1975.
51. Vavrick, D.J. and Johnson, G.R., "Dynamic Analysis of Elastic-Plastic Anisotropic Solids," Honeywell Internal Report, Contract No. DAAK11-78-C-0010, US Army Ballistic Research Laboratory, October 1980.
52. Wu, L., Drexel University, Philadelphia, PA, Private Communication, November 1985.

INTENTIONALLY LEFT BLANK.

APPENDIX A:

DEVIATORIC CONSTITUTIVE RELATION  
FOR ANISOTROPIC MATERIALS

INTENTIONALLY LEFT BLANK.

APPENDIX A:  
DEVIATORIC CONSTITUTIVE RELATION  
FOR ANISOTROPIC MATERIALS

The information presented in this appendix is a summary of that found in reference 44. It is presented here to assist the reader in understanding the computational techniques developed for use in the current research.

A.1 Introduction.

It is desired to improve upon the ability to describe the behavior of anisotropic media subjected to large pressures, as is the case for hypervelocity impact. It is believed that expressing the anisotropic constitutive relationship in a form that makes use of the deviatoric stress and strain tensors provides for a better description of anisotropic materials whose compressibility is permitted to vary with volumetric strain. The deviatoric stress technique is used routinely in many impact codes for describing isotropic behavior<sup>46-48</sup>, and is described in many books on elasticity and plasticity.<sup>24,49</sup> Anisotropic schemes have also been developed for various impact codes<sup>50-51</sup> which calculate a deviatoric stress. However, the deviatoric stress is expressed in terms of a total strain and the bulk modulus. In a true deviatoric formulation, deviatoric stress is expressed only in terms of deviatoric strain, and compressibility affects only the equation of state, not the deviatoric stress/strain relation.

An anisotropic formulation is proposed which satisfies the condition of reducing to Hooke's Law/Prandtl Reuss Flow Rule when employing the constraint of constant compressibility and isotropy, but which conveniently allows for anisotropy and variable compressibility. Additionally, the formulation is amenable for inclusion into existing impact codes which presently use the deviatoric stress technique for isotropic materials. The scheme also provides an improved technique for calculating hydrostatic pressure which is less prone to error than existing techniques. Finally, it is hoped that the formulation provides an enhanced physical interpretation on the behavior of anisotropic materials which might otherwise be lacking.

## A.2 Background.

The constitutive relationship for any elastic material may be represented in contracted form as

$$\sigma_i = C_{ij} \varepsilon_j \quad (\text{A-1})$$

where  $\sigma_i$  and  $\varepsilon_j$  represent the six independent stress and strain components, and  $C_{ij}$  is the modulus matrix. The contracted form of the constitutive relation is used for the sake of simplicity, but the tensorial components of the contracted form are defined as follows:

$$\sigma_i = (\sigma_{11} \ \sigma_{22} \ \sigma_{33} \ \sigma_{23} \ \sigma_{13} \ \sigma_{12})$$

$$\varepsilon_i = (\varepsilon_{11} \ \varepsilon_{22} \ \varepsilon_{33} \ \varepsilon_{23} \ \varepsilon_{13} \ \varepsilon_{12})$$

In general,  $C_{ij}$  may be a function of  $\sigma$ ,  $\varepsilon$ ,  $\dot{\varepsilon}$ , etc. However, it is somewhat unwieldy as such, and is sometimes considered to be constructed of constants, which produces the familiar Hooke's Law. One reason why the deficiency of Hooke's Law becomes apparent experimentally under large pressures is that the bulk modulus of the material is quite different from the material's low stress value.

For isotropic materials, this problem has been computationally circumvented by the introduction of the deviatoric stress and strain tensors. These tensors differ from the absolute stress/strain tensors in that the normal components of stress and strain are decremented by the average of the normal stresses and strains respectively. In this way, the deviatoric quantities represent deviation from a hydrostatic condition, while the relationship existing between the average stress (negative of pressure) and average strain (volumetric dilatation) is an equation of state. Since experimental evidence reveals that the compressibility of many materials changes under large pressures, the deviatoric formulation suggests that while the simplicity of Hooke's Law (constant coefficients) might possibly be retained for computation of the deviatoric stresses and strains, a more accurate scalar equation of state should simultaneously be employed to account for non-linear compressibility effects.

### A.3 Elastic Deviatoric Anisotropy.

While the mathematics of the constant coefficient constitutive relationship for anisotropic materials is well understood, the casting of these rules into a deviatoric format is not nearly as straightforward as it is for isotropic materials. Difficulties arise because of two primary differences in the behavior of anisotropic materials with respect to that of isotropic materials:

a. under hydrostatic pressure, strain is not uniform in all three directions of the material coordinates, and

b. except under restrictive modulus conditions, deviatoric strain will produce volumetric dilatation (i.e., two different stress states with the same pressure will produce different dilatations in the material).

Decomposition of the stress and strain tensors into their hydrostatic and deviatoric components yields:

$$s_i = \sigma_i - \bar{\sigma}_i \quad (\text{A-2})$$

$$e_j = \epsilon_j - \bar{\epsilon}_j \quad (\text{A-3})$$

where  $\bar{\sigma}_i$  are all equal to the components of hydrostatic stress ( $\bar{\sigma} = (\sigma_1 + \sigma_2 + \sigma_3)/3$ ) for normal stress components and equal to zero for the shear stress components. The term  $\bar{\epsilon}_j$  represents the normal strains due to hydrostatic stress. One may acquire upon substitution into equation (A-1):

$$(s_i + \bar{\sigma}_i) = C_{ij} (e_j + \bar{\epsilon}_j) \quad (\text{A-4})$$

where barred quantities represent conditions resulting from a hydrostatic pressure,  $s_i$  and  $e_j$  are the deviatoric stresses and strains respectively, and  $C_{ij}$  is the modulus matrix. Unlike the isotropic materials in which a hydrostatic pressure produces a uniform dilatation in all three coordinate directions, hydrostatic strain for an anisotropic material is non-uniform. Therefore, if one defines the deviatoric components of stress and strain to be the total stress/strain components decremented by an amount which would result from a hydrostatic

stress state, one can conclude (per condition "a" above) that there is a unique hydrostatic strain component associated with all three directions in the material coordinates (the coordinate system which produces no shear coupling). Equation (A-4) may be decoupled to give a hydrostatic equation

$$\bar{\sigma}_i = C_{ij} \bar{\epsilon}_j \quad (\text{A-5})$$

and a deviatoric relationship void of hydrostatic terms:

$$s_i = C_{ij} e_j \quad (\text{A-6})$$

For the sake of clear visualization, the formulation will be described for transverse isotropy, though extension to orthotropy is straightforward<sup>52</sup>. Figure A-1 depicts material elements from an anisotropic body whose material (preferred) coordinate systems differ from the laboratory frame of reference. The preferred coordinate system is the reference frame in which the constitutive relation reduces to its most simple form. Figure A-2 shows properties of the preferred transversely isotropic material frame. Mechanical properties are invariant with respect to reference frame rotations that are confined to the plane of isotropy. As such, a certain symmetry of mechanical properties exist in transversely isotropic materials which are absent in orthotropic materials. The proposed model will be described in the material (preferred) coordinate system. Solutions of problems in which the laboratory frame and the material frame do not coincide pose no problem if one first transforms stress and strain to the material frame.

Under the influence of a purely hydrostatic stress state (and assuming the moduli to be constant), there will be a constant ratio between the anisotropic (longitudinal) strain  $\bar{\epsilon}_1$  and the transversely isotropic planar strain  $\bar{\epsilon}_2$ . Defining the ratio in terms of material compliances  $S_{ij}$  (where  $S_{ij} = (C_{ij})^{-1}$ ):

$$K_\epsilon = \frac{\bar{\epsilon}_1}{\bar{\epsilon}_2} = \frac{S_{11} + 2S_{12}}{S_{22} + S_{12} + S_{23}} \quad (\text{A-7})$$

it is seen that this parameter ( $K_\epsilon$ ) reduces to a value of unity for isotropy, where  $S_{11}$  will equal  $S_{22}$ , and  $S_{12}$  will equal  $S_{23}$ .

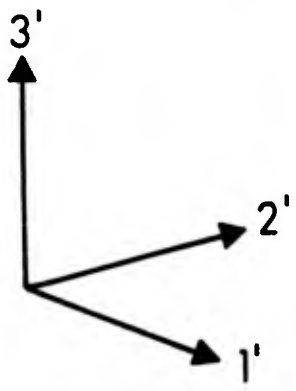
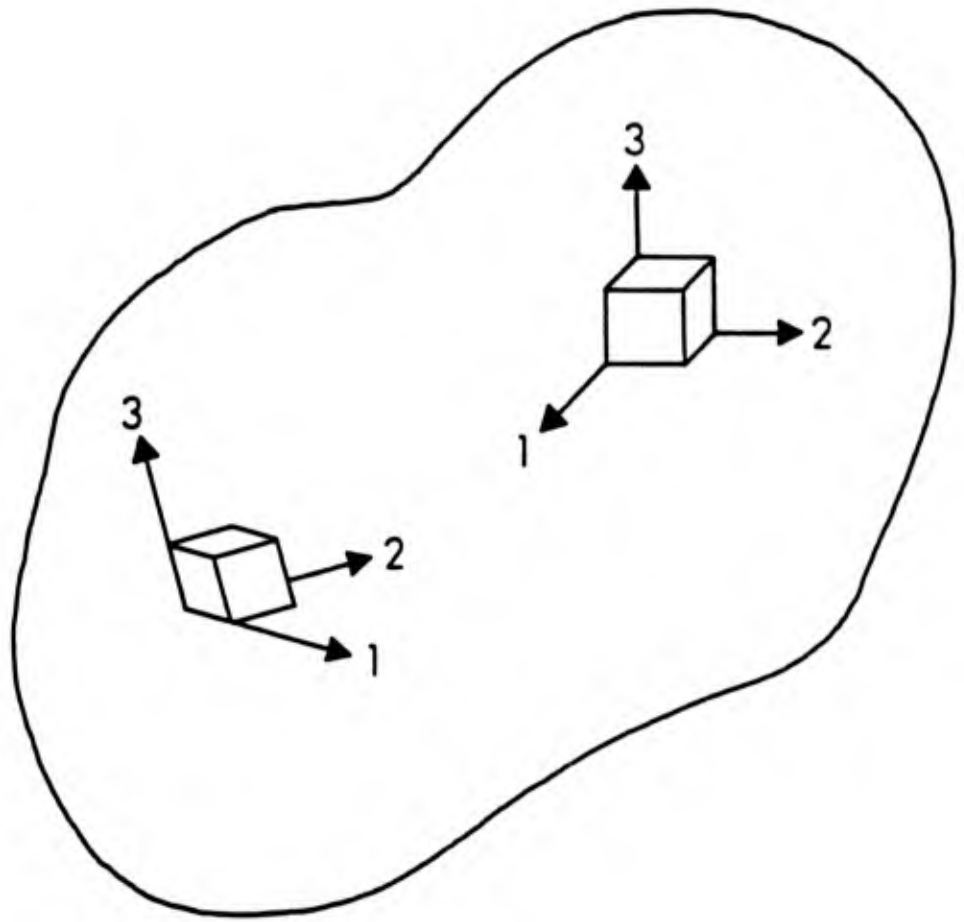
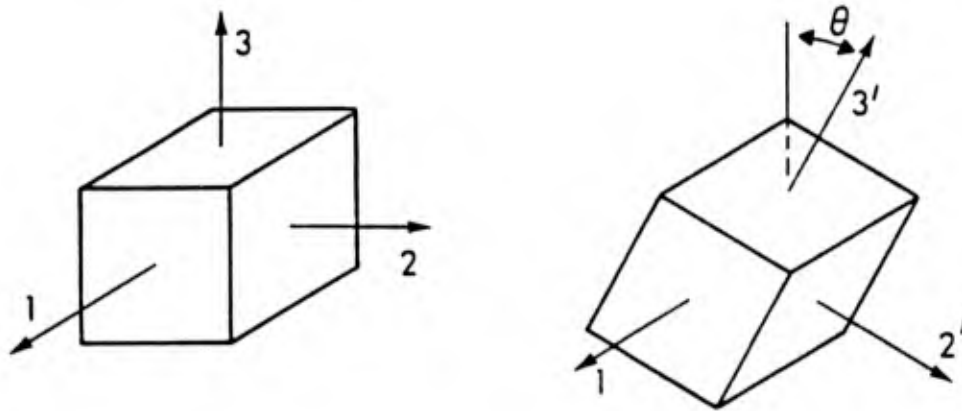


Figure A-1. Schematic depiction of general anisotropic body, where principal material directions are not generally aligned with laboratory axes.



$$\nu_{13} = \nu_{13'}, G_{13} = G_{13'}, E_3 = E_{3'}, Y_3 = Y_{3'}, Y_{13} = Y_{13'}$$

When  $\theta = 90^\circ$ , it follows that

$$\nu_{12} = \nu_{13}, G_{12} = G_{13}, E_2 = E_3, Y_2 = Y_3, Y_{12} = Y_{13}$$

Figure A-2. Transversely isotropic material properties are derivable from orthotropic properties, when plane of material symmetry is assumed.

Using the definition that deviatoric stress is that part of the stress tensor which deviates from the hydrostatic stress condition, one can conclude that the deviatoric stress has no hydrostatic component

$$s_1 + s_2 + s_3 = 0 \quad (\text{A-8})$$

One may substitute the deviatoric constitutive relation, equation (A-6), to acquire

$$K_\sigma e_1 + e_2 + e_3 = 0 \quad (\text{A-9})$$

where  $K_\sigma$  physically represents the ratio of longitudinal and transverse stress under conditions of uniform strain ( $\epsilon_1 = \epsilon_2 = \epsilon_3$ ), and is given by

$$K_\sigma = \frac{C_{11} + 2C_{12}}{C_{22} + C_{12} + C_{23}} \quad (\text{A-10})$$

As a result, the sum of the three normal deviatoric strain increments is not generally zero, but rather equals a deviatoric dilatation ( $\bar{e}$ ). The significance of this term is that a state of stress whose average normal value is zero can produce volumetric change on an element with respect to that element's stress free volume.

If one wishes to convert a given elastic strain state ( $\epsilon_i$ ) into the elastic deviators ( $e_i$ ), elastic deviatoric dilatation ( $\bar{e}$ ), and the hydrostatic strain components ( $\bar{\epsilon}_i$ ), the following nine equations given below may be used for a transversely isotropic material (whose plane of isotropy is the 2-3 plane):

$$e_1 = \epsilon_1 - \bar{\epsilon}_1 \quad (\text{A-3a})$$

$$e_2 = \epsilon_2 - \bar{\epsilon}_2 \quad (\text{A-3b})$$

$$e_3 = \epsilon_3 - \bar{\epsilon}_2 \quad (\text{A-3c})$$

$$e_4 = \epsilon_4 \quad (\text{A-3d})$$

$$e_5 = \varepsilon_5 \quad (A-3e)$$

$$e_6 = \varepsilon_6 \quad (A-3f)$$

$$\bar{e}_1 = e_1 + e_2 + e_3 \quad (\text{Dilatation of Deviatoric Strain}) \quad (A-11)$$

$$\bar{e}_1 = K_\varepsilon \bar{\varepsilon}_2 \quad (\text{Non-uniform hydrostatic strain}) \quad (A-7)$$

$$K_\sigma e_1 + e_2 + e_3 = 0 \quad (\text{Assures that deviatoric stress has no hydrostatic component}) \quad (A-9)$$

Finally, the use of the deviatoric constitutive relation, equation (A-6) hinged upon the satisfaction of equation (A-5). Inverting equation (A-5) into compliance form and summing the three equations for normal strain yields upon reduction:

$$\bar{\sigma} = \tilde{K} (\varepsilon_1 + \varepsilon_2 + \varepsilon_3 - \bar{e}) \quad (A-12)$$

where  $\tilde{K}$  is a true material property which will be called the effective bulk modulus of the material (it equals the reciprocal of the sum of the nine normal compliance matrix components), and  $(\varepsilon_1 + \varepsilon_2 + \varepsilon_3)$  is the total volumetric dilatation of the material element. This effective modulus, unlike the bulk modulus, is independent of deviatoric stress in anisotropic materials. The bulk modulus reduces to the effective bulk modulus only when the deviatoric dilatation  $\bar{e}$  equals zero. This condition occurs under either of the following conditions: the material is isotropic, or the loading is purely hydrostatic.

It was mentioned previously that the empirical relation between dilatation and pressure is not a linear one. One advantage of the deviatoric formulation lies in the ability to arbitrarily make the hydrostatic relation non-linear while retaining the linear simplicity of Hooke's Law for the deviatoric portion of the constitutive relation. Though this ad hoc procedure does not theoretically follow as an extension to Hooke's Law, it does permit the code user to more flexibly model the empirical behavior of the material.

There are also codes employing the incremental strain approach which use a formulation employing deviatoric stress, though the formulation can not be termed deviatoric. The form of the relation used by the HELP code<sup>50</sup> is

$$\Delta s_i = \begin{cases} C_{ij} \Delta \epsilon_j - 3K (\Delta \epsilon_1 + \Delta \epsilon_2 + \Delta \epsilon_3) & , i=1,2,3 \\ C_{ij} \Delta \epsilon_j & i=4,5,6 \end{cases} \quad (A-13)$$

where K is identified as the bulk modulus which presumably can be made dependent on dilatation (and therefore hydrostatic stress). In this way, the formulation may also provide the flexibility of a truly deviatoric formulation. However, equation (A-13) is not truly a deviatoric relation, since the deviatoric stress increment is not related to deviatoric strain increment, but rather is expressed in terms of the total strain increment. The system of equations presently proposed, equations (A-6) and (A-12), are thus more attractive in a theoretical sense. Similarly, it has already been pointed out that the bulk modulus (as opposed to the effective bulk modulus derived in equation (A-12)) is functionally dependent on deviatoric stress, and in this sense equation (A-13) will exhibit flawed behavior if the deviatoric variation in bulk modulus is not modeled. Finally, the flexibility afforded in equation (A-13) by allowing the bulk modulus to vary with hydrostatic stress has the disturbing effect that the resulting sum of the normal stress deviators is not generally zero. If this interpretation of the HELP<sup>50</sup> is correct, the use of the term stress deviators to describe the left hand side of equation (A-13) is not even justified.

EPIC<sup>51</sup> use a form similar to equation (A-13) except that K is defined in such a way as to force the sum of the normal stress deviators to zero. This ad hoc procedure will coincidentally mimic the behavior of equation (A-6), though the formulation is in error during the subsequent hydrostatic stress calculation by not accounting for the deviatorically induced dilatation ( $\bar{\epsilon}$ ).

Additional advantages afforded by the proposed formulation when using a code which employs an incremental strain approach, may be seen by comparing the proposed algorithm specifics with that of the prior formulation used in HELP<sup>50</sup>. The proposed formulation takes strain increments, and decomposes them into hydrostatic and deviatoric components. Equation (A-6) is used in an incremental way to update deviatoric stress. If

the hydrostatic strain increments are summed and remembered, equation (A-12) may be used to evaluate the hydrostatic stress value directly. If the hydrostatic stress is a function of volumetric dilatation only, then errors introduced into the calculation of hydrostatic stress are machine precision dependent, but not algorithm dependent. That is to say, errors in the calculation of hydrostatic pressure are insensitive to the size of the hydrostatic strain increment.

On the other hand, an incremental stress formulation like that proposed for HELP<sup>50</sup> experiences errors which are dependent on hydrostatic strain increment size (which is proportional to the calculation timestep size), if variable compressibility is employed. For example, use of equation (A-13) as described for materials with variable compressibility requires that some sort of average compressibility be calculated for the time increment in question. As shown in Figure A-3, the average bulk modulus depends not only on the total element dilatation, but also on the size of the strain increment (since dilatation changes with strain increment). Therefore, the accuracy of such a scheme is limited by the integration step size regardless of machine precision. Presumably, this problem can be avoided if one replaces the modulus dilatation product at the end of equation (A-13) with a  $\Delta\bar{\sigma}$  term, where the  $\Delta\bar{\sigma}$  term is directly obtainable knowing the previous and present cycles' average stress.

However, many non-linear equations of state that are routinely employed in impact codes like HELP<sup>50</sup> show a dependence of hydrostatic pressure on internal energy. Under such conditions, this dependence of pressure on energy must effectively be reflected in equation (A-13) for consistency to be maintained. However, since internal energy is affected by the work done by the internal stresses (which include deviatoric stresses), a coupling of internal energy, pressure, and deviatoric stresses exists. No simple means exists to solve this set of equations simultaneously, and a lengthy iterative process becomes necessary. No mention of such coupling and/or iteration was made<sup>50</sup>. Thus, it can be seen that equation (A-13) suffers many drawbacks which make its use less desirable than the proposed method given by equations (A-6) and (A-12) in which the deviatoric relations are free of hydrostatic terms.

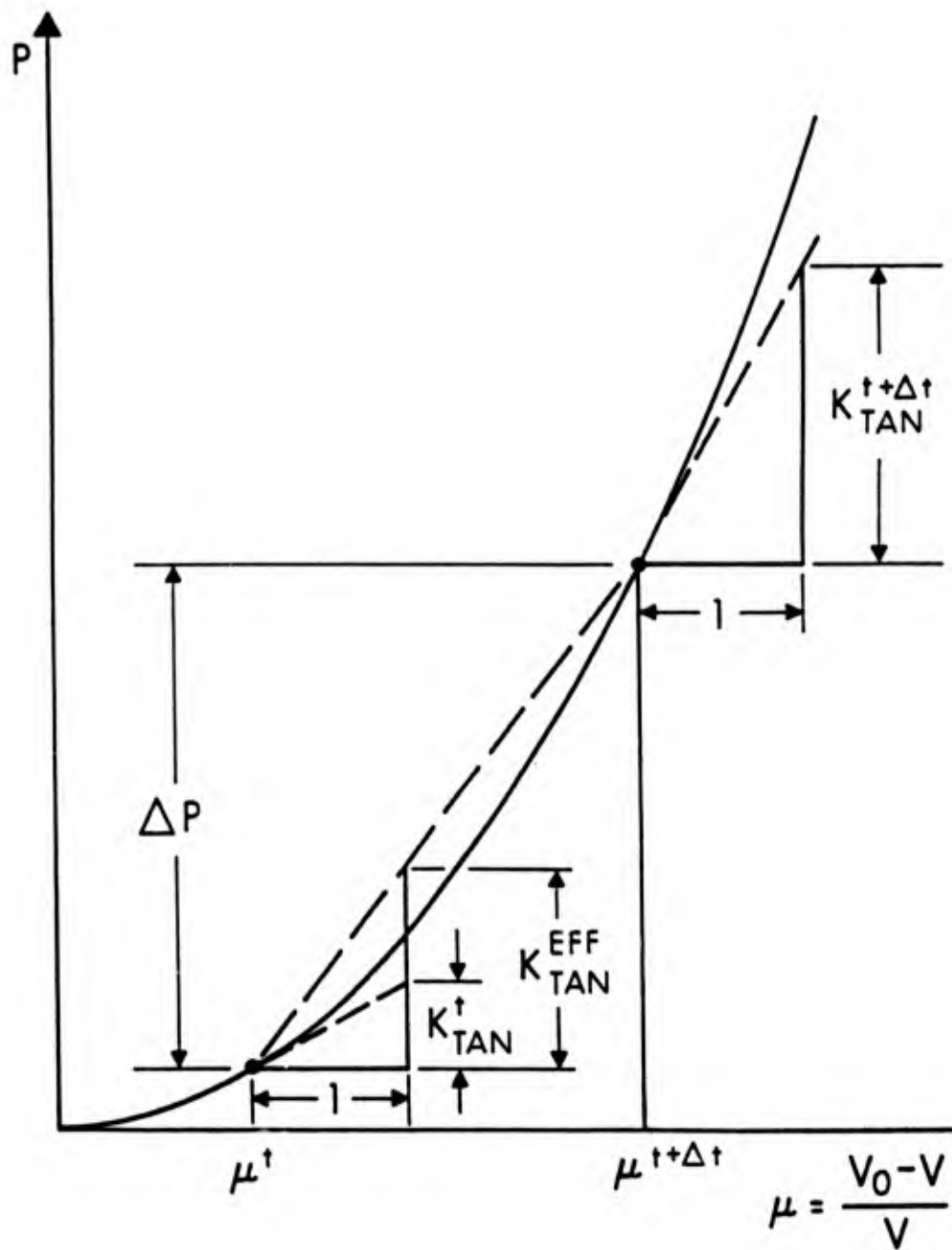


Figure A-3. Error in computation of hydrostatic pressure is introduced if tangent modulus is employed.

In summary, the steps proposed for deducing elastic anisotropic deviators in equations (A-6) and (A-12) follow closely those for isotropic materials in the following ways:

- a. deviatoric stress is expressible totally in terms of deviatoric strain, and
- b. pressure is expressible totally in terms of dilatations.

The differences from the isotropic formulation are:

- a. the matrix relating deviatoric stress to deviatoric strain is not diagonal in the anisotropic case, and
- b. the total volumetric dilatation must be modified by the deviatorically induced dilatation when calculating the pressure.

#### A.4 Plastic Deviatoric Anisotropy.

The anisotropic equivalent to the Prandtl-Reuss flow rule of plasticity can be similarly cast into a deviatoric form. Stress behavior of yielding material is governed primarily by the nature of the yield surface, which defines the allowable stress states of the material and subsequent plastic flow properties. In general, only a portion of a post-elastic strain increment ( $\Delta\epsilon_j^I$ ) contributes to changing the stress. That portion is designated the elastic strain increment ( $\Delta\epsilon_j$ ). The remaining portion of the strain increment is designated the plastic strain increment ( $\Delta\epsilon_j^P$ ). This decomposition of the strain increment is governed by two rules:

- a. an infinitesimal plastic strain increment vector must be normal to the yield surface at the stress state under consideration, and
- b. a stress increment vector tending to go outside of the yield surface can at most move tangentially to the yield surface at the stress state under consideration.

Because of the linearity of the equations governing the conversion from absolute elastic strain ( $\epsilon_j$ ) to deviatoric elastic strain ( $e_j, \bar{e}, \hat{e}_j$ ), one is assured that by decomposing

the elastic strain increment into any two arbitrary divisions, the sum of the two converted strain divisions equals the conversion of the strain division sum. This rule becomes handy for impact code implementation if the two strain divisions are taken as the total strain increment and the negative of the plastic strain increment (the sum of which add up to the elastic strain increment). In this way, the stress changes may be calculated on the assumption that the total stress increment is elastic. If it can then be determined that yield has been violated, a fictitious stress may be calculated from the plastic strain increment, and subtracted from the stress state which is in violation of yield to give the true stress state.

To see how this is employed in actuality, consider the deviatoric constitutive relation, equation (A-6), in which the deviatoric stress increment is calculated via the product of the modulus and elastic deviatoric strain increment. The linearity of the deviatoric conversion equations implies, for plastic deformation, that:

$$\Delta s_i = C_{ij} (\Delta e_j^t - \Delta e_j^p) \quad (A-14)$$

The deviatoric total strain increment ( $\Delta e_j^t$ ) is calculated with the deviatoric conversion equations, based on the total strain increment. The plastic deviatoric strain increment ( $\Delta e_j^p$ ) can be decomposed into its total plastic ( $\Delta e_j^p$ ) and hydrostatic plastic ( $\Delta \bar{e}_j^p$ ) components, respectively.

The total plastic strain component is necessarily normal to the yield surface, and is given by:

$$\Delta e_j^p = \Delta \lambda \frac{\partial f}{\partial \sigma_j} \quad (A-15)$$

where  $f$  is the equation governing the yield surface, and  $\Delta \lambda$  is a proportionality constant for the yield surface normal ( $\partial f / \partial \sigma_j$ ), which has been evaluated at the stress state in question. If one assumes an anisotropic yield condition like Hill's<sup>39</sup> in which the yield criterion is independent of the hydrostatic pressure, then the yield surface normal may be evaluated with the use of the deviatoric stresses (e.g.,  $\partial f / \partial s_j$ ).

Similarly, the hydrostatic plastic component represents the three components of plastic deviatoric dilatation, and can be explicitly calculated knowing the elastic and plastic material constants and the same proportionality constant  $\Delta\lambda$  required above.

As a side note, the usage "plastic dilatation" would seem to imply that plastic incompressibility does not hold. This is, however, not the case. Recall that equations (A-3), (A-7), (A-9), and (A-11) were proven valid only for elastic deformations. The concept of plastic strain was introduced to represent the difference between the elastic and total strain components. This term "plastic dilatation" in fact represents a portion of the total dilatation to be subtracted off to yield the proper value of elastic deviatoric dilatation. The plastic incompressibility relation:

$$\Delta\epsilon_1^P + \Delta\epsilon_2^P + \Delta\epsilon_3^P = 0 \quad (\text{A-16})$$

is still assumed to hold throughout all calculations derived here. Thus, expressing the plastic deviatoric dilatation term as

$$\Delta\bar{\epsilon}_j^P = \frac{d\bar{\epsilon}_j^P}{d\lambda} \Delta\lambda \quad (\text{A-17})$$

the deviatoric constitutive relation may be expressed, using equations (A-14), (A-15), and (A-17) as

$$\Delta s_i = C_{ij} \left( \Delta e_j^t - \left( \frac{\partial f}{\partial s_j} - \frac{d\bar{\epsilon}_j^P}{d\lambda} \right) \Delta\lambda \right) \quad (\text{A-18})$$

Notice that the only term in this relationship which differs from the isotropic case is the last term involving  $(d\bar{\epsilon}_j^P/d\lambda)$ . This term is zero for the isotropic case because of the fact that there is no dilatation as a result of deviatoric stress. Similarly, this term can not generally be zero for the anisotropic case because equation (A-18) is a deviatoric stress relationship. The term  $(d\bar{\epsilon}_j^P/d\lambda)$  is precisely the magnitude required to force the deviator stress to remain in the  $\pi$  plane (i.e., have no hydrostatic components).

The quantity  $\Delta\lambda$  may be evaluated by taking the scalar product of equation (A-18) with  $(\partial f/\partial s_j)$ . Because  $\Delta s_j$  is tangential to the yield surface and  $(\partial f/\partial s_j)$  is the yield surface

normal, the scalar product is zero. Similarly the term  $(d\bar{\epsilon}_j^P/d\lambda)$  is of a form identical to that resulting from the purely hydrostatic stress state described in equation (A-7). Thus, the quantity  $C_{ij}(d\bar{\epsilon}_j^P/d\lambda)$  is parallel with the hydrostat vector. If one assumes an anisotropic yield condition like Hill's<sup>39</sup> in which the yield criterion is independent of the hydrostatic pressure, the scalar product of  $C_{ij}(d\bar{\epsilon}_j^P/d\lambda)$  and  $(\partial f/\partial s_i)$  is also zero. Thus the value for  $\Delta\lambda$  may be calculated as:

$$\Delta\lambda = \frac{\frac{\partial f}{\partial s_i} C_{ij} \Delta e_j^t}{\frac{\partial f}{\partial s_i} C_{ij} \frac{\partial f}{\partial s_j}} \quad (\text{A-19})$$

This expression for  $\Delta\lambda$  is of a form identical to that obtained for the isotropic case, and can be used in equation (A-18) to calculate the elastic deviatoric stress increment.

Because of the curvature of the yield surface and the fact that  $\Delta\lambda$  was calculated for the stress state existing at the beginning of the time cycle, the updated stress state resulting from equation (A-18) may in fact still lie slightly outside the yield surface. What is done at this point in both the existing models and the proposed one is to scale back all the stress components uniformly until the yield surface is exactly reached. Though this technique introduces some error on its own, it is believed that the error is not too great since the components of the increment of stress scale back are nearly normal to the yield surface in many cases. Also, ways have been devised by Vavrick and Johnson<sup>51</sup> to decrease the magnitude of this error. Their techniques employ subdivision of the time cycle. However, some anisotropic formulations use a deviatoric stress formulation in which elastic deviatoric stresses are defined in the following way<sup>50</sup>

$$\Delta s_i = \begin{cases} C_{ij} \Delta \epsilon_j - 3K (\Delta \epsilon_1 + \Delta \epsilon_2 + \Delta \epsilon_3), & i=1,2,3 \\ C_{ij} \Delta \epsilon_j, & i=4,5,6 \end{cases} \quad (\text{A-13})$$

and additional error is introduced as a result. This occurs because the formulation in equation (A-13) does not guarantee that the sum of the deviatoric stresses will equal zero for an anisotropic material, and in fact they will generally not do so. As a result, any scale back of the stresses employed to meet the yield criterion will include a hydrostatic

component. Such hydrostatic scale back violates basic rules of yield surface normality in a fundamental way. Furthermore, techniques proposed by Vavrick and Johnson which decrease the error resulting from stress scale-back will not decrease the amount of hydrostatic stress error introduced into the calculation as the result of using a formulation like that of equation (A-13).

#### A.5 Summary.

An anisotropic formulation has been proposed which satisfies the condition of reducing to Hooke's Law/Prandtl Reuss Flow Rule when employing the constraint of constant compressibility and isotropy, but which conveniently allows for anisotropic material properties and variable compressibility.

The deviatoric stress technique which has been used routinely in the isotropic impact codes for describing isotropic behavior has been effectively combined with the anisotropic constitutive relations to produce a truly deviatoric anisotropic constitutive relation. In this deviatoric formulation, deviatoric stress is expressed only in terms of deviatoric strain, and compressibility does not influence the deviatoric relation.

Existing formulations suffer from drawbacks which have been eliminated in the present formulation. Some of the drawbacks of previous formulations may be enumerated as follows:

- a. working with absolute stress and strain offers no simple way to perform calculations involving variable compressibility,
- b. calculating hydrostatic pressure increments (instead of complete hydrostatic pressure) can introduce error associated with obtaining and averaging the tangent bulk modulus over a strain increment (this problem compounded by the fact that Hugoniot data is usually gathered in the form pressure versus dilatation, the slope of which is the tangent bulk modulus), and
- c. use of a "deviatoric" stress which includes a hydrostatic component will produce error in the pressure calculation if stresses are scaled back to satisfy the yield condition.

Additionally, the formulation can be simply coded into existing impact codes which presently use the deviatoric stress technique for isotropic materials. Finally, it is hoped that the formulation provides an enhanced physical interpretation on the behavior of anisotropic materials.

INTENTIONALLY LEFT BLANK.

APPENDIX B:

ANISOTROPY DIRECTION TRACKING FOR  
AXISYMMETRIC SIMULATIONS

INTENTIONALLY LEFT BLANK.

## APPENDIX B:

### ANISOTROPY DIRECTION TRACKING FOR AXISYMMETRIC SIMULATIONS

In order to model anisotropy for axisymmetric code simulations, one must have the ability to accurately track element motion in the  $\theta$  direction. In particular, one must ascertain the orientation of anisotropy in the  $r$ - $z$  plane, as well as the angle formed between the principal direction of anisotropy and the  $r$ - $z$  plane.

One of the first problems to be considered is the shape of a computational element which has experienced motion in the  $\theta$  direction. The data available are the  $r$ ,  $z$ , and  $\theta$  coordinates for the three nodes at the vertices of the element. A logical choice for an interpolation function for the  $\theta$  position throughout the element, which is consistent with the  $r$  and  $z$  interpolations is

$$\theta = \alpha r + \beta z + \gamma \quad , \quad (B-1)$$

where  $\alpha$ ,  $\beta$ , and  $\gamma$  are constants chosen in such a way that  $\theta$ , evaluated at each of the nodal vertices, matches that node's coordinate. One of the favorable results of choosing an interpolation function like equation (B-1) is that the element, when plotted in a Cartesian  $r$ ,  $z$ ,  $\theta$  space (Figure B-1) is still flat. However, interpolation function (B-1) suffers drawbacks. In particular, the surface of the element in cylindrical  $r$ - $z$ - $\theta$  space is curved in such a way that the angle ( $\phi$ ) formed between the element surface at a point and the  $r$ - $z$  plane through that point varies for the different points in the element. Figure B-2 depicts this behavior schematically where, for simplicity of illustration, projection into the  $r$ - $\theta$  plane has been performed. As such, the term  $\phi^r$  has been employed to represent the angle  $\phi$  as projected into the  $r$ - $\theta$  plane.

On the other hand, the curved element proposed is much more desirable than say, a flat element in cylindrical  $r$ - $z$ - $\theta$  space. Only when one admits the possibility of having a curved element can one consider the more realistic situation of having a deformed element curve around the axis of symmetry. As was noted however, in Figure B-2, the angle ( $\phi$ ) formed between the deformed element and the  $r$ - $z$  plane varies slightly at different points in

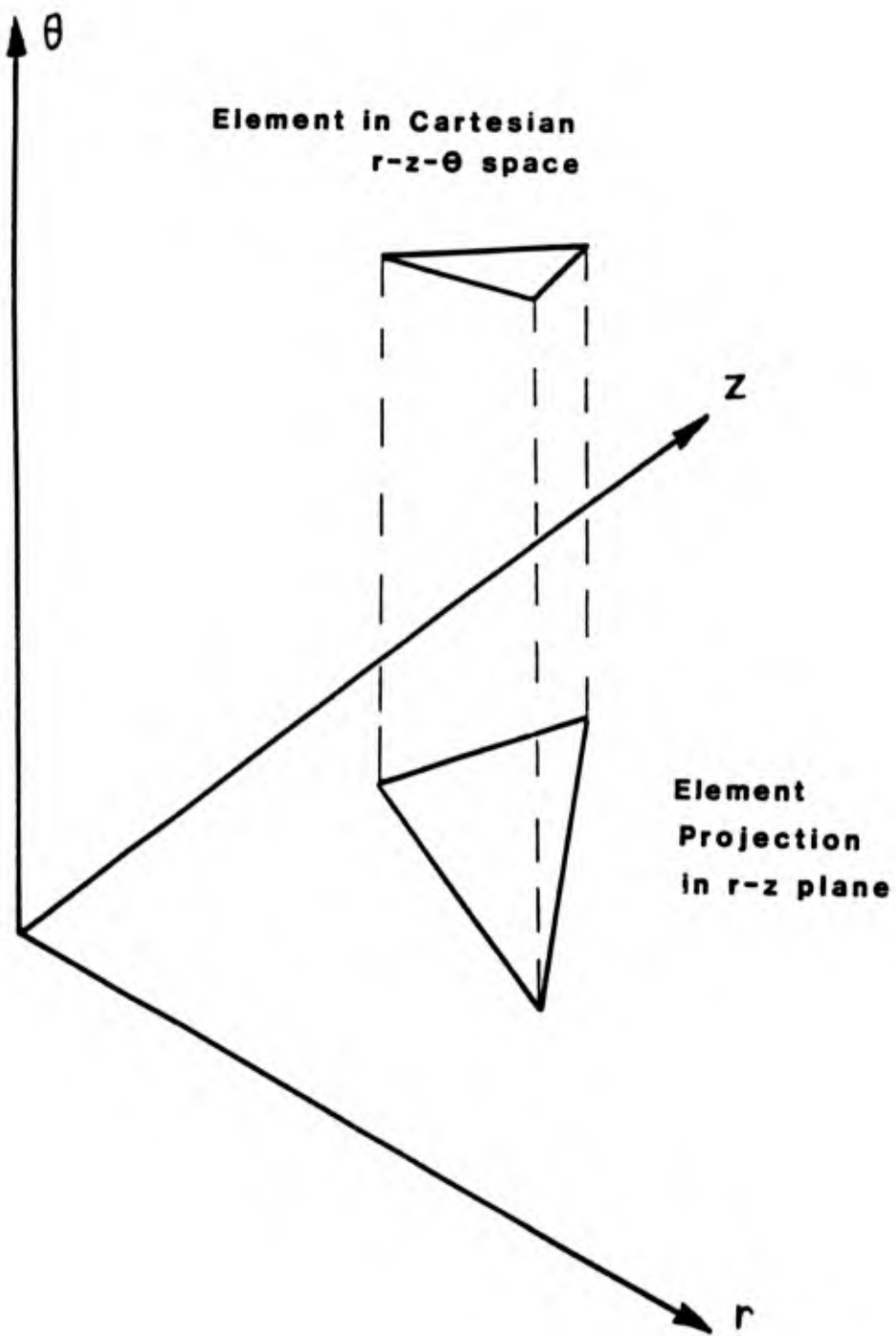
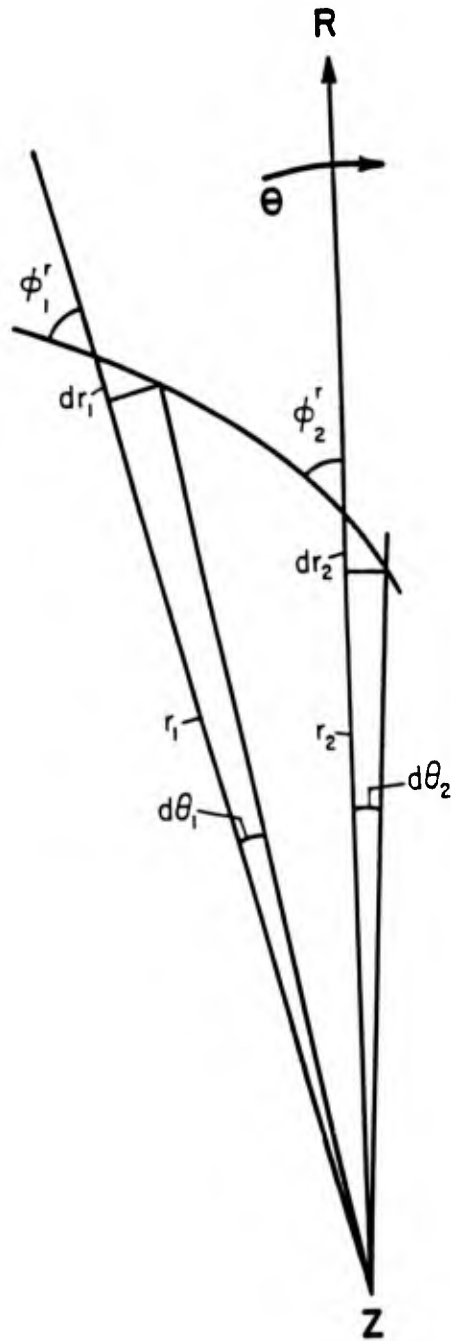


Figure B-1. Interpolation for  $\theta$  within a computational element is flat in Cartesian  $r$ - $z$ - $\theta$  space.



$$\theta = \alpha r + \beta z + \gamma$$

$$\frac{d\theta}{dr} = \alpha = \text{constant}$$

$$\frac{d\theta_1}{dr_1} = \frac{d\theta_2}{dr_2} = \frac{d\theta}{dr} = \alpha$$

$$\phi_1^r = \phi_2^r$$

$$\tan \phi_1^r = r_1 \frac{d\theta}{dr}$$

$$\tan \phi_2^r = r_2 \frac{d\theta}{dr}$$

Figure B-2. Schematic depiction of how interpolation function for  $\theta$  causes the angle between r-z plane and computational element ( $\phi^r$ ) to vary throughout element, as viewed down the z axis in cylindrical r-z- $\theta$  space.

the element. A reasonable average for this angle may be obtained by evaluating the angle at the centroid of the element.

The actual situation of anisotropy modeling is further complicated by two issues:

a. there exists a particular line in the r-z plane, which represents the projection of the principal direction of anisotropy onto the r-z plane; and

b. at time zero, when an element's geometry is undeformed, there may exist a non-zero angle between the principal direction of anisotropy and the r-z plane.

The orientation of principal direction, as projected into the r-z plane (item 1 above), can be easily tracked by integrating the element's r-z rotation rate. This rotation rate is readily available from standard axisymmetric hydrocode computations. It was shown in Figure B-1 how a deformed element remains flat in the Cartesian r-z- $\theta$  space. For the anisotropic problem at hand, one must be able to determine the angle ( $\phi$ ) formed between this deformed element and the r-z plane, along a particular direction. In Figure B-3, this direction is shown as a vector dl which forms an angle  $\delta$  with respect to the r axis, and lies in the r-z plane. To determine  $d\theta/dl$ , one employs directional derivatives  $\partial\theta/\partial r$  and  $\partial\theta/\partial z$  so that

$$\frac{d\theta}{dl} = \frac{\partial\theta}{\partial r} \frac{\partial r}{\partial l} + \frac{\partial\theta}{\partial z} \frac{\partial z}{\partial l} \quad (B-2)$$

Recalling equation (B-1), and substituting into equation (B-2), it is seen that  $d\theta/dl$  may be expressed as

$$\frac{d\theta}{dl} = \alpha \cos \delta + \beta \sin \delta \quad (B-3)$$

The parameters  $\alpha$  and  $\beta$  are easily determinable from vector analysis. If the quantity  $V_{12} \times V_{13}$  takes on the value

$$V_{12} \times V_{13} = a \hat{i} + b \hat{j} + c \hat{k} \quad (B-4)$$

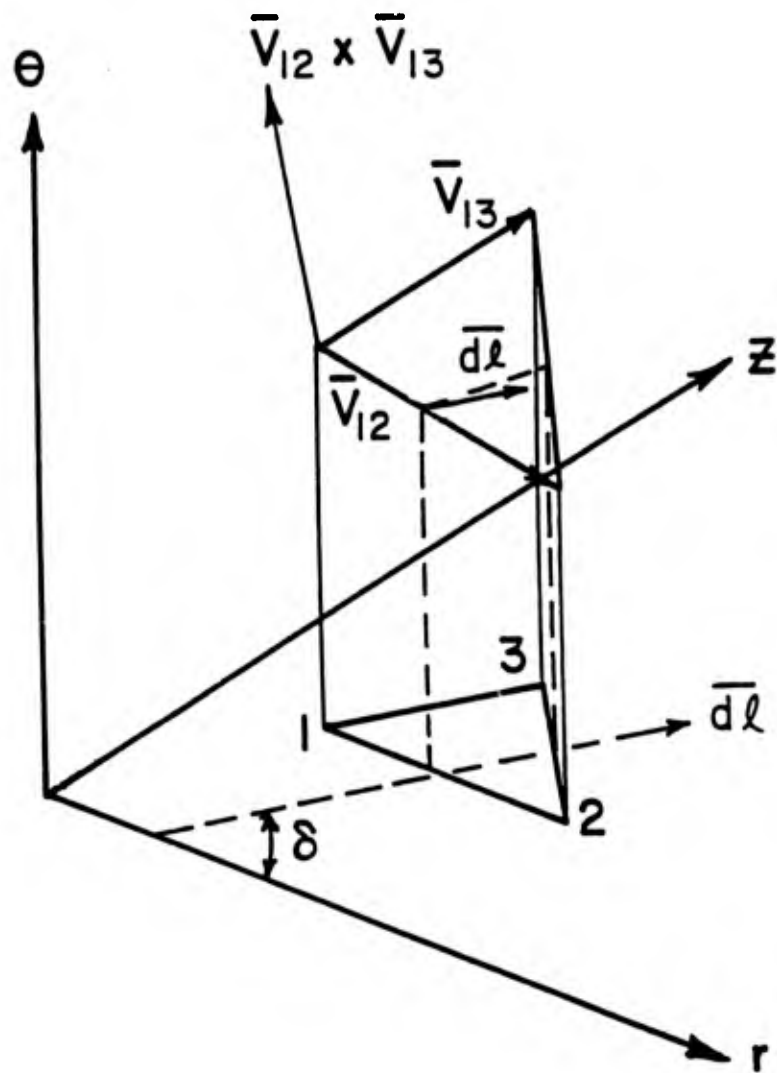


Figure B-3. Computational element viewed in Cartesian r-z-θ space, showing all quantities needed to compute  $d\theta/dl$ , and hence the angle between the r-z plane and deformed element in cylindrical r-z-θ space ( $\phi$ ).

then it can be shown that  $\alpha = -a/c$  and  $\beta = -b/c$ . Thus, the angle ( $\phi$ ) formed between the element and the r-z plane along the direction dl is given by

$$\tan \phi = r \frac{d\theta}{dl} \quad (B-5)$$

This result is similar to that derived in Figure B-2, except that it accounts for arbitrary directions of anisotropy, and does not assume that dl is aligned with the radial axis.

The final point to be considered is the situation where the principal direction of anisotropy does not lie in the plane of the element (item 2 above). Even if the element does not experience deformation in the  $\theta$  direction, it is clear that the out of plane angle  $\phi$  may vary with r and z distortion. In particular, an element in the r-z plane stretched infinitely large will have  $\phi$  approach zero, while an element being compressed to infinitesimal proportions will have  $\phi$  approach  $\pi/2$ . The way that this situation may be addressed computationally is to (within an element) augment the nodes  $\theta$  coordinates by a fictitious amount only for the purposes of computing  $\phi$ . This fictitious augmentation will be computed in such a fashion as to guarantee that the initial value  $\phi$  takes on is the desired initial value for  $\phi$ . In the absence of this augmentation, the initial value for  $\phi$  would otherwise be zero identically. These augmentation values are computed once at the commencement of computation for each element, and are used throughout the numerical computation.

It has thus been shown that the necessity of tracking anisotropy orientation in axisymmetric elements may be accomplished in a straight forward manner. The tracking is done on two parameters. First, the projection of anisotropy direction on the r-z plane is tracked via r-z element rotation. Secondly, the angle ( $\phi$ ) formed between the principal direction of anisotropy and the r-z plane is tracked. The employment of this type of anisotropy tracking permits the effective modeling of anisotropic materials in axisymmetric codes in such a way as to permit anisotropy induced accelerations in the  $\theta$  direction of the cylindrical coordinate system.

## LIST OF SYMBOLS

- ( )' a primed variable is a quantity whose value is taken in an arbitrary laboratory reference frame. The same quantities, when unprimed, are those taken in the "material coordinate frame", unless otherwise noted.
- ( )<sup>t</sup> a superscript t denotes that a variable (e.g., strain) represents a total quantity, which is composed of an elastic part and a plastic part.
- ( )<sup>p</sup> a superscript p denotes that a variable (e.g., strain) represents a plastic quantity.
- ( $\dot{\quad}$ ) a dotted quantity represent time differentiation.
- $\Delta( )$  a upper case delta before a quantity signifies that the quantity is an increment.
- $\delta( )$  a lower case delta before a quantity signifies that the quantity is an increment.
- $A_{ij}$  the matrix which, when multiplied by the contracted stress vector, produces the yield surface normal in the material reference frame.
- $A_{ij}'$  the matrix which, when multiplied by the contracted stress vector, produces the yield surface normal in the laboratory reference frame.
- $\tilde{A}_{ij}$  the difference between  $A_{ij}'$  and  $A_{ij}$ .
- a major axis half-length of anisotropic yield ellipse, or alternately linear acceleration.
- $\alpha$  liner half angle, or alternately an interpolation constant.
- b minor axis half-length of anisotropic yield ellipse.
- $\beta$  an interpolation constant.

- $C_{ij}$  modulus matrix (6x6) which relates stress increments  $d\sigma_i$  to elastic strain increments  $d\varepsilon_j$ .
- D shaped charge diameter.
- $\delta$  thickness of cone or liner element, or alternately the angle formed between the r axis and the projection of a principal material direction onto the r-z plane.
- $\delta m$  mass of a liner element or jet segment.
- $E_i$  Young's modulus in direction i.
- $e_j$  deviatoric elastic strain components (6 independent). In this report, the term "deviatoric" will imply a deviation from the strain state resulting from a condition of hydrostatic pressure. For anisotropic materials, strain is not uniform under conditions of hydrostatic pressure (i.e. the three principal components of strain are not identical). As a result, the normal deviatoric strain components are NOT simply the difference between the total strain component and the average of the normal strain components.
- $\bar{e}$  deviatoric dilatation ( $e_1+e_2+e_3$ ). Though dilatation is only a function of pressure for isotropic materials, dilatation may vary in an anisotropic material just by varying the deviatoric stress (without changing the pressure). Thus, this dilatation associated with the deviatoric stress is referred to as deviatoric dilatation.
- $\varepsilon_j$  elastic strain components in contracted notation; indices 1 to 3 are normal components, whereas 4 to 6 are the shear components 23, 13, and 12 respectively.
- $\bar{\varepsilon}_j$  strain state resulting from hydrostatic pressure. For an isotropic material, the three normal "hydrostatic" strains would be equal. This is not the case for anisotropic material.

- $\epsilon_t$  normal strain in the thickness direction of a rotary forged tensile specimen.
- $\epsilon_w$  normal strain across the width of a rotary forged tensile specimen.
- F coefficient of Hill's yield criterion.
- f the plastic potential (i.e., yield function) or alternately, the fraction of liner element mass which ends up in a jet segment.
- $\partial f / \partial \sigma_j$  the vector normal to the yield surface given by the function f.
- $\partial f / \partial s_j$  is equivalent to  $\partial f / \partial \sigma_j$  for a yield criterion like the Von Mises or Hill, where yielding is not a function of hydrostatic pressure.
- $\phi$  the angle formed between a distorted computational element and the r-z plane.
- $\phi'$  the angle formed between a distorted computational element and the r-z plane, as seen viewing down the z axis.
- G coefficient of Hill's yield criterion.
- $G_{ij}$  Shear modulus in i-j plane.
- $\Gamma$  the CCW angle of rotation about one of the laboratory axes, from the laboratory coordinate system to the preferred material coordinate system.
- $\gamma$  an interpolation constant.
- $\gamma_{ij}$  component of engineering shear strain, equal to twice the tensorial component  $\epsilon_{ij}$ .
- H coefficient of Hill's yield criterion.

- I polar moment of inertia.
- $K_\epsilon$  a parameter which represents the ratio of longitudinal to transverse strain (in the material reference frame) under conditions of hydrostatic pressure ( $\sigma_1 = \sigma_2 = \sigma_3$ ).
- $K_\sigma$  a parameter which represents the ratio of longitudinal to transverse stress (in the material reference frame) under conditions of uniform strain ( $\epsilon_1 = \epsilon_2 = \epsilon_3$ ).
- k strength of a material in simple shear.
- L coefficient of Hill's yield criterion, or alternately the length of a shaped charge cone.
- $l_1$  length of anisotropic yield ellipse along the 1 direction.
- $l_2$  length of anisotropic yield ellipse along the 2 direction.
- $l_3$  length of anisotropic yield ellipse along the 3 direction.
- dl the vector in the direction of the projection of a principal material axis onto the r-z plane.
- $\Delta\lambda$  a proportionality constant between the yield surface normal vector, and the total plastic strain increment vector, which are parallel.
- M coefficient of Hill's yield criterion, or alternately the mass of a cylinder slice.
- m fractional mass of a cylinder slice, or alternately the cosine of an angle in question.
- N coefficient of Hill's yield criterion.
- n the sine of an angle in question.

- $n$  outward normal vector to the anisotropic yield ellipse.
- $\nu_{ij}$  Poisson's ratio in i-j plane.
- $O( )$  Signifies the order of magnitude of the quantity in parentheses.
- $P$  angular momentum.
- $Q_1$  a term comprised of Hill's yield constants, equal to N-2H-G.
- $Q_2$  a term comprised of Hill's yield constants, equal to N-2H-F.
- $Q_3$  a term comprised of Hill's yield constants, equal to M-L.
- $R$  Initial radius of a liner element.
- $r$  radial coordinate in cylindrical r-z- $\theta$  space, or alternately the so called "r-value" of anisotropic material.
- $r_j$  radius of jet segment.
- $\rho$  density.
- $s_i$  deviatoric elastic stress components (6 independent). In this report, the term "deviatoric" will imply a deviation from the stress state resulting from a condition of hydrostatic pressure.
- $\sigma$  standard deviation.
- $\sigma_i$  stress components in contracted notation; indices 1 to 3 are normal components, whereas 4 to 6 are the shear components 23, 13, and 12 respectively.

$\frac{\sigma}{i}$	average stress, by definition equal to the negative of the hydrostatic pressure.
$\sigma_{\theta}$	normal hoop stress component.
T	torque.
$T_{ij}$	The transformation matrix which converts stress and strain from one coordinate system to another.
$T_o$	initial value of torque.
t	time, or alternately tensile specimen thickness.
$t_o$	original tensile specimen thickness.
$\tau_{r\theta}$	shear stress component in the r- $\theta$ plane.
$\tau_{z\theta}$	shear stress component in the z- $\theta$ plane.
$V_j$	axial jet particle velocity.
$V_o$	initial circumferential velocity component of a liner element.
$V_{ij}$	the vector connecting node i of a computational element to node j of the same element, where i, j, and k may take on the values 1, 2, and 3.
w	tensile specimen width.
$w_o$	original tensile specimen width.
$\Omega$	shaped charge spin rate.

$\Omega$	angular velocity of liner element at initial radius R (prior to collapse), as a result of residual stress relief mode 2.
$\omega$	angular velocity of a jet particle, or of the collapsing liner element which forms the jet particle.
$\omega_{net}$	momentum averaged angular velocity through a certain percentage of a collapsing anisotropic cylinder slice.
$\omega_s$	angular velocity of the slug, which results from shaped-charge liner collapse.
$\Delta\xi$	length of a jet segment, originating from a liner element of length $\Delta z$ .
$Y_{1,2,3}$	normal flow stress in material directions 1, 2, and 3, respectively. For an elastic-perfectly plastic material, it equals the yield strength.
$Y_{4,5,6}$	shear flow stress in the 23, 13, and 12 planes, respectively. For an elastic-perfectly plastic material, it equals the yield strength.
$Y_{skew}$	normal flow stress for rotary forged tensile tab oriented 45 degrees from both the circumferential and radial directions.
$\theta$	circumferential coordinate in cylindrical r-z- $\theta$ space.
$z$	axial coordinate in cylindrical r-z- $\theta$ space.
$\Delta z$	axial length of a liner element.

INTENTIONALLY LEFT BLANK.

No of Copies	<u>Organization</u>	No of Copies	<u>Organization</u>
(Unclass., unlimited) 12	Administrator	1	Commander
(Unclass., limited) 2	Defense Technical Info Center		US Army Missile Command
(Classified) 2	ATTN: DTIC-DDA Cameron Station Alexandria, VA 22304-6145		ATTN: AMSMI-RD-CS-R (DOC) Redstone Arsenal, AL 35898-5010
1	HQDA (SARD-TR) WASH DC 20310-0001	1	Commander US Army Tank-Automotive Command ATTN: AMSTA-TSL (Technical Library) Warren, MI 48397-5000
1	Commander US Army Materiel Command ATTN: AMCDRA-ST 5001 Eisenhower Avenue Alexandria, VA 22333-0001	1	Director US Army TRADOC Analysis Command ATTN: ATAA-SL White Sands Missile Range, NM 88002-5502
1	Commander US Army Laboratory Command ATTN: AMSLC-DL Adelphi, MD 20783-1145	(Class. only) 1	Commandant US Army Infantry School ATTN: ATSH-CD (Security Mgr.) Fort Benning, GA 31905-5660
2	Commander Armament RD&E Center US Army AMCCOM ATTN: SMCAR-MSI Picatinny Arsenal, NJ 07806-5000	(Unclass. only) 1	Commandant US Army Infantry School ATTN: ATSH-CD-CSO-OR Fort Benning, GA 31905-5660
2	Commander Armament RD&E Center US Army AMCCOM ATTN: SMCAR-TDC Picatinny Arsenal, NJ 07806-5000	1	Air Force Armament Laboratory ATTN: AFATL/DLODL Eglin AFB, FL 32542-5000
1	Director Benet Weapons Laboratory Armament RD&E Center US Army AMCCOM ATTN: SMCAR-CCB-TL Watervliet, NY 12189-4050		<u>Aberdeen Proving Ground</u> Dir, USAMSAA ATTN: AMXSY-D AMXSY-MP, H. Cohen Cdr, USATECOM ATTN: AMSTE-TO-F Cdr, CRDEC, AMCCOM ATTN: SMCCR-RSP-A SMCCR-MU SMCCR-MSI
1	Commander US Army Armament, Munitions and Chemical Command ATTN: SMCAR-ESP-L Rock Island, IL 61299-5000		Dir, VLAMO ATTN: AMSLC-VL-D
1	Commander US Army Aviation Systems Command ATTN: AMSAV-DACL 4300 Goodfellow Blvd. St. Louis, MO 63120-1798		
1	Director US Army Aviation Research and Technology Activity Ames Research Center Moffett Field, CA 94035-1099		

<u>No. of Copies</u>	<u>Organization</u>	<u>No. of Copies</u>	<u>Organization</u>
2	Director DARPA ATTN: J. Richardson Maj. R. Lundberg 1400 Wilson Blvd. Arlington, VA 22209-2308	2	Naval Weapons Support Center ATTN: John D. Barber Sung Y. Kim Code 2024 Crane, IN 47522-5020
1	Defense Nuclear Agency ATTN: Maj. James Lyon 6801 Telegraph Rd. Alexandria, VA 22192	6	Naval Surface Warfare Center ATTN: Charles R. Garnett (Code G-22) Linda F. Williams (Code G-33) Joseph C. Monolo (Code G-34) Larry Crabtree (Code G-34) Janet Vena (Code G-34) Mary Jane Sill (Code H-11) Dahlgren, VA 22448-5000
1	US Army Strategic Defense Command ATTN: CSSD-H-LL (Tim Cowles) Huntsville, AL 35807-3801	15	Naval Surface Warfare Center ATTN: Pao C. Huang (G-402) Bryan A. Baudler (R-12) Robert H. Moffett (R-12) Robert Garrett (R-12) Thomas L. Jungling (R-32) Philip Marshall (U-11) Windsor Furr (U-11) Daniel Harris (U-11) Amos A. Dare (U-12) Richard Caminity (U-43) John P. Matra Paula Walter Lisa Mensi Kenneth Kiddy F.J. Zerilli 10901 New Hampshire Ave. Silver Spring, MD 20903-5000
1	USA ARMC ATTN: ATSB-CD (Dale Stewart) Ft. Knox, KY 40121	1	Naval Civil Engr. Lab. ATTN: Joel Young (Code L-56) Port Huene, CA 93043
1	US Army MICOM ATTN: AMSMI-RD-TE-F (Matt H. Triplett) Redstone Arsenal, AL 35898-5250	4	Air Force Armament Lab. ATTN: AFATL/DLJW (W. Cook) AFATL/DLJW (M. Nixon) AFATL/MNW (Lt. Donald Lorey) AFATL/MNW (Richard D. Guba) Eglin AFB, FL 32542
2	TACOM RD&E Center ATTN: AMCPM-ABMS-SA (John Rowe) AMSTA-RSS (K.D. Bishnoi) Warren, MI 48397-5000	2	MSD/ENL ATTN: W. Dyess I. Talbot Eglin, AFB 32542-5000
2	Commander Armament RD&E Center US Army AMCCOM ATTN: SMCAR-CCH-V (M.D. Nicolich) SMCAR-FSA-E (W.P. Dunn) Picatinny Arsenal, NJ 07806-5000	1	3246 Test Wing/TZFT ATTN: Cpt. Mark Olson Eglin AFB, FL 32542-5000
4	US Army Belvoir RD&E Center ATTN: STRBE-NAE (Bryan Westlich) STRBE-JMC (Terilee Hanshaw) STRBE-NAN (Steven G. Bishop) STRBE-NAN (Josh Williams) Ft. Belvoir, VA 22060-5166		
1	USMC/MCRDAC/PM Grounds Wpns. Br. ATTN: Dan Haywood Firepower Div. Quantico, VA 22134		
3	Naval Weapons Center ATTN: Tucker T. Yee (Code 3263) Don Thompson (Code 3268) W.J. McCarter (Code 6214) China Lake, CA 93555		

<u>No. of Copies</u>	<u>Organization</u>	<u>No. of Copies</u>	<u>Organization</u>
8	Sandia National Laboratory ATTN: Robert O. Nellums (Div. 9122) Jim Hickerson (Div. 9122) Marlin Kipp (Div. 1533) Allen Robinson Div. 1533) Wm. J. Andrzejewski (Div. 2512) Don Marchi (Div. 2512) R. Graham (Div. 1551) R. Lafarge (Div. 1551) P.O. Box 5800 Albuquerque, NM 87185	2	Explosive Technology ATTN: James Kennedy Michael L. Knaebel P.O. Box KK Fairfield, CA 94533
10	Director Los Alamos National Laboratory ATTN: G.E. Cort (MS K574) Tony Rollett (MS K574) Mike Burkett (MS K574) Robert Karpp (MS P940) Rudy Henninger (MS K557, N-6) Robert M. Gates (MS K574) Roy Greiner (MS-G740) James P. Ritchie (B214, T-14) John Bolstad (MS G787) Bill Harvey P.O. Box 1663 Los Alamos, NM 87545	2	Rockwell Missile Systems Div. ATTN: Terry Neuhart Dennis Kaisand 1800 Satellite Blvd. Duluth, GA 30136
13	Lawrence Livermore National Laboratories ATTN: Barry R. Bowman (L-122) Ward Dixon (L-122) Raymond Pierce (L-122) Russell Rosinsky (L-122) Owen J. Alford (L-122) Diana Stewart (L-122) Tony Vidlak (L-122) Albert Holt (L-290) John E. Reaugh (L-290) David Wood (L-352) Robert M. Kuklo (L-874) Thomas McAbee (MS 35) Michael J. Murphy P.O. Box 808 Livermore, CA 94550	1	Rockwell Intl./Rocketydyne Div. ATTN: James Moldenhauer 6633 Canoga Ave (HB 23) Canoga Park, CA 91303
1	Battelle Northwest ATTN: John B. Brown, Jr. MSIN 3 K5-22 P.O. Box 999 Richland, WA 99352	1	IIT Research Institute ATTN: Gerard Koller 10 W. 35th St. Chicago, IL 60616
1	Advanced Technology, Inc. ATTN: John Adams P.O. Box 125 Dahlgren, VA 22448-0125	1	Allied Signal ATTN: L. Lin P.O. Box 31 Petersburg, VA 23804
		2	McDonnell-Douglas Helicopter ATTN: Loren R. Bird Lawrence A. Mason 5000 E. McDowell Rd. (MS 543-D216) Mesa, AZ 85205
		1	University of Colorado Campus Box 431 (NNT 3-41) ATTN: Timothy Maclay Boulder, CO 80309
		1	New Mexico Inst. Mining & Tech. Campus Station (TERA Group) ATTN: David J. Chavez Socorro, NM 87801
		2	Schlumberger Perforating & Test ATTN: Manuel T. Gonzalez Dan Markel P.O. Box 1590/14910 Ariline Rd. Rosharon, TX 77583-1590
		2	Aerojet Ordnance/Exp. Tech. Ctr. ATTN: Patrick Wolf Gregg Padgett 1100 Bulloch Blvd. Socorro, NM 87801

<u>No. of Copies</u>	<u>Organization</u>	<u>No. of Copies</u>	<u>Organizaion</u>
1	Aerojet Precision Weapons Dept. 5131/T-W ATTN: Robert S. Kowell 1100 Hollyvale Azusa, CA 91702	2	Dyna East Corporation ATTN: P.C. Chou R. Ciccarelli 3201 Arch St. Philadelphia, PA 19104
1	Aerojet Ordnance Corporation ATTN: J. Carleone 2521 Michelle Drive Tustin, CA 92680	2	Southwest Research Institute ATTN: C. Anderson A. Wenzel 6220 Culebra Road P.O. Drawer 28510 San Antonio, TX 78284
1	Babcock & Wilcox ATTN: Ken Camplin P.O. Box 11165 Lynchburg, VA 24506	2	Battelle - Columbus Laboratories ATTN: R. Jameson S. Golaski 505 King Avenue Columbus, OH 43201
2	Physics International ATTN: Ron Funston Lamont Garnett 2700 Merced St./P.O. Box 5010 San Leandro, CA 94577	3	Honeywell, Inc. ATTN: Gordon R. Johnson Tim Holmquist Kuo Chang MN 48-2700 7225 Northland Dr. Brooklyn Park, MN 55428
1	Sparta ATTN: Tony Hill 5401 East La Palma Ave. Anaheim, CA 92807	1	AAI Corp. ATTN: Richard Huffman Dept. 403/Bldg. 100 Hunt Valley, MD 21030
2	Lockheed Missile & Space Co., Inc. ATTN: S. Kusumi (O-81-11, Bldg. 157) Jack Philips (O-54-50) P.O. Box 3504 Sunnyvale, CA 94088	5	LTV Missiles & Electronics Group ATTN: Gary Hough (WT-50) G.L. Jackson (WT-71) M.M. Tower (WT-78) Ken Havens (EM-36) R.J. Taylor (EM-36) P.O. Box 65003 Dallas, TX 75265-0003
1	Lockheed Missile & Space Co., Inc. ATTN: Richard A. Hoffman Santa Cruz Fac./Empire Grade Rd. Santa Cruz, CA 95060	2	General Research Corp. ATTN: Alex Charters Tom Menna 5383 Hollister Ave. Santa Barbara, CA 93160-6770
1	Boeing Corporation ATTN: Thomas M. Murray (MS 84-84) P.O. Box 3999 Seattle, WA 98124	1	General Dynamics ATTN: Jaime Cuadros P.O. Box 50-800 Mail Zone 601-87 Ontario, CA 91761-1085
2	Mason & Hanger - Silas Mason Co. ATTN: Thomas J. Rowan Christopher Vogt Iowa Army Ammunition Plant Middletown, IA 52638-9701	1	Systems, Science and Software, Inc. ATTN: R. Sedgwick 3398 Carmel Mountain Rd. San Diego, CA 92121
1	Nuclear Metals Inc. ATTN: Jeff Schreiber 2229 Main St. Concord, MA 01742		

<u>No. of Copies</u>	<u>Organization</u>
2	California Research & Tech. Corp. ATTN: Roland Franzen Dennis Orphal 5117 Johnson Dr. Pleasanton, CA 94566
2	Orlando Technology, Inc. ATTN: Dan Matuska J. Osborn P.O. Box 855 Shalimar, FL 32579
3	Kaman Sciences Corporation ATTN: D. Barnette D. Elder P. Russell P.O. Box 7463 Colorado Springs, CO 80933

<u>No. of</u> <u>Copies</u>	<u>Organization</u>	<u>No. of</u> <u>Copies</u>	<u>Organization</u>
2	Defense Research Establishment Suffield ATTN: Chris Weickert David MacKay Ralston, Alberta, TOJ 2NO Ralston CANADA	1	Centre d'Etudes de Gramat ATTN: SOLVE Gerald 46500 Gramat FRANCE
1	Defense Research Establishment Valcartier ATTN: Norbert Gass P.O. Box 8800 Courcellette, PQ, GOA 1RO CANADA	1	Centre d'Etudes de Vaujours ATTN: PLOTARD Jean-Paul Boite Postale No. 7 77181 Country FRANCE
1	Canadian Arsenals, LTD ATTN: Pierre Pelletier 5 Montee des Arsenaux Villie de Gardeur, PQ, J5Z2 CANADA	1	PRB S.A. ATTN: M. Vansnick Avenue de Tervueren 168, Bte. 7 Brussels, B-1150 BELGIUM
1	Ernst Mach Institute ATTN: A.J. Sulp Eckerstrasse 4 D-7800 Freiburg i. Br. WEST GERMANY	1	AB Bofors/Ammunition Division ATTN: Jan Hasslid BOX 900 S-691 80 Bofors SWEDEN
1	MBB ATTN: Manfred Held Postfach 1340 D-8898 Schrobenhausen WEST GERMANY		
3	IABG ATTN: HJ. Raatschen W. Schittke F. Scharppf Einsteinstrasse 20 D-8012 Otobrun b. Muenchen WEST GERMANY		
1	Royal Armament R&D Establishment ATTN: Ian Cullis Fort Halstead Sevenoaks, Kent TN14 7BP ENGLAND		
2	Royal Ordnance ATTN: Chris Constantinou R.C. Davies Euxton Lane, Euxton, Chorley Lancashire PR7 6AD ENGLAND		

## USER EVALUATION SHEET/CHANGE OF ADDRESS

This Laboratory undertakes a continuing effort to improve the quality of the reports it publishes. Your comments/answers to the items/questions below will aid us in our efforts.

1. BRL Report Number BRL TR-3090 Date of Report MAR 90

2. Date Report Received \_\_\_\_\_

3. Does this report satisfy a need? (Comment on purpose, related project, or other area of interest for which the report will be used.) \_\_\_\_\_  
\_\_\_\_\_  
\_\_\_\_\_

4. Specifically, how is the report being used? (Information source, design data, procedure, source of ideas, etc.) \_\_\_\_\_  
\_\_\_\_\_  
\_\_\_\_\_

5. Has the information in this report led to any quantitative savings as far as man-hours or dollars saved, operating costs avoided, or efficiencies achieved, etc? If so, please elaborate. \_\_\_\_\_  
\_\_\_\_\_  
\_\_\_\_\_

6. General Comments. What do you think should be changed to improve future reports? (Indicate changes to organization, technical content, format, etc.) \_\_\_\_\_  
\_\_\_\_\_  
\_\_\_\_\_  
\_\_\_\_\_

CURRENT  
ADDRESS

\_\_\_\_\_  
Name

\_\_\_\_\_  
Organization

\_\_\_\_\_  
Address

\_\_\_\_\_  
City, State, Zip Code

7. If indicating a Change of Address or Address Correction, please provide the New or Correct Address in Block 6 above and the Old or Incorrect address below.

OLD  
ADDRESS

\_\_\_\_\_  
Name

\_\_\_\_\_  
Organization

\_\_\_\_\_  
Address

\_\_\_\_\_  
City, State, Zip Code

(Remove this sheet, fold as indicated, staple or tape closed, and mail.)

-----FOLD HERE-----

**DEPARTMENT OF THE ARMY**

Director  
U.S. Army Ballistic Research Laboratory  
ATTN: SLCBR-DD-T  
Aberdeen Proving Ground, MD 21005-5066  
**OFFICIAL BUSINESS**



**NO POSTAGE  
NECESSARY  
IF MAILED  
IN THE  
UNITED STATES**

**BUSINESS REPLY MAIL**  
FIRST CLASS PERMIT No 0001, APG, MD

POSTAGE WILL BE PAID BY ADDRESSEE

Director  
U.S. Army Ballistic Research Laboratory  
ATTN: SLCBR-DD-T  
Aberdeen Proving Ground, MD 21005-9989

-----FOLD HERE-----

